UNIVERSITY OF CALIFORNIA SAN DIEGO

Tracking Past Changes in Ocean Heat Content with Atmospheric Noble Gases in Ice Cores

A dissertation submitted in partial satisfaction of the
requirements for the degree
Doctor of Philosophy

in

Earth Sciences

by

Sarah Ann Shackleton

Committee in charge:

Professor Jeffrey Severinghaus, Chair
Professor Helen Fricker
Professor Ralph Keeling
Professor Lynne Talley
Professor Mark Thiemens

2019

The dissertation of Sarah Ann Shackleton is approved, and it is acceptable in quality and form for publication on microfilm and electronically:

Chair

University of California San Diego

2019

EPIGRAPH

Do it for joy and you can do it forever

Stephen King

TABLE OF CONTENTS

LIST OF FIGURES

LIST OF TABLES

ACKNOWLEDGEMENTS

First, I would like to thank the individuals in the SIO administration who have consistently gone above and beyond in helping to navigate through the UC bureaucracy. We're extremely lucky to have you. Thanks to the members of my cohort and other SIO buddies for their comradery over these last six years. I'm especially grateful to my housemates Maddie, Dara, and Dox, who have been constant sources of support and joy throughout this whole experience. To my lab mates Daniel, Alan, Ross, Benni, Jessica, Jacob, and Berni – thank you so much for your guidance and advice; I've learned so much from you all. This work would not be possible without our collaborators at the University of Bern; I appreciate your trust and partnership in working through the challenges of the mean ocean temperature proxy. I could not have gotten through the last six years without my family. To my sisters, Emily and Leah, thank you for being my best friends and sometimes-benefactors; I look forward to the day when I can pick up the bill. To my parents, thank you for your unwavering encouragement and strength, and for your earnest interest in understanding what I'm doing and why it matters. I'm forever indebted to the members of the Taylor Glacier project. To Kathy and Jayred, my experience at Taylor Glacier wouldn't have been nearly as joyful without the two of you. To Andy and Michael, two thirds of the DyoMenkLeton field leadership, I'm so grateful for our field seasons together; you are excellent scientists and I look forward to seeing how our paths intertwine in the future. Thanks to my committee members, Helen, Ralph, Lynne, Mark, and Jeff for their advice when I've sought it; I wish I had done so more often. I'd especially like to thank my advisor, Jeff. Throughout my time at SIO, you've been incredibly supportive, and I truly appreciate your continual encouragement to trust myself as a scientist. Your excitement about science and discovery is contagious. Finally, I'd like to thank

Taylor Glacier. You've been a wonderful home and source of knowledge and growth; I hope to see you again someday.

Chapter 2, in full, is a reproduction of published materials in *Geophysical Research Letters*: Shackleton, S., Bereiter, B., Baggenstos, D., Bauska, T. K., Brook, E. J., Marcott, S. A., Severinghaus, J. P. Is the Noble Gas-Based Rate of Ocean Warming During the Younger Dryas Overestimated? *Geophysical Research Letters*, 2019. I was the primary investigator and author of this work.

Chapter 3 contains unpublished material with the following co-authors: Christo Buizert, Kenji Kawamura, Daniel Baggenstos, and Jeffrey Severinghaus. I was the primary investigator and author of this work.

Chapter 4, in full, is the reproduction of a manuscript that is currently in review at *Nature Geoscience*: Shackleton, S., Baggenstos, D., Menking, J. A., Dyonisius, M. N., Bereiter, B., Bauska, T. K., Rhodes, R. H., Brook, E. J., Petrenko, V. V., McConnell, J. R., Kellerhals, T., Häberli, M., Schmitt, J., Fischer, H., Severinghaus, J. P. Last Interglacial Peak Mean Ocean Temperature Due to Ocean Circulation Change. In Review at *Nature Geoscience*. I was the primary investigator and author of this work.

Chapter 5 contains unpublished material with the following co-authors: James Menking, Edward Brook, Vasilii Petrenko, Michael Dyonisius, Daniel Baggenstos, and Jeffrey Severinghaus. I was the primary investigator and author of this work.

VITA

2013	Bachelor of Arts in Chemistry, Wesleyan University
2016	Master of Science in Oceanography, UCSD
2019	Doctor of Philosophy in Earth Sciences, UCSD

PUBLICATIONS

Shackleton, S., et al., Last Interglacial Peak Mean Ocean Temperature Due to Ocean Circulation Change, in review at *Nature Geoscience.*

Dyonisius, M. N., et al., Old carbon reservoires were not important in the deglacial methane budget, in review at *Science.*

Menking, J. A., et al., Spatial pattern of accumulation at Taylor Dome during Marine Isotope Stage 4: stratigraphic constraints from Taylor Glacier. *Climate of the Past*, 15, 1537-1556, 2018.

Baggenstos, D., et al., The Earth's radiative imbalance from the Last Glacial Maximum to the present. *Proceedings of the National Academy of Sciences*, 116, 14881–14886, 2019.

Shackleton, S., et al., Is the noble gas-based rate of ocean warming during the Younger Dryas overestimated? *Geophysical Research Letters*, 46, 5928-5936, 2019.

Bauska, T. K., et al., Controls on Millennial-Scale Atmospheric CO_2 Variability During the Last Glacial Period. *Geophysical Research Letters*, 45, 7731-7740, 2018.

Bereiter, B., et al., Mean global ocean temperatures during the last glacial transition. *Nature*, 553, 39–44, 2018.

Baggenstos, D., et al., Atmospheric gas records from Taylor Glacier, Antarctica, reveal ancient ice with ages spanning the entire last glacial cycle. *Climate of the Past*, 13, 943–958, 2017.

ABSTRACT OF THE DISSERTATION

Tracking Past Changes in Ocean Heat Content with Atmospheric Noble Gases in Ice Cores

by

Sarah Ann Shackleton

Doctor of Philosophy in Earth Sciences

University of California, San Diego, 2019

Professor Jeffrey P. Severinghaus, Chair

As an emerging proxy for total ocean heat content, atmospheric noble gas ratios in ice cores have the promise to provide key insights into Earth's energy budget, and how it has responded to past climate perturbations. This method takes advantage of the mass-conservation of krypton, xenon, and dinitrogen in the combined ocean and atmosphere, and their unique temperature-dependent solubilities in seawater. By measuring changes in the noble gas ratios of the well-mixed atmosphere, we can deduce their change in the ocean due to warming or cooling, which allows us to track changes in total ocean heat content. As a new area of research, there is still much to learn about the proxy's potential, as well as its limitations. The motivation of this dissertation is twofold:

to identify the main sources of uncertainty in mean ocean temperature reconstructions and to apply the mean ocean temperature method to previously unstudied climate intervals.

To address our first goal, we focus on processes that decouple the noble gas ratios measured in ice cores from mean ocean temperature. While past studies have focused on this decoupling at the ocean-atmosphere interface (e.g. through dissolved gas disequilibrium), we primarily focus on the decoupling of gases at the atmosphere-ice sheet interface, and within the ice sheet itself. We identify previously unappreciated or underappreciated mechanisms of gas fractionation that, if not appropriately accounted for, introduce error into mean ocean temperature records. Based on our findings, we outline specific steps to identify and correct for these processes in order to minimize error in future mean ocean temperature studies.

To address our second goal, we reconstruct mean ocean temperature with ice cores from the Taylor Glacier blue ice area. Taylor Glacier has the advantage of being recently-drilled and clathrate-free, making it an ideal site for mean ocean temperature reconstruction. Using well-established methods of blue ice dating based on gas synchronization with well-dated ice cores, we identify and collect ice cores from the last interglacial period and last glacial inception for mean ocean temperature reconstruction. Considering the mean ocean temperature records presented here, along with previous reconstructions, a pattern emerges from the data; over a range of timescales and background climate states, we find a dominant role of the ocean's overturning circulation in controlling the timing and magnitude of mean ocean temperature change.

Chapter 1

Introduction

Today and in the past, the oceans have played a critical role in the evolution of global climate and represent the dominant energy reservoir in the climate system (Stocker et al., 2013). Understanding how the oceans have responded to external (e.g. greenhouse gas and insolation) and internal (e.g. circulation) perturbations in the past provides insight into their future response to climate change. However, even within the observational era, the ability to track changes in ocean heat content has been limited by the spatiotemporal resolution of available records (Abraham et al., 2013). This limitation is even more pronounced for reconstructions that extend beyond the observational era with marine-based proxies for ocean temperature.

The recently developed proxy for mean ocean temperature (MOT) from atmospheric noble gas ratios in ice cores (Headly & Severinghaus, 2007) has provided a method to circumvent the problem of limited spatial coverage of marine records. This method utilizes the temperature-dependent solubilities of krypton, xenon, and nitrogen in seawater to deduce total ocean heat content. With no major sources or sinks outside of the combined ocean and atmosphere, changes in the atmospheric content of these inert gases reflect a change in their oceanic reservoir, which is primarily governed by ocean temperature. Because ocean heat and gases are set and exchanged at the surface, any change in ocean heat content coincides with an exchange of inert gases between the atmosphere and the ocean with no lag in their respective response times. Because the atmosphere is well mixed, and krypton, xenon, and nitrogen have unique temperature-dependent solubilities, the atmospheric ratios of these gases provide a globally integrated signal of changes

in ocean heat content, and MOT (Ritz et al., 2011). Atmospheric noble gas ratios therefore provide a metric to track the evolving response of ocean temperature to a climate perturbation.

Atmospheric greenhouse and noble gases are trapped concurrently in ice as air bubbles, making it possible to produce simultaneous records of greenhouse forcing and MOT from a single ice core record. The ability to compare records of these two fundamental parameters in the climate system with no temporal uncertainty has crucial implications for understanding their interplay. Because CO_2 is highly soluble in seawater, ocean warming and cooling affect atmospheric CO_2. In turn, the radiative impact of CO_2 and other greenhouse gases on the Earth's energy budget influence total ocean heat content. Simultaneous records of MOT and CO_2 over a range of timescales and climate states may provide crucial insight into Earth system sensitivity.

Since the development of the MOT proxy, the analytical precision of noble gas measurements has markedly improved (Bereiter, Kawamura, et al., 2018). In addition, the drilling of the carefully-handled, high-resolution WAIS Divide ice core allowed for the recent reconstruction of MOT over the last deglaciation (Bereiter, Shackleton, et al., 2018). The glacial-interglacial MOT change found in this reconstruction of 2.6±0.2°C agrees well with the initial finding of 2.7±0.6°C (Headly & Severinghaus, 2007), but the improvement in analytical precision made it possible to detect subtle features in MOT change across the deglaciation that had been previously unidentified. The most striking aspect of this record was the close covariation of MOT and Antarctic temperature. Another surprising feature was a rapid warming that occurred in the first 700 years of the Younger Dryas and exceeded rates of modern warming.

This pioneering study highlighted the enormous potential of the MOT proxy. However, the dramatic improvement in analytical precision makes it necessary to carefully evaluate other potential sources of error in MOT reconstructions, which could greatly exceed the current

analytical uncertainty. As a new area of research, investigations into mechanisms that may decouple the noble gas ratios measured in ice cores from ocean heat content are limited and have primarily focused on the processes of gas and heat exchange at the ocean-atmosphere interface (Ritz et al., 2011).

The first of two main goals of this dissertation is to address processes that decouple the noble gas content of ice from the well-mixed atmosphere and assess associated uncertainties in the interpretation of MOT records. In Chapter 2, we explore a mechanism of gas fractionation during the transformation of air bubbles to clathrates in the ice that may introduce random error into MOT records. Comparing MOT reconstructions with ice cores from Taylor Glacier and WAIS Divide, we suggest that the recent result of rapid MOT warming in the first 700 years of the Younger Dryas may be an artifact of this fractionating process in the WAIS Divide ice core. In Chapter 3, we evaluate our understanding of the processes that fractionate noble gases in the consolidating snow (or firn) through measurements of modern air within the open pores of the firn, and in recently closed off air bubbles from sites across Greenland and Antarctica. Based on these results, we estimate the influence of systematic error in MOT reconstructions and suggest best practices to minimize their influence in future studies.

The second motivation of this dissertation is to extend the MOT record to unstudied climate intervals in order to gain greater insight into the controls on ocean heat content throughout a glacial cycle. In Chapter 4 we reconstruct MOT during the penultimate deglaciation and last interglacial period with ice cores from Taylor Glacier and EDC. Through comparison with other proxy records and modelling results, we suggest that the warmer-than-modern MOT that occurred at the onset of the last interglacial was a transient feature, due to the shut-down of the Atlantic Meridional Overturning Circulation, but one that had implications for the elevated sea level that is observed

during this interval. In Chapter 5 we reconstruct MOT during the last glacial inception (at around 70 ka) with ice cores from Taylor Glacier and WAIS Divide. With this record, we consider the role of ocean cooling in atmospheric CO_2 drawdown, the sequence of events that occur during glacial inceptions, and the response of MOT to AMOC perturbations on millennial timescales. Finally, we suggest target intervals for MOT reconstructions to further evaluate the role of internal and external perturbations in setting total ocean heat content.

References

Abraham, J. P., Baringer, M., Bindoff, N. L., Boyer, T., Cheng, L. J., Church, J. A., Conroy, J. L., Domingues, C. M., Fasullo, J. T., Gilson, J., Goni, G., Good, S. A., Gorman, J. M., Gouretski, V., Ishii, M., Johnson, G. C., Kizu, S., Lyman, J. M., Macdonald, A. M., et al. (2013). A review of global ocean temperature observations: Implications for ocean heat content estimates and climate change. *Reviews of Geophysics*, *51*(3), 450–483. https://doi.org/10.1002/rog.20022

Bereiter, B., Shackleton, S., Baggenstos, D., Kawamura, K., & Severinghaus, J. (2018). Mean global ocean temperatures during the last glacial transition. *Nature*, *553*(7686), 39–44. https://doi.org/10.1038/nature25152

Bereiter, B., Kawamura, K., & Severinghaus, J. P. (2018). New methods for measuring atmospheric heavy noble gas isotope and elemental ratios in ice core samples. *Rapid Communications in Mass Spectrometry*, *32*(10), 801–814. https://doi.org/10.1002/rcm.8099

Headly, M. A., & Severinghaus, J. P. (2007). A method to measure Kr/N2 ratios in air bubbles trapped in ice cores and its application in reconstructing past mean ocean temperature. *Journal of Geophysical Research*, *112*(19), 1–12. https://doi.org/10.1029/2006JD008317

Ritz, S. P., Stocker, T. F., & Severinghaus, J. P. (2011). Noble gases as proxies of mean ocean temperature : sensitivity studies using a climate model of reduced complexity. *Quaternary Science Reviews*, *30*(25–26), 3728–3741. https://doi.org/10.1016/j.quascirev.2011.09.021

Stocker, T. F., Qin, D., Plattner, G.-K., Tignor, M., Allen, S. K., Boschung, J., Nauels, A., Xia, Y., Bex, V., & Midgley, P. M. (2013). Climate change 2013: The physical science basis. Cambridge University Press Cambridge.

Chapter 2

Is the Noble Gas-Based Rate of Ocean Warming During the Younger Dryas Overestimated?

Abstract

Noble gases in ice cores enable reconstructions of past mean ocean temperature. A recent result from the clathrate-containing WAIS Divide Ice Core showed tight covariation between ocean and Antarctic temperatures throughout the last deglaciation, except for the Younger Dryas interval. In the beginning of this interval, oceans warmed at 2.5 °C/kyr—three times greater than estimates of modern warming. If valid, this challenges our understanding of the mechanisms controlling ocean heat uptake. Here we reconstruct mean ocean temperature with clathrate-free ice samples from Taylor Glacier to test these findings. The two records agree in net temperature change over the Younger Dryas, but the Taylor Glacier record suggests sustained warming at the more modest rate of 1.1 ± 0.2°C/kyr. We explore mechanisms to explain differences between records and suggest that the noble gas content for the Younger Dryas interval of WAIS Divide may have been altered by a decimeter-scale fractionation during bubble-clathrate transformation.

2.1. Introduction

Ocean heat uptake plays a crucial role in regulating the rate of planetary warming. To understand mechanisms controlling ocean warming on centennial-millennial timescales, it is necessary to consult paleoclimate archives. Reconstructions of atmospheric noble gas ratios (Kr/N_2, Xe/N_2, and Xe/Kr) from trapped air in ice cores reflect past mean ocean temperature (MOT) due to the temperature-dependent changes of gas solubilities in seawater and thus the relative partitioning of noble gases between the ocean and atmosphere (Headly & Severinghaus, 2007; Ritz et al., 2011). The MOT proxies reflect volume-averaged ocean temperature change; the rate of MOT change (or ocean heat uptake) depends on both the magnitude of the surface forcing and on ocean mixing/circulation. A recent MOT study covering the last deglaciation from the Antarctic WAIS Divide (WD) ice core showed features in MOT change that were not apparent in traditional ocean temperature reconstructions from marine sediment cores, including covariation between MOT and Antarctic temperature (Bereiter, Shackleton, et al., 2018). The exceptional resolution and age control of this record enabled strong constraints on rates of ocean temperature change. The most surprising feature of this record was a 1.6 °C MOT warming in the first 700 years of the Younger Dryas (referred to as YD1), which is roughly triple the rate of modern ocean warming. This interval represents the only significant deviation of the MOT trend from that of Antarctic temperature during the last deglaciation (Figure 1).

The Younger Dryas (12.75–11.55 ka BP) was marked by abrupt cooling of Greenland and the North Atlantic (Broecker et al., 1988) and gradual warming in Antarctica (Blunier et al., 1997), as a result of reduction in Atlantic Meridional Overturning Circulation (AMOC; Broecker et al., 1989). The Younger Dryas ended with abrupt recovery of the AMOC (McManus et al., 2004). Modeling studies suggest that MOT and ocean heat content should increase through the duration

of AMOC reduction at a rate roughly one quarter of that found at WD for YD1 (Galbraith et al., 2016; Pedro et al., 2018). As of yet, no evidence for major changes in climate or ocean circulation have been found that shed light on the YD1 warming.

Because of the important implications of the rapid YD1 MOT warming, we sought to replicate this MOT change with another ice core record. We analyzed samples from Taylor Glacier, Antarctica, a blue ice area where ice from the last glacial cycle can be found in abundance (Baggenstos et al., 2017). Importantly, the air in Taylor Glacier ice is enclosed entirely in the form of bubbles and lacks clathrates due to the relatively shallow depth of the glacier, while WD is a deep ice core in which the Younger Dryas is within fully clathrated ice, approximately 400 to 500 m below the bubble-clathrate transition zone (BCTZ; Fitzpatrick et al., 2014).

2.2. Methods and Site Description

Sixteen ice core samples from Taylor Glacier covering 13.4–11.0 ka BP were collected along a previously established sampling line, which contains a well-dated, high-resolution record of the last deglaciation (Baggenstos et al., 2017). Samples were analyzed for isotopes of nitrogen, argon, and krypton and Kr/N_2, Xe/N_2, and Xe/Kr following Bereiter, Kawamura, et al. (2018). Results are reported in delta notation, relative to the modern atmosphere.

Ice core Kr/N_2, Xe/N_2, and Xe/Kr are influenced by gravitational (Schwander, 1989; Craig et al., 1988) and thermal (Severinghaus et al., 1998) fractionation. Because the effects of gravitational and thermal fractionation are well understood for the measured gases, the isotope ratios can be used to correct Kr/N_2, Xe/N_2, and Xe/Kr to derive their original atmospheric

compositions. We solve for fractionations using all measured isotope ratios in a linear least squares system of equations (Baggenstos, 2015; and supporting information).

To derive MOT, Kr/N_2, Xe/N_2, and Xe/Kr were input into the four-box ocean-atmosphere model of Bereiter, Shackleton, et al. (2018). To estimate uncertainty in the rate and magnitude of MOT change in the Taylor Glacier record, we run 10,000 Monte Carlo simulations of the data, propagating analytical uncertainties, sample age uncertainties, and uncertainties in the sea level record used in the box model (Lambeck et al., 2014) through the full evaluation routine.

2.3 Results/Discussion

2.3.1. Taylor Glacier and WD MOT records

Figure 1 shows the MOT results for Taylor Glacier compared to WD. The Taylor Glacier record shows sustained warming over the whole Younger Dryas interval at 1.1 ± 0.2 °C/kyr (1σ) for a total warming of 1.3 °C over 1,200 years. Overall, trends for Taylor Glacier are consistent with those of Antarctic temperature. While the WD record suggests similar net warming of 1.4 °C during the Younger Dryas, MOT change occurs in two phases. There is a rapid (2.5 ± 0.5 °C/kyr) warming in the first 700 years (YD1), followed by ~0.8 °C/kyr cooling in the final 500 years of the Younger Dryas. The Taylor Glacier and WD MOT records agree (within uncertainty) for much of the Younger Dryas, but they differ significantly in the warming rate during YD1 (supporting information). These rates are tightly constrained for each record, due to the high sampling resolution within this interval. Potential explanations for the differences between the records are explored below.

2.3.2. Lab artifacts and data processing

Because the WD and Taylor Glacier records were measured using the same analytical method, we can rule out laboratory artifacts as the source of disagreement between the two records. However, for Taylor Glacier we applied a different method to correct for firn fractionations and slightly different parameterizations to the box model compared to the WD study. If we apply the same firn corrections and box model parameters to WD as we used for Taylor Glacier (open circles, Figure 1), we find that the whole record shifts to warmer MOT by ~0.4 °C, but the record structure remains essentially unchanged, and there is no significant change to the rate of warming during YD1. This suggests that the differences between records are likely a result of some unaccounted-for physical process within the firn or ice.

2.3.3. Smoothing of the Taylor Glacier MOT Record

An important consideration when comparing the WD and Taylor Glacier records is the effect of signal smoothing in the firn column (Spahni et al., 2003). Compared to the atmosphere, fast variations in gas records in ice cores are low-pass filtered because (1) gases within firn mix slowly with the atmosphere through molecular diffusive transport and (2) bubble enclosure occurs gradually over a depth range of ~15 m (Schwander et al., 1988). In effect, gases within an ice layer do not have a single age, but a distribution of ages. This smoothing process has greatest impact on gases that undergo fast atmospheric changes (e.g., CH_4), but if bubble close-off occurs gradually enough, it may also affect slower atmospheric changes such as the noble gas trends observed during YD1.

The degree of smoothing depends on site conditions; cold, low accumulation sites tend to have the widest gas age distributions and thus experience the most smoothing (Spahni et al., 2003). Because of its high accumulation and relatively moderate temperature, WD has an exceptionally narrow gas age distribution width (20 to 60 years; Rhodes et al., 2017); the noble gas MOT record should be virtually unaltered by smoothing at this site. In contrast, the Taylor Glacier deposition site has lower accumulation and colder temperatures, so a wider gas age distribution is expected. The YD1 MOT warming suggested by WD is quite rapid; one possible explanation for the differences between the two records is that the noble gas record is smoothed at Taylor Glacier.

In order to quantify the differences between the two MOT records due to smoothing, we compare abrupt CH_4 transitions at the onset and termination of the Younger Dryas between Taylor Glacier (Bauska et al., 2016) and WD (Rhodes et al., 2015). Because these atmospheric CH_4 changes are rapid (several hundred ppb over a few hundred years), they should be more affected by smoothing than the MOT record. From the degree of smoothing of the Taylor Glacier CH_4 record compared to WD, it is possible to predict the degree of smoothing of the Taylor Glacier MOT record. The Taylor Glacier age scale was developed through gas synchronization between Taylor Glacier and WD from measurements of CH_4, CO_2, and $\delta^{18}O_{atm}$ (Baggenstos et al., 2017). A dynamic programming algorithm (Lisiecki & Lisiecki, 2002) was employed to optimize the fit of the Taylor Glacier gas records to those of WD on the WD2014 chronology (Buizert et al., 2015; Sigl et al., 2016), while maintaining a physically realistic (i.e., smooth) distance-age relationship. Because CH_4 data are used to constrain the age model, it is somewhat circular to compare rates of CH_4 transitions between WD and Taylor Glacier on the published Taylor Glacier age scale. To circumvent this issue, we reran the dynamic algorithm with $\delta^{18}O_{atm}$ alone. While the age model is

still tied to WD2014, $\delta^{18}O_{atm}$ variations are several orders of magnitude slower than those of CH4, so the effect of smoothing on $\delta^{18}O_{atm}$ is negligible.

On the new Taylor Glacier timescale, rates of CH_4 change ($d[CH_4]/dt$) at the transitions are comparable to those of WD, suggesting no substantial smoothing of the Taylor Glacier record relative to WD (Figure 2). In fact, the Younger Dryas termination $d[CH_4]/dt$ is actually greater at Taylor Glacier than at WD. This is the more abrupt of the CH_4 transitions, so we would expect it to be more sensitive to smoothing. Comparing CH_4 transitions between Taylor Glacier and WD, it is important to note that the Taylor Glacier CH_4 data are in much lower resolution than for WD, so there is greater uncertainty in Taylor Glacier $d[CH_4]/dt$. However, high-resolution field measurements of CH4 at Taylor Glacier confirm the $d[CH_4]/dt$ of the lower resolution lab-based measurements (supporting information), and uncertainties in $d[CH_4]/dt$ have little impact on smoothing estimates.

We convolved the WD CH4 and MOT records with a log-logistic function to predict the degree of smoothing of the MOT record at Taylor Glacier from the observed CH4 smoothing at Taylor Glacier relative to WD. A log-logistic function was chosen to approximate the gas age distribution at Taylor Glacier and realistically simulate smoothing (supporting information). However, results are insensitive to the shape of the smoothing function; a simple boxcar function yields a similar relationship between the degree of smoothing of the CH4 record and the MOT record.

As expected, the CH_4 record is significantly more sensitive to smoothing than the MOT record. The observed 18% reduction of $d[CH_4]/dt$ at Taylor Glacier (compared to WD) at the Younger Dryas onset gives an expected reduction in the YD1 MOT rate of 0.5% at Taylor Glacier

relative to WD. Accounting for uncertainties in Taylor Glacier d[CH_4]/dt, an upper bound on smoothing of the CH_4 record (59%) predicts an upper estimate on MOT smoothing of 6% in the Taylor Glacier record. However, the observed rate of MOT warming at Taylor Glacier is 64% reduced compared to WD during YD1. From these results, we can confidently reject the hypothesis that the difference between the Taylor Glacier and WD MOT records is the result of smoothing.

2.3.4. Outliers in the WD Record Due to Clathrate Layering

In addition to higher rates of MOT warming during YD1, the WD record also has more high frequency variability than Taylor Glacier during and just after the Younger Dryas (Figure 3). Here we consider the possibility that high frequency variations in the WD noble gas record during the Younger Dryas and Early Holocene are not atmospheric and are instead related to fractionation of noble gases due to layering during bubble-clathrate transformation. Taylor Glacier samples are entirely in bubbly ice and therefore free of any such effect.

The proposed mechanism was originally invoked to explain centimeter-scale variations in CO_2 and O_2/N_2 measurements within and just below the BCTZ (Lüthi et al., 2010). The effect is summarized as follows: the fractionation of gases in the BCTZ is due to the differential permeation of gases from bubbles to growing clathrates. Clathrate formation does not occur gradually with increasing depth but in layers. Layers in which clathrates first form are more enriched in gases with higher bubble-to-clathrate permeation rates, even after all surrounding bubbles have transformed to clathrates. Below the BCTZ, gas content slowly rehomogenizes via molecular diffusion through the ice lattice, which can take tens of thousands of years (Bereiter et al., 2009). The proposed mechanism would introduce systematic error within the BCTZ and random error to

samples below the BCTZ that decreases with depth, as gases have more time to rehomogenize and thinning of layers enhances diffusion.

In the BCTZ (where bubbles and clathrates coexist), we observe systematic error in gases influenced by clathrate layering. For CO_2, this is due to the preferential sampling of bubbles over clathrates during gas extraction (Stauffer & Tschumi, 2000). For O_2/N_2 and Ar/N_2 (and likely Kr/N_2, Xe/N_2, and Xe/Kr), there is preferential sampling of clathrates, because of gas loss from bubbles from core cracking during drilling due to the brittle nature of ice in the BCTZ (Bender & Sowers, 1995; Kobashi et al., 2008). In contrast, for samples just below the BCTZ (in fully clathrated ice), we expect random error associated with this clathrate layering process, depending on whether the depth interval preferentially contains earlier or later-formed clathrates. Bereiter, Kawamura, et al. (2018) showed that Kr/N_2, Xe/N_2, and Xe/Kr are systematically fractionated in the BCTZ at WD, and noble gas samples in this region were rejected from the MOT record. However, spatial fractionation of Kr/N_2, Xe/N_2, and Xe/Kr beyond the BCTZ (and the associated random error) was not considered, because samples were averaged over a length (~30 cm) that earlier studies suggest should have homogenized the spatial variability caused by clathrate layering.

Lüthi et al. (2010) suggested that samples averaged over more than 10 cm provide reliable gas measurements. However, the estimate of averaging length of Lüthi et al. (2010) came from a single ice core (EDML) from high-resolution CO_2 measurements. Unfortunately, we do not have high resolution gas data to estimate the required averaging length at WD, but it is possible that the length scale of clathrate layering varies between sites. It is important to note that the processes driving clathrate layering are not fully understood but that the limiting step in bubble-clathrate transformation is clathrate nucleation. Factors including grain size (Faria et al., 2010), bubble size

(Lipenkov, 2000), and ice chemistry (Ohno et al., 2010; Shimada & Hondoh, 2004) may influence clathrate nucleation. While a consensus has yet to be reached on the relative importance of these factors, they are all either directly or indirectly related to ice impurity content. Ice chemistry data from the Younger Dryas depth interval at WD suggest layering of impurities on the order of tens of centimeters (Sigl et al., 2016, and supporting information), so we find it plausible that the 30-cm MOT samples may still be affected by this process.

Because little is known about the permeation rates of gases from bubbles to clathrates, we look to empirical evidence to estimate the range of gas rehomogenization below the BCTZ. One indication that clathrates at a given depth below the BCTZ have not fully rehomogenized is the elevation of CO_2 pair differences with respect to deeper/older samples for which rehomogenization has already occurred (Lüthi et al., 2010). In addition to CO_2, we consider pair differences in O_2/N_2 and Ar/N_2 to identify the depth range of clathrate rehomogenization. In order to identify the influenced depth range, we bin data of standard deviations for replicate samples of WD CO_2 (Marcott et al., 2014), O_2/N_2, and Ar/N_2 (Seltzer et al., 2017) into 100-m depth intervals and use a Student t test to determine if the standard deviations within a given depth interval are greater (at the 95% confidence level) than the deepest (2,500–2,600 m) bin. The standard deviations for all three gases are clearly elevated within and just below the BCTZ (Figure 3). O_2/N_2 and Ar/N_2 standard deviations show statistically significant elevated values down to 2,000 m, while CO_2 standard deviations are significantly higher down to 2,100 m. The WD Early Holocene data are within the depth range identified from all three gas measurements, and the YD1 interval (2,034–2,094 m) is within the range identified by CO_2. If a larger bin size is used to identify the range of affected data (e.g., 200 m) so that there are more data per bin, the range extends even deeper (2,200 m for O_2/N_2 and Ar/N_2 and 2,400 m for CO_2). From these observations, we find it plausible that

the noble gas ratios have still not fully homogenized at WD for the YD1 interval, and the spatial fractionation may still be in effect for deeper MOT samples. This spatial fractionation may have randomly altered a few WD data points within the Younger Dryas to create the observed two-phase pattern of MOT.

If we compare the standard deviation of the CO_2, O_2/N_2, and Ar/N_2 replicate data within the YD1 depth interval to that of the deepest bin (2,500–2,600 meters), we find that the standard deviations are on average 37%, 49%, and 53% elevated for CO_2, O_2/N_2, and Ar/N_2, respectively, within YD1, compared to the deepest samples. To estimate the magnitude of the error in MOT associated with clathrate layering, we artificially increase the reported WD MOT error within YD1 and run Monte Carlo simulations of the data to determine the increase in WD MOT error required so that the difference between the Taylor Glacier and WD YD1 warming rates is no longer statistically significant at the 95% confidence level (supporting information). We estimate a 35% increase in error due to clathrate layering within YD1. Note that we expect the error associated with clathrate layering to increase closer to the BCTZ, where clathrates have had less time to rehomogenize, so uncertainties in the early Holocene MOT data may be even larger than those estimated for the YD1 interval.

2.3.5. Reliability of WD versus Taylor Glacier MOT records

While we posit that clathrate layering in the WD record is the most likely cause for the disagreement between the WD and Taylor Glacier records, there is not enough evidence to conclusively reject the Younger Dryas in WD. However, there are several reasons that suggest the Taylor Glacier record is more plausible than that of WD. The first is the agreement between MOT

proxies. MOT records derived from Kr/N_2, Xe/N_2, and Xe/Kr at Taylor Glacier show excellent agreement in overall trends and absolute MOT. While WD Kr/N_2, Xe/N_2, and Xe/Kr MOT records are in general agreement, they show more spread in absolute MOT, and the duration and magnitude of the YD1 MOT change differ slightly between the three proxies (Figure 1).

In addition, the Taylor Glacier record is more physically consistent with the expected response of MOT to ocean circulation changes during the Younger Dryas inferred from models. Proxy evidence for ocean circulation (McManus et al., 2004; Stieglitz et al., 2011) suggests that AMOC strength within the Younger Dryas was weakened, but relatively stable. Model simulations under weakened (and stable) AMOC conditions show sustained MOT warming (Galbraith et al., 2016; Pedro et al., 2018), which is consistent with the Taylor Glacier record. The modeled rates of MOT warming are about 40% lower than the Taylor Glacier record; however, these simulations were run under conditions that are more consistent with Heinrich Stadial 1 and are consistent with MOT warming rates found for Heinrich Stadial 1 (Bereiter, Shackleton, et al., 2018).

Interestingly, proxy evidence would suggest that the rate of MOT warming during Heinrich Stadial 1 may exceed that of the Younger Dryas, because the relative magnitude of AMOC reduction is greater during the former (McManus et al., 2004). However, the scaling between the AMOC reduction and rate of ocean warming has not (to our knowledge) been rigorously explored. In addition, the higher obliquity during the Younger Dryas (relative to Heinrich Stadial 1) results in higher annually averaged insolation at high latitudes, where deep-water formation occurs (Bereiter, Shackleton, et al., 2018). The increased insolation at these sites during the Younger Dryas may help to explain the higher rate of MOT warming found compared to Heinrich Stadial 1.

2.4. Conclusions

We suggest that a previously identified form of fractionation of CO_2 in ice cores may also affect Kr/N_2, Xe/N_2, and Xe/Kr measurements in ice samples below the BCTZ, adding random noise to the derived atmospheric noble gas ratios. While sample rejection within the BCTZ has been previously recommended for MOT records, we caution in interpreting high-frequency variations in samples several hundred meters below the BCTZ and suggest that the uncertainty in MOT within this depth region may be significantly larger than the analytical uncertainty of the method. Future work must be done to find more direct evidence of this mechanism and to better understand its effect on Kr/N_2, Xe/N_2, and Xe/Kr.

Considering these findings, we posit that the Taylor Glacier record shows a more plausible scenario of MOT warming over the Younger Dryas than that of WD and that MOT and Antarctic temperature covaried through the entirety of the last deglaciation. The rate of MOT warming (1.1 ± 0.2 °C/kyr) from the Taylor Glacier record is significantly smaller than that from WD, but the Younger Dryas MOT warming rate found for this study is still about 70% greater than that of Heinrich Stadial 1 and 40% greater than estimates of ocean heat uptake from 1955 to 2010 (Levitus et al., 2012). The differing rates of ocean heat uptake between the Younger Dryas and Heinrich Stadial 1 are not fully understood, though models have successfully captured the rate of ocean warming during Heinrich Stadial 1. Future simulations of the Younger Dryas may serve as a valuable opportunity to distinguish between internal (ocean circulation) and external (greenhouse gas and insolation) controls on ocean heat uptake.

2.S1: Fractionation corrections for $\delta Kr/N_2$, $\delta Xe/N_2$ and $\delta Xe/Kr$

To derive atmospheric $\delta Kr/N_2$, $\delta Xe/N_2$ and $\delta Xe/Kr$ for mean ocean temperature (MOT) reconstruction, we assume that these noble gas ratios measured in ice cores reflect their atmospheric composition, modified by gravitational and thermal fractionation that occurs within the firn:

$$\delta'_{meas} = \delta'_{atm} + \delta'_{grav} + \delta'_{therm}$$

Where $\delta' = \ln(q)$ and $q = R_{sample}/R_{standard}$ (Markle, 2017). We use δ' here, which is approximately equal to the standard delta, because gravitational and thermal fractionation can be expressed linearly in terms of δ'. Atmospheric isotope ratios of krypton, argon and nitrogen are not affected by ocean solubility changes, so these ratios measured in ice cores only reflect firn fractionations. In order to correct $\delta Kr/N_2$, $\delta Xe/N_2$ and $\delta Xe/Kr$, we set up a linear system of equations of measured $\delta^{15/14}N$, $\delta^{40/38}Ar$, $\delta^{40/36}Ar$, $\delta^{86/84}Kr$, $\delta^{86/83}Kr$, and $\delta^{86/82}Kr$ to solve for the thermal gradient and gravitational settling (or diffusive column height) within the firn. The scaling of gravitational settling for the isotopes and elemental ratios is mass dependent:

$$\delta'_{grav} = \frac{\Delta m_{x-y} g z}{RT}$$

Where Δm is the mass difference of the gas pair (x-y), g is the gravitational constant, z is depth in the diffusive column, R is the gas constant, and T is average firn temperature. The relative influence of thermal fractionation on the isotope and elemental ratios is proportional to their laboratory-determined thermal diffusion sensitivities:

$$\delta'_{therm} = \Omega \Delta T$$

Ω is the thermal diffusion sensitivity of the gas pair and ΔT is the firn thermal gradient. In the linear least squares system, all isotopes are included, and isotope ratios are weighted by their analytical precision. Once diffusive column height and thermal gradient are determined, ice core $\delta Kr/N_2$, $\delta Xe/N_2$ and $\delta Xe/Kr$ are corrected for gravitational settling and thermal fractionation to derive their atmospheric content (see Figure S1). These corrected noble gas ratios are then input into an ocean-atmosphere box model to determine MOT.

2.S2: Assessment of Taylor Glacier and WD MOT disagreement over YD1

Because of the relatively large analytical uncertainties in MOT reconstructions, some differences are to be expected between the Taylor Glacier and WAIS Divide (WD) records. As such, it is important to test if differences in the Taylor Glacier and WD rates of MOT warming during the Younger Dryas 1 interval (YD1, 12.8-12 ka) are due to analytical noise, or if additional unknown processes are affecting one or both of the MOT records. For this test, we estimate uncertainty in the YD1 warming rates from 10,000 Monte Carlo simulations of the MOT data points within the YD1 interval for the respective Taylor Glacier and WAIS Divide records.

In a first evaluation, we vary the data in each record according to the reported error for each data point (Bereiter et al., 2018, Figure 1 of the main text) and measure the YD1 warming rate (d[MOT]/dt) for each simulation. We then estimate the error of the YD1 warming rate for Taylor Glacier and WD from the distributions of the respective Monte Carlo simulations (Figure S2) and apply a two-tailed z-test to determine the statistical significance of the difference between the two records (p=.016). However, reported error bars for the WD MOT data include systematic

uncertainties (e.g. ocean saturation state) and do not include analytical uncertainties in the isotope ratios used to correct the noble gas ratios. Consequently, it may be inappropriate to use the published WD error to test the hypothesis that the WD and Taylor Glacier record differences are attributed to analytical noise. As such (and for consistency in record comparison), we also run the raw WD isotope and noble gas data through the same Monte Carlo evaluation routine as applied for Taylor Glacier, with WD reported analytical error for isotope and noble gas measurements (Bereiter et al., 2018). From these simulations, the WD YD1 distribution narrows slightly (Figure S2), resulting in a more statistically significant difference between the Taylor Glacier and WD YD1 warming rates ($p=.002$). From these analyses, we can reject the null hypothesis at the >95% confidence level that YD1 warming rates found for Taylor Glacier and WD are the same within analytical uncertainty. This suggests that other processes and/or sources of uncertainty are required to explain the difference between the two records.

Assuming that the disagreement between the Taylor Glacier and WD MOT records during YD1 is due to clathrate layering in WD, we can estimate the magnitude of its associated error. By artificially increasing the MOT error bars in the WD YD1, running Monte Carlo simulations of the data, and comparing the results to the Taylor Glacier simulations using a z-test, we can determine what size MOT error bars are necessary for the WD YD1 record to agree with Taylor Glacier within error. We iteratively increase the WD MOT error bars until we find values at which we can no longer reject the null hypothesis that the WD and Taylor Glacier warming rates are the same ($p > .05$). For YD1, we find that the WD MOT error bars need to be 35% larger than the published values, or about 0.35°C (1σ), to agree with the Taylor Glacier record.

2.S3: Taylor Glacier gas age distribution function and smoothing estimates

In order to quantify the reduction in Taylor Glacier YD1 MOT warming that may be attributed to signal smoothing in the firn, we convolve the WD MOT record with an approximation of the gas age distribution at Taylor Glacier to simulate record smoothing. A log-logistic function is used to represent the gas age distribution (Figure S2):

$$y = \frac{(\beta/\alpha)(x/\alpha)^{\beta-1}}{(1+(x/\alpha)^{\beta})^2}$$

Where x is gas age, or time since last exchange with the atmosphere (in years), and α and β are the free parameters of the distribution function. The α parameter determines the width of the distribution and is equal to the median age of the distribution. β is the shape parameter of the distribution, and determines the skewness, and kurtosis of the distribution. The gas age distribution was truncated at three times the median age (α) to prevent unrealistically long tails, as bubble close-off only occurs in the bottom ~15 meters of the firn (Spahni et al., 2003).

Several other probability distributions (e.g. log-normal) were considered for modeling the gas age distribution and yielded virtually identical results for a given gas age distribution width. The log-logistic distribution was chosen because of its mathematical tractability and limited number of free parameters. To physically represent the Taylor Glacier gas age distribution, a range of β values was tested, but the degree of signal smoothing (which is the primary interest of this analysis) is quite insensitive to this parameter. A β value of 1.5 was chosen because it yields a

similar degree of skewness to the gas age distribution for EDC determined from a firn densification model (Spahni et al., 2003).

The degree of signal smoothing is almost entirely dependent on the α parameter, which is directly proportional to the width of the gas age distribution. In order to determine a realistic value for α for Taylor Glacier, we compare the CH_4 record Taylor Glacier to that of WD. By comparing the relative rates of CH_4 change ($d[CH_4]/dt$) between the two records, we can quantify how smoothed the CH_4 Taylor Glacier record is, relative to WD (Table S1). We then convolve the WD CH_4 record with gas age distributions with a range of α values. The gas age distribution (and α value) that best replicates the observed Taylor Glacier $d[CH_4]/dt$ is then used to convolve the WD MOT record to predict the degree of smoothing of the Taylor Glacier MOT record. The relationship between the smoothing of the $d[CH_4]/dt$ and d[MOT]/dt signals is shown in Figure 2 of the main text.

Error in Taylor Glacier $d[CH_4]/dt$ results in error in the assigned α value for the gas age distribution function, and ultimately in the estimation of MOT smoothing for Taylor Glacier. In order to estimate the uncertainty in Taylor Glacier $d[CH_4]/dt$, we run 50,000 Monte Carlo simulations of the Taylor Glacier CH_4 data including age uncertainty and analytical uncertainty in CH_4. Only simulations that fulfilled the expected age/distance monotonic change were considered in our analysis (~30% of simulations rejected). Because we are interested in an upper bound estimate for smoothing of the MOT record at Taylor Glacier, we consider the 95^{th} percentile of the Monte Carlo distribution of $d[CH_4]/dt$ for the Younger Dryas onset as an upper bound of the observed smoothing of the Taylor Glacier CH_4 record (Table S1). The Younger Dryas onset (rather than termination) was selected to estimate smoothing of the Taylor Glacier record, because CH_4 data at the termination showed minimal evidence of smoothing (Figure S4). This upper bound

d[CH_4]/dt value is then used (as above) to estimate an α value, and finally an upper bound estimate of smoothing of the Taylor Glacier MOT record.

To investigate the influence of sampling resolution on estimates of d[CH_4]/dt at the Younger Dryas onset at Taylor Glacier, samples were taken at higher resolution slightly up and down-glacier of the established sampling line and measured for CH_4 in the field during the 2012-2013 field season (Figure S5). To compare to laboratory measurements, field measurements are offset by -17.2 ppb based on the overall field-lab offset for this season. Transect distances were adjusted by -3.5m so that the CH_4 transition aligned with the original transect. Slopes of the transition (d[CH_4]/dt) at the Younger Dryas onset are comparable for the up and down-glacier sampling lines and the original lab data but include features of the CH_4 transition (compared to WD) that were missing in the lower resolution lab measurements. There are some slight differences in the features of the sampling lines, which may be related to artifacts due to layered bubble trapping (Rhodes et al., 2016)

Acknowledgements

This work was supported by NSF grants 1246148 (SIO), 1245821 (OSU) and 0739766 (OSU). Presented data are available online at http://www.usap-dc.org/view/dataset/601176. We thank Kathy Schroeder, Michael Dyonisius, and Vasilii Petrenko for making this fieldwork possible through exceptional organization and leadership and Mike Jayred, Andy Menking, and Peter Neff for their help with sampling and camaraderie in the field. Thanks especially to Heidi Roop for being an upbeat and hardworking field partner for this project. The US Antarctic Program and IDDO (Ice Drilling Design and Operations) provided logistical support for this project. Thanks

to Ross Beaudette for labwork assistance, Christo Buizert for helpful discussions on gas smoothing, and Alan Seltzer for providing helpful feedback on figures and content.

Chapter 2, in full, is a reproduction of published materials in *Geophysical Research Letters*: Shackleton, S., Bereiter, B., Baggenstos, D., Bauska, T. K., Brook, E. J., Marcott, S. A., Severinghaus, J. P. Is the Noble Gas-Based Rate of Ocean Warming During the Younger Dryas Overestimated? *Geophysical Research Letters*, 2019. I was the primary investigator and author of this work.

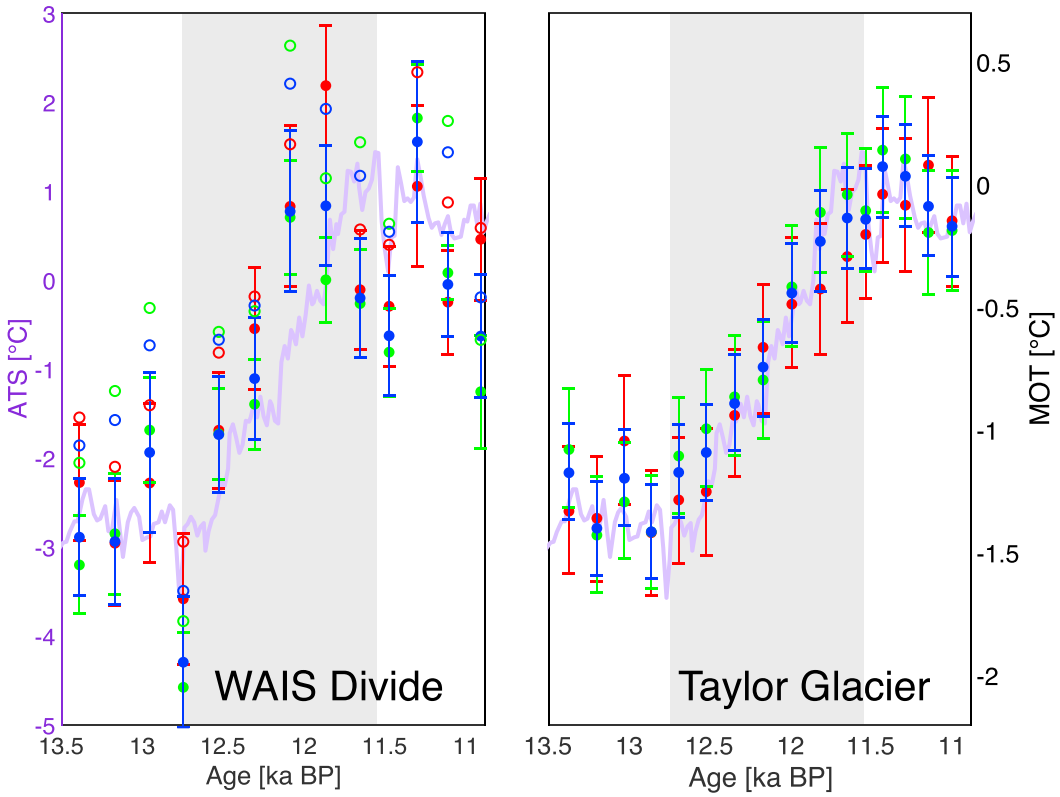

Figure 2.1. Mean ocean temperature (MOT) records for published WAIS Divide (WD; left; Bereiter, Shackleton, et al., 2018) and Taylor Glacier (right) derived from Kr/N_2 (red), Xe/N_2 (blue), and Xe/Kr (green) with 1σ uncertainties (scale on right). Open circles in left panel show WD data corrected with the least squares method applied in this study. Antarctic temperature stack (ATS; Parrenin et al., 2013) is shown in purple (scale on left). MOT and ATS data are displayed as anomalies relative to modern. Gray bars highlight the Younger Dryas.

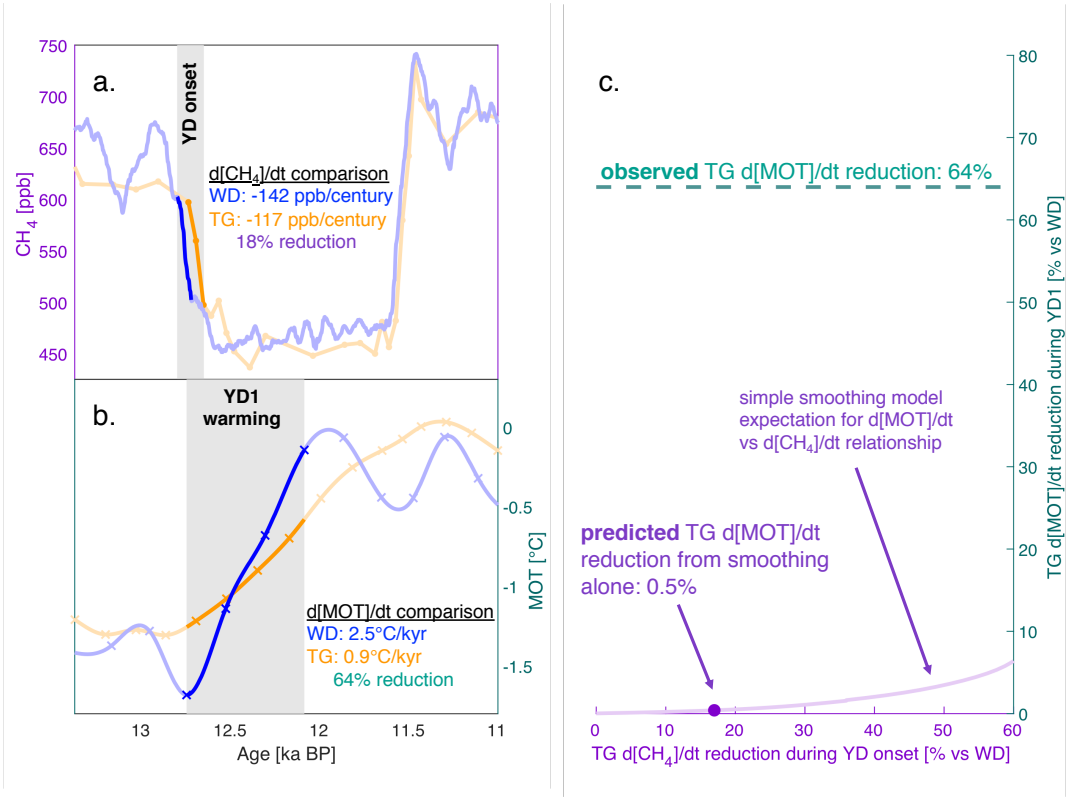

Figure 2.2. Comparison in rates of CH4 and mean ocean temperature (MOT) change at Taylor Glacier (TG) compared to WAIS Divide (WD). (a) CH4 records from TG (discrete, orange; Bauska et al., 2016) and WD (continuous, blue; Rhodes et al., 2015). Gray bar highlights CH4 data used to estimate smoothing at TG. (b) Splined MOT records for TG (orange) and WD (blue; Bereiter, Shackleton, et al., 2018). Crosses indicate location of MOT data used to produce spline. Reported TG d[MOT]/dt is for the YD1 interval, which differs slightly (but agrees within uncertainty) with the d[MOT]/dt reported for the full Younger Dryas interval. Gray bar highlights YD1. (c) Modeled reduction of d[MOT]/dt versus d[CH4]/dt at TG (relative to WD) due to smoothing. Purple dot shows observed reduction of TG d[CH4]/dt and the expected reduction of d[MOT]/dt. Dashed teal line indicates the observed reduction of d[MOT]/dt for TG compared to WD.

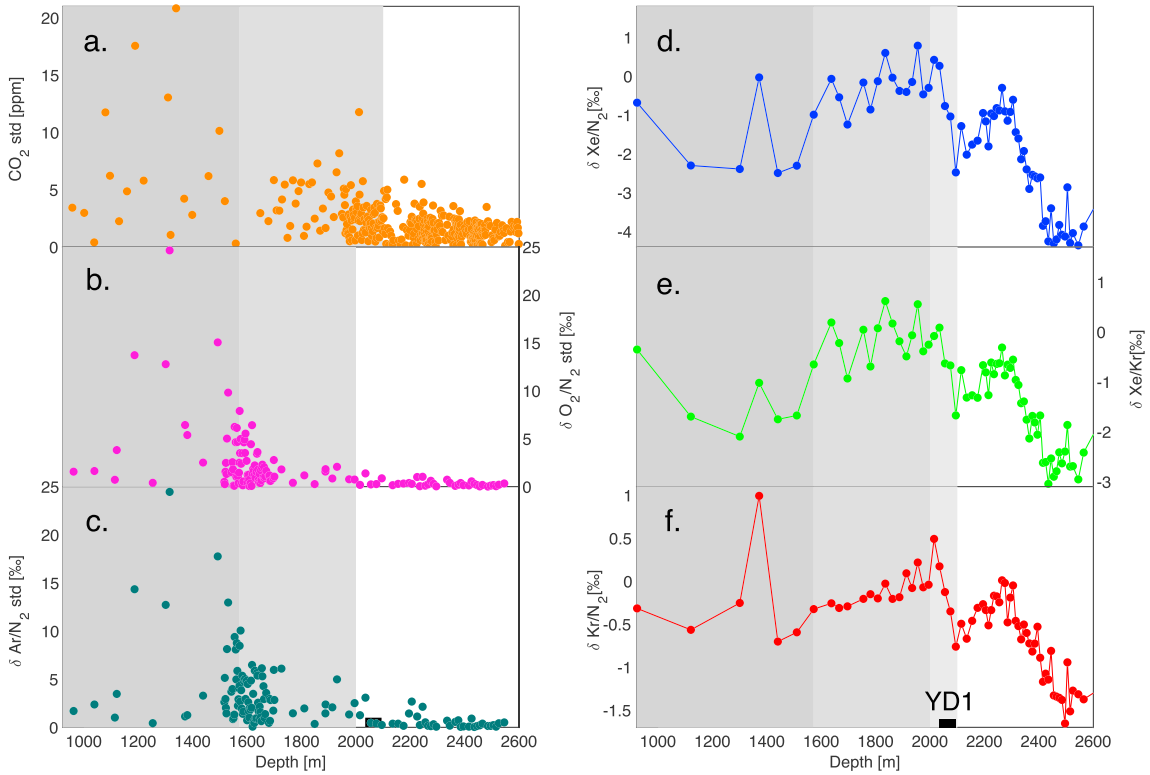

Figure 2.3. Evidence for spatial fractionation of noble gas ratios in and below the bubble-clathrate transition zone (BCTZ) at WAIS Divide. Standard deviations for replicate measurements of (a) CO2 (this study and Marcott et al., 2014), (b) O2/N2, and (c) Ar/N2 (Seltzer et al., 2017) versus depth. Dark gray paneling indicates the depth range of the BCTZ, and medium gray paneling marks the depth intervals below the BCTZ for which standard deviations are significantly elevated compared to the deepest (2,500–2,600 m) depth interval. Gravitationally and thermally corrected (d) Xe/N2, (e) Xe/Kr, and (f) Kr/N2 within and below BCTZ (Bereiter, Kawamura, et al., 2018; Bereiter, Shackleton, et al., 2018). Dark gray paneling indicates the depth range of the BCTZ, medium gray paneling marks the depth intervals where standard deviations for all three indicator gases are elevated, and light gray paneling marks where only standard deviations of CO2 show significant elevation. Black bar indicates the YD1 depth interval.

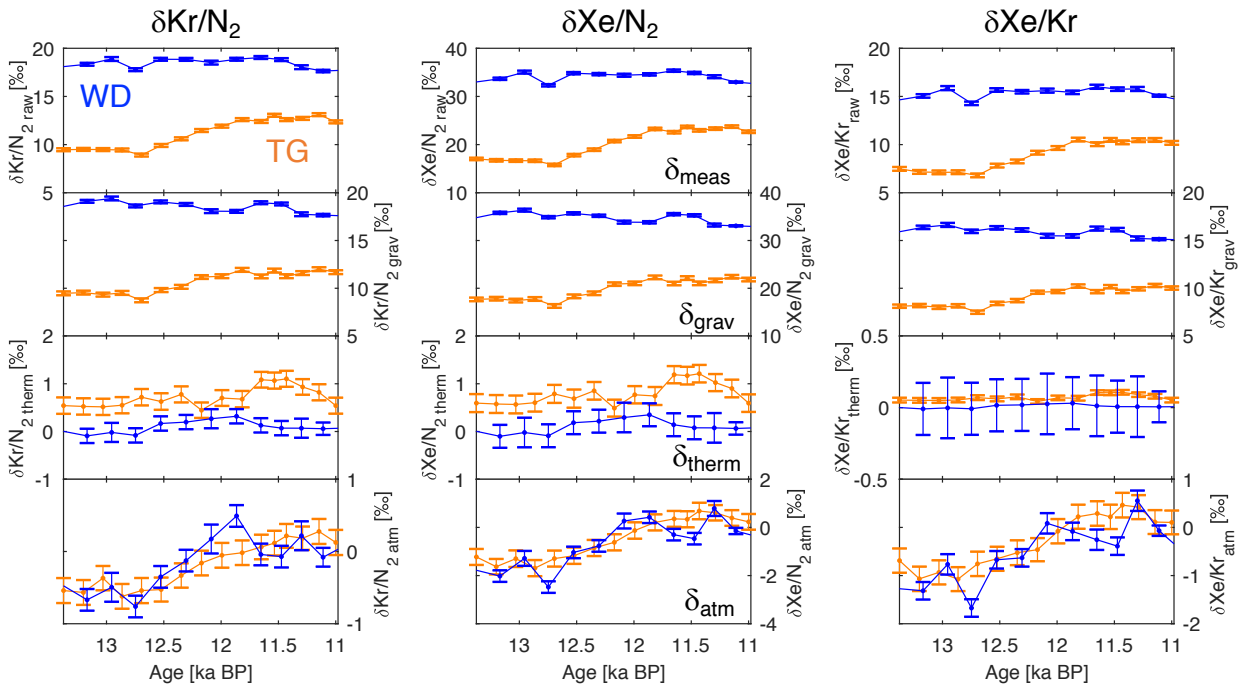

Figure 2.S1. Comparison of WAIS Divide (WD, blue) and Taylor Glacier (TG, orange) $\delta Kr/N_2$, $\delta Xe/N_2$ and $\delta Xe/Kr$ measurements (top panel), firn fractionations (middle panels), and atmospheric content (bottom panel). TG firn fractionations are calculated using the linear least squares method, and error bars are calculated from 10,000 Monte Carlo simulations of the linear least squares solutions (for the thermal and gravitational fractionation) that incorporate analytical uncertainties in all isotopic and elemental ratios. WD error bars are the analytical uncertainties of the respective noble gas ratios from Bereiter et al., 2018. The atmospheric noble gas ratios (bottom panel) results from the measured ratios (top panel) minus the gravitational (second panel) and thermal (third panel) fractionations for TG and WD respectively.

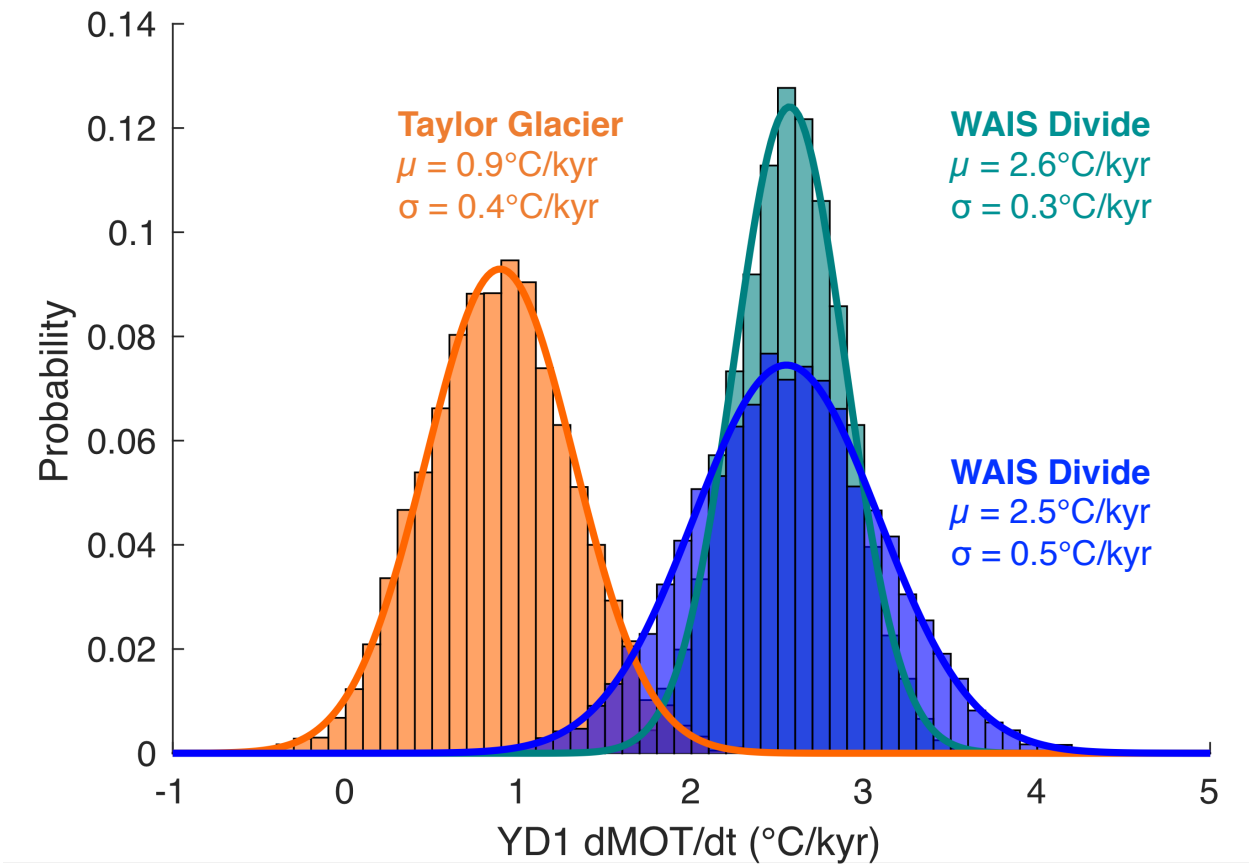

Figure 2.S2. Histograms and inferred probability distribution functions of the YD1 warming rate for Taylor Glacier and WAIS Divide. Histograms show the results of 10,000 Monte Carlo simulations of the MOT data. WAIS Divide simulations are conducted using the published MOT error bars (blue, Bereiter et al., 2018), and with the analytical routine used for Taylor Glacier in this study (teal).

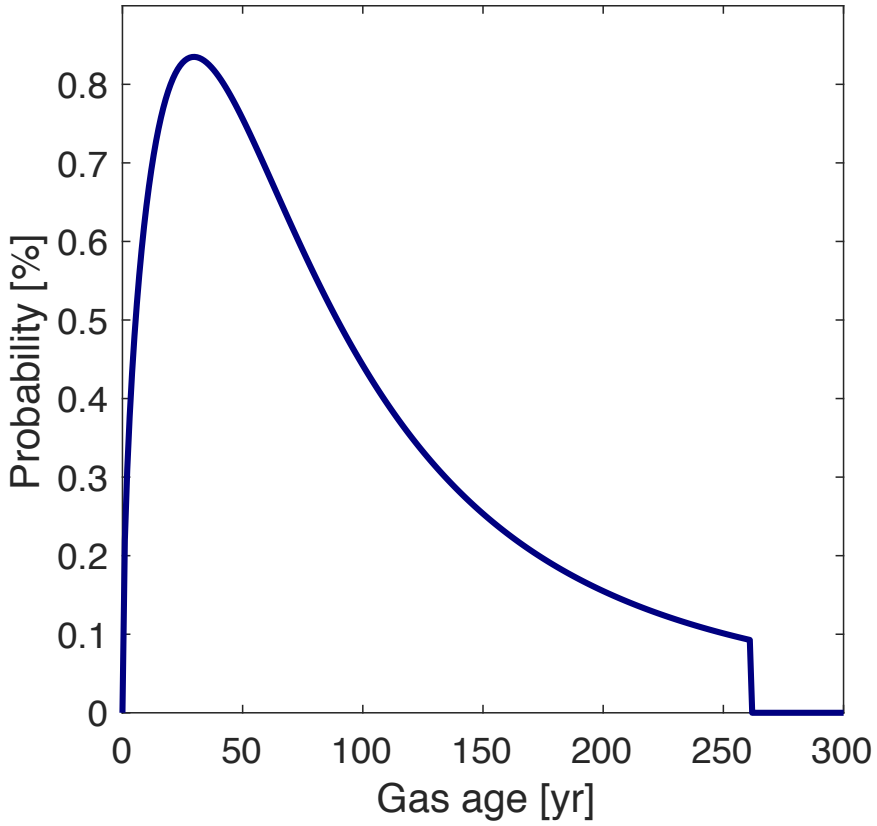

Figure 2.S3. Example of a log-logistic gas age distribution function with a width of 100 years and β value of 1.5. The gas age distribution is truncated at three times the median age (α) to prevent unphysically long tails (Spahni et al., 2003).

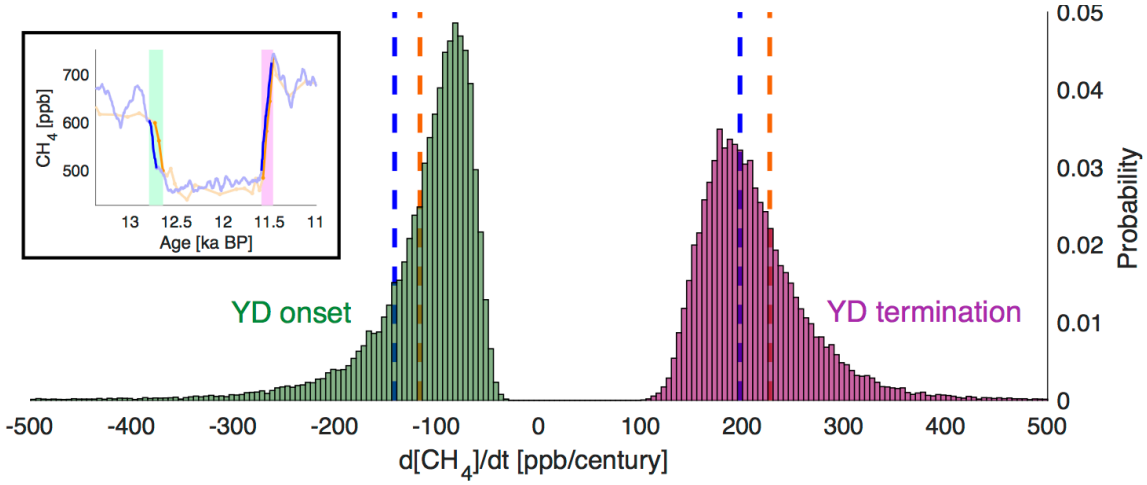

Figure 2.S4. Probability distributions from Monte Carlo simulations for Taylor Glacier d[CH_4]/dt at the Younger Dryas onset (green) and termination (magenta). Blue dashed lines show WAIS Divide d[CH_4]/dt for the onset and termination. Orange dashed lines show the same for the Taylor Glacier data. Inset shows the Taylor Glacier (orange, Bauska et al., 2016) and WAIS Divide (blue, Rhodes et al., 2015) CH_4 data. The green bar highlights the WAIS Divide and Taylor Glacier data for comparison of d[CH_4]/dt at the Younger Dryas onset. Magenta bar shows the same for the Younger Dryas termination.

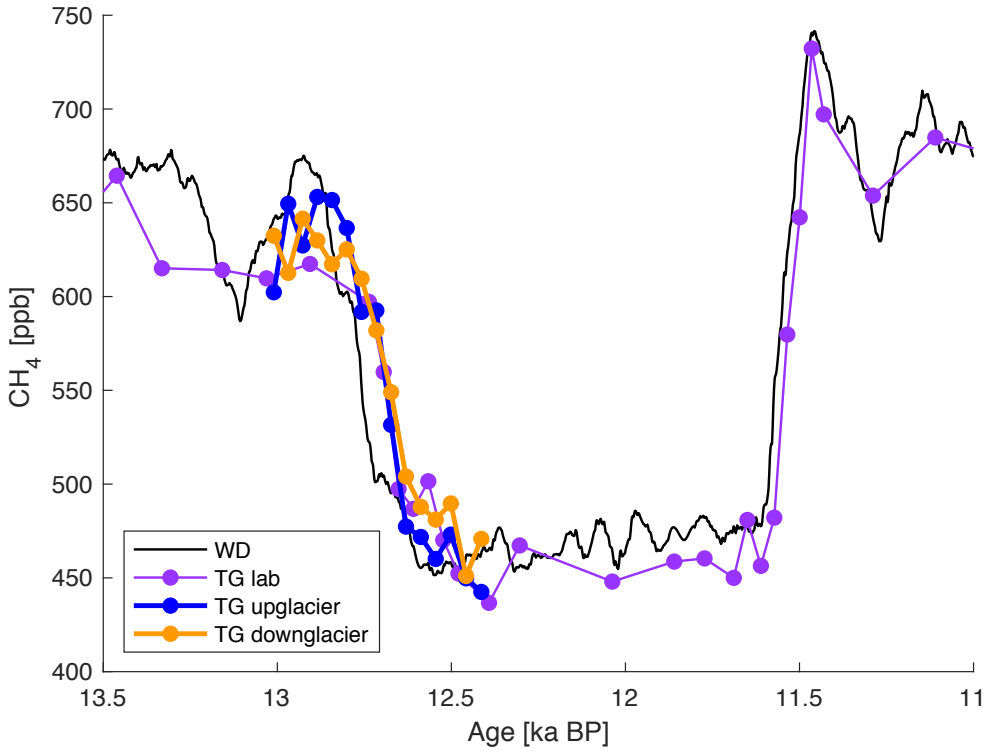

Figure 2.S5. CH_4 field measurements at Taylor Glacier (TG, Bauska et al., 2016) compared to laboratory measurements and WAIS Divide (WD, Rhodes et al., 2015). Taylor Glacier samples are plotted on the Taylor Glacier timescale using only $\delta^{18}O_{atm}$. Field measurements (upglacier and downglacier) were adjusted by 17.2 ppb to account for field-lab offsets.

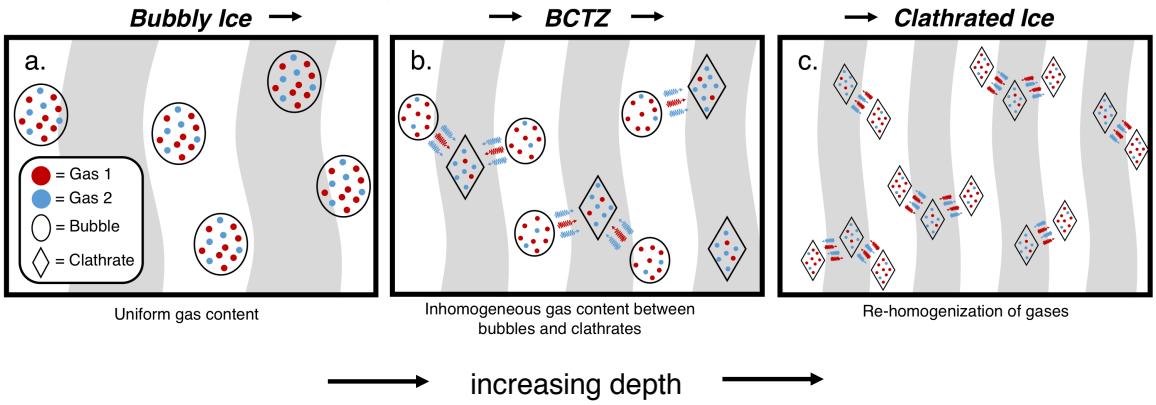

Figure 2.S6. Schematic of the steps involved in the clathrate layering hypothesis. Depth increases from left to right. Gray/white shading represents layers of variable impurity content. a) Depth range with bubbles (open circles) only. Bubbles have homogeneous gas concentrations. b) Depth range where clathrate (diamonds) formation occurs, preferentially in layers with impurities that promote clathrate nucleation. Gases permeate from bubbles to clathrates at differing rates (gas 2 > gas 1 in this schematic), causing a relative enrichment of gases with higher permeation rates in clathrates and depletion in bubbles, and vice versa for the slower permeating gases. c) Depth range just below the BCTZ where ice is fully clathrated, but clathrates have not fully homogenized. The thinning of layers with depth enhances diffusion and re-homogenization of gases.

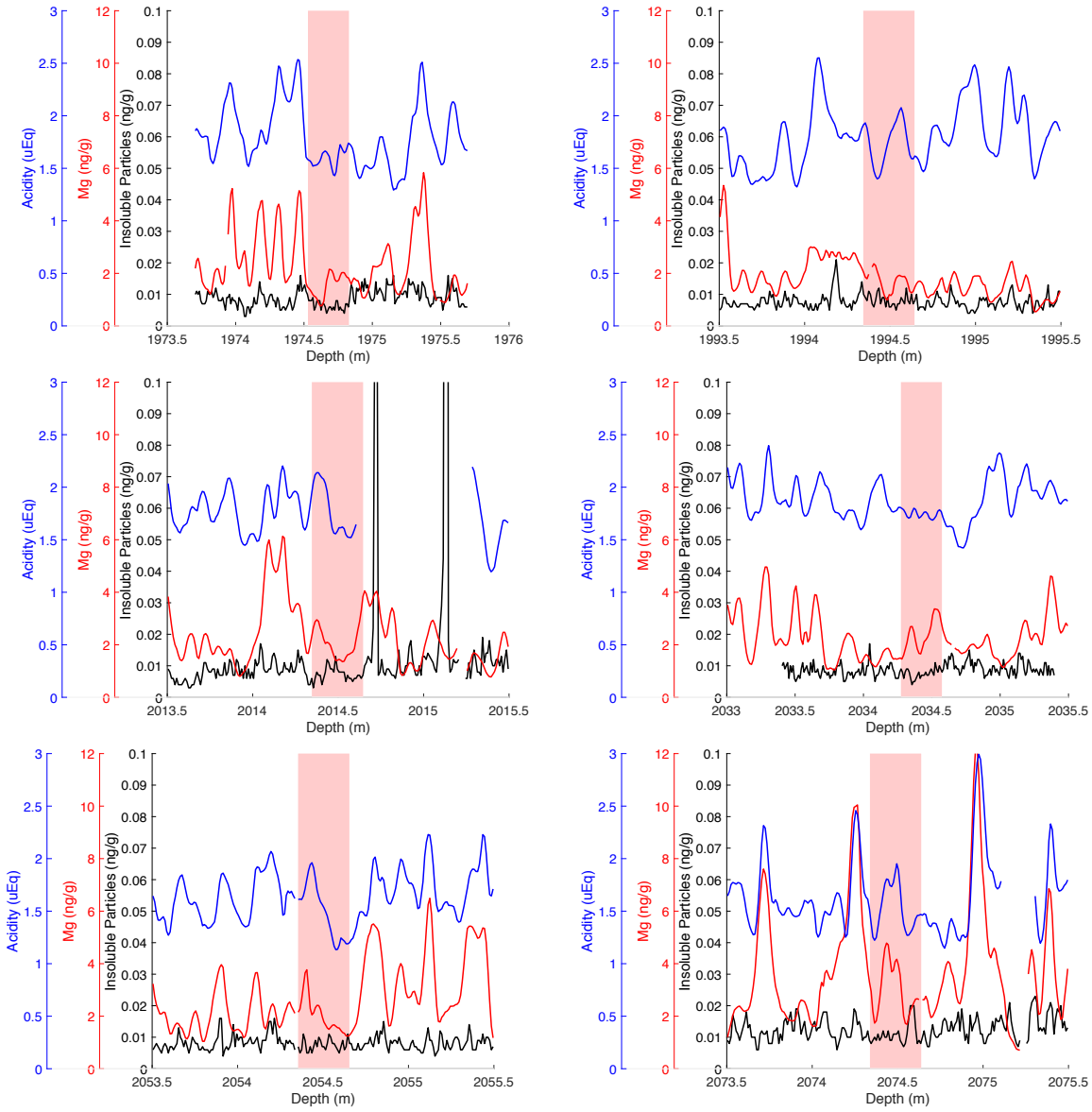

Figure 2.S7. Ice impurities in WAIS Divide noble gas samples from the Younger Dryas interval. Insoluble particles (black), acidity (blue), and Mg content (red) of ice (Sigl et al., 2016, Data DOI: 10.15784/601008), all of which are believed to directly or indirectly contribute to clathrate nucleation and thus clathrate layering. Pink panel indicates the depth interval sampled for noble gases for MOT reconstruction.

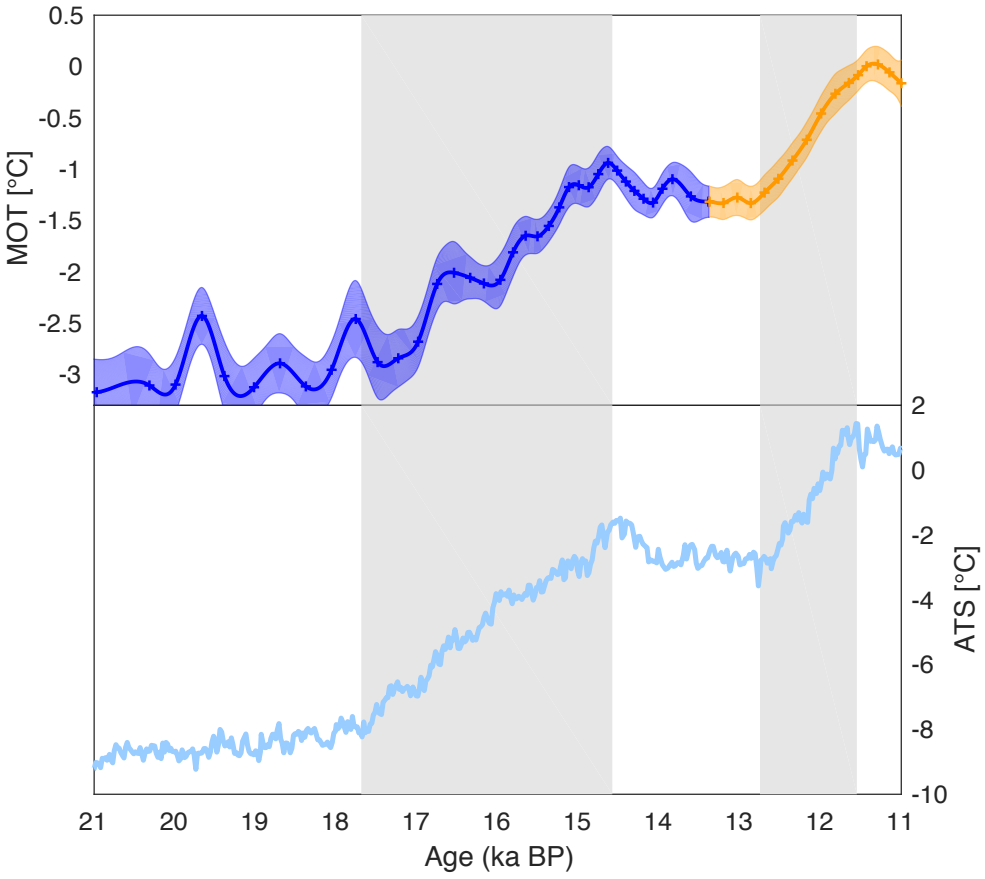

Figure 2.S8. Combined WD and Taylor Glacier spline and Antarctic Temperature. Top panel: splined MOT data for the last deglaciation with combined WD (blue) and Taylor Glacier (orange) data. Spline was created using the same parameterizations as in Bereiter, Shackleton, et al., (2018). Xs indicate where MOT data used to produce spline are located. Bottom panel: Antarctic temperature stack (Parrenin et al., 2013). Gray bars indicate the Heinrich Stadial 1 (HS1) and Younger Dryas (YD) intervals.

Table 2.S1. Comparisons in the rates of CH_4 change for Taylor Glacier and WAIS Divide used to constrain the gas age distribution for Taylor Glacier. Taylor Glacier rates in parentheses are the 95th and 5th percentiles of the Monte Carlo distributions of d[CH_4]/dt for the Younger Dryas onset and termination respectively. These values are used to predict the upper bound on smoothing of the Taylor Glacier MOT record.

	WAIS Divide (ppb/century)	**Taylor Glacier (ppb/century)**	**TG rate reduction (%)**	**TG max rate reduction (%)**
YD onset	-142	-117 (-58)	18	59
YD termination	197	227 (147)	0	26

References

Baggenstos, D. (2015). *Taylor Glacier as an archive of ancient ice for large-volume samples: Chronology, gases, dust, and climate*. University of California, San Diego.

Baggenstos, D., Bauska, T. K., Severinghaus, J. P., Lee, J. E., Schaefer, H., Buizert, C., Brook, E. J., Shackleton, S., & Petrenko, V. V. (2017). Atmospheric gas records from Taylor Glacier, Antarctica, reveal ancient ice with ages spanning the entire last glacial cycle. *Climate of the Past*, *13*(7), 943–958. https://doi.org/10.5194/cp-13-943-2017

Bauska, T. K., Baggenstos, D., Brook, E. J., Mix, A. C., Marcott, S. A., Petrenko, V. V, Schaefer, H., Severinghaus, J. P., & Lee, J. E. (2016). Carbon isotopes characterize rapid changes in atmospheric carbon dioxide during the last deglaciation. *Proceedings of the National Academy of Sciences*, *113*(13), 3465–3470. https://doi.org/10.1073/pnas.1513868113

Bender, M. L., Sowers, T., & Lipenkov, V. (1995). On the concentrations of O2, N2, and Ar in trapped gases from ice cores. *Journal of Geophysical Research*, *100*, 18651–18660. https://doi.org/10.1029/94jd02212

Bereiter, B., Schwander, J., Lüthi, D., & Stocker, T. F. (2009). Change in CO2 concentration and O2/N2 ratio in ice cores due to molecular diffusion. *Geophysical Research Letters*, *36*(5). https://doi.org/10.1029/2008GL036737

Bereiter, B., Shackleton, S., Baggenstos, D., Kawamura, K., & Severinghaus, J. (2018). Mean global ocean temperatures during the last glacial transition. *Nature*, *553*(7686), 39–44. https://doi.org/10.1038/nature25152

Bereiter, B., Kawamura, K., & Severinghaus, J. P. (2018). New methods for measuring atmospheric heavy noble gas isotope and elemental ratios in ice core samples. *Rapid Communications in Mass Spectrometry*, *32*(10), 801–814. https://doi.org/10.1002/rcm.8099

Blunier, T., Schwander, J., Stauffer, B., Stocker, T., Dällenbach, A., Indermühle, A., Tschumi, J., Chappellaz, J., Raynaud, D., & Barnola, J.-M. (1997). Timing of the Antarctic cold reversal and the atmospheric CO 2 increase with respect to the Younger Dryas Event. *Geophysical Research Letters*, *24*(21), 2683–2686. https://doi.org/10.1029/97GL02658

Broecker, W. S., Andree, M., Wolfli, W., Oeschger, H., Bonani, G., Kennett, J., & Peteet, D. (1988). The chronology of the last Deglaciation: Implications to the cause of the Younger Dryas Event. *Paleoceanography*, *3*(1), 1–19. https://doi.org/10.1029/PA003i001p00001

Broecker, W. S., Kennett, J. P., Flower, B. P., Teller, J. T., Trumbore, S., Bonani, G., & Wolfli, W. (1989). Routing of meltwater from the Laurentide Ice Sheet during the Younger Dryas cold episode. *Nature*, *341*(6240), 318–321. https://doi.org/10.1038/341318a0

Buizert, C., Cuffey, K. M., Severinghaus, J. P., Baggenstos, D., Fudge, T. J., Steig, E. J., Markle,

B. R., Winstrup, M., Rhodes, R. H., Brook, E. J., Sowers, T. A., Clow, G. D., Cheng, H., Edwards, R. L., Sigl, M., McConnell, J. R., & Taylor, K. C. (2015). The WAIS-Divide deep ice core WD2014 chronology – Part 1 : Methane synchronization (68 – 31 ka BP) and the gas age-ice age difference. *Climate of the Past*, *11*, 153. https://doi.org/10.5194/cp-11-153-2015

Craig, H., Horibe, Y., & T., S. (1988). Gravitational Seperation of Gases and Isotopes in Polar Ice Caps. *Science*, *242*(4886), 1675–1678. https://doi.org/10.1126/science.242.4886.1675

Faria, H., Freitag, J., & Kipfstuhl, S. (2010). Polar ice structure and the integrity of ice-core paleoclimate records. *Quaternary Science Reviews*, *29*, 338–351. https://doi.org/10.1016/j.quascirev.2009.10.016

Fitzpatrick, J. J., Voigt, D. E., Fegyveresi, J. M., Stevens, N. T., Spencer, M. K., Cole-dai, J., Alley, R. B., Jardine, G. E., Cravens, E. D., Wilen, L. A., Fudge, T. J., & Mcconnell, J. R. (2014). Physical properties of the WAIS Divide ice core. *Journal of Glaciology*, *60*(224), 1181–1198. https://doi.org/10.3189/2014JoG14J100

Galbraith, E. D., Merlis, T. M., & Palter, J. B. (2016). Destabilization of glacial climate by the radiative impact of Atlantic Meridional Overturning Circulation disruptions. *Geophysical Research Letters*, *43*(15), 8214–8221. https://doi.org/10.1002/2016GL069846

Headly, M. A., & Severinghaus, J. P. (2007). A method to measure Kr/N2 ratios in air bubbles trapped in ice cores and its application in reconstructing past mean ocean temperature. *Journal of Geophysical Research*, *112*(19), 1–12. https://doi.org/10.1029/2006JD008317

Kobashi, T., Severinghaus, J. P., & Kawamura, K. (2008). Argon and nitrogen isotopes of trapped air in the GISP2 ice core during the Holocene epoch (0 – 11 , 500 B . P .): Methodology and implications for gas loss processes Author ' s personal copy. *Geochimica et Cosmochimica Acta*, *72*, 4675–4686. https://doi.org/10.1016/j.gca.2008.07.006

Lambeck, K., Rouby, H., Purcell, A., Sun, Y., & Sambridge, M. (2014). Sea level and global ice volumes from the Last Glacial Maximum to the Holocene. *Proceedings of the National Academy of Sciences*, *111*(43), 15296–15303. https://doi.org/10.1073/pnas.1411762111

Levitus, S., Antonov, J. I., Boyer, T. P., Baranova, O. K., Garcia, H. E., Locarnini, R. A., Mishonov, A. V, Reagan, J. R., Seidov, D., Yarosh, E. S., & Zweng, M. M. (2012). World ocean heat content and thermosteric sea level change (0-2000m), 1955-2010. *Geophysical Research Letters*, *39*(10), 1–5. https://doi.org/10.1029/2012GL051106

Lipenkov, V. Y. (2000). Air bubbles and air-hydrate crystals in the Vostok ice core. In T. Hondoh (Ed.), *Physics of Ice Core Records* (pp. 327–358). Hokkaido University Press.

Lisiecki, L. E., & Lisiecki, P. A. (2002). Application of dynamic programming to the correlation of paleoclimate records. *Paleoceanography*, *17*(4), 1-1-1–12. https://doi.org/10.1029/2001PA000733

Lüthi, D., Bereiter, B., Stauffer, B., Winkler, R., Schwander, J., Kindler, P., Leuenberger, M., Kipfstuhl, S., Capron, E., Landais, A., Fischer, H., & Stocker, T. F. (2010). CO2 and O2/N2 variations in and just below the bubble-clathrate transformation zone of Antarctic ice cores. *Earth and Planetary Science Letters*, *297*(1–2), 226–233. https://doi.org/10.1016/j.epsl.2010.06.023

Marcott, S. A., Bauska, T. K., Buizert, C., Steig, E. J., Rosen, J. L., Cuffey, K. M., Fudge, T. J., Severinghaus, J. P., Ahn, J., Kalk, M. L., McConnell, J. R., Sowers, T., Taylor, K. C., White, J. W. C., & Brook, E. J. (2014). Centennial-scale changes in the global carbon cycle during the last deglaciation. *Nature*, *514*(7524), 616–619. https://doi.org/10.1038/nature13799

McManus, J. F., Francois, R., Gherardl, J. M., Kelgwin, L., & Drown-Leger, S. (2004). Collapse and rapid resumption of Atlantic meridional circulation linked to deglacial climate changes. *Nature*, *428*(6985), 834–837. https://doi.org/10.1038/nature02494

Ohno, H., Lipenkov, V. Y., & Hondoh, T. (2010). Formation of air clathrate hydrates in polar ice sheets: heterogeneous nucleation induced by micro-inclusions. *Journal of Glaciology*, *56*(199), 917–921.

Parrenin, F., Masson-Delmotte, V., Köhler, P., Raynaud, D., Paillard, D., Schwander, J., Barbante, C., Landais, A., Wegner, A., & Jouzel, J. (2013). Synchronous change of atmospheric CO2and antarctic temperature during the last deglacial warming. *Science*, *339*(6123), 1060–1063. https://doi.org/10.1126/science.1226368

Pedro, J. B., Jochum, M., Buizert, C., He, F., Barker, S., & Rasmussen, S. O. (2018). Beyond the bipolar seesaw: Toward a process understanding of interhemispheric coupling. *Quaternary Science Reviews*, *192*, 27–46. https://doi.org/10.1016/j.quascirev.2018.05.005

Rhodes, R. H., Brook, E. J., Chiang, J. C. H., Blunier, T., Maselli, O. J., McConnell, J. R., Romanini, D., & Severinghaus, J. P. (2015). Enhanced tropical methane production in response to iceberg discharge in the North Atlantic. *Science*, *348*(6238), 1016–1019. https://doi.org/10.1126/science.1262005

Ritz, S. P., Stocker, T. F., & Severinghaus, J. P. (2011). Noble gases as proxies of mean ocean temperature : sensitivity studies using a climate model of reduced complexity. *Quaternary Science Reviews*, *30*(25–26), 3728–3741. https://doi.org/10.1016/j.quascirev.2011.09.021

Schwander, J. (1989). The transformation of snow to ice and the occlusion of gases. In H. Oeschger & C. C. Langway (Eds.), *The Environmental Record in Glaciers and Ice Sheets* (pp. 53–67).

Schwander, J., Stauffer, B., & Sigg, A. (1988). Air mixing in firn and the age of the air at pore close-off. *Annals of Glaciology*, *10*, 141–145. https://doi.org/10.1017/S0260305500004328

Seltzer, A. M., Buizert, C., Baggenstos, D., Brook, E. J., Ahn, J., Yang, J.-W., & Severinghaus, J. P. (2017). Does d18O of O2 record meridional shifts in tropical rainfall? *Climate of the Past*, *13*(10), 1323–1338. https://doi.org/10.5194/cp-13-1323-2017

Severinghaus, J. P., Sowers, T., Brook, E. J., Alley, R. B., & Bender, M. L. (1998). Timing of abrupt climate change at the end of the younger dryas interval from thermally fractionated gases in polar ice. *Nature*, *391*(6663), 141–146. https://doi.org/10.1038/34346

Shimada, W., & Hondoh, T. (2004). In situ observation of the transformation from air bubbles to air clathrate hydrate crystals using a Mizuho ice core. *Journal of Crystal Growth*, *265*, 309–317. https://doi.org/10.1016/j.jcrysgro.2004.01.040

Sigl, M., Fudge, T. J., Winstrup, M., Cole-Dai, J., Ferris, D., McConnell, J. R., Taylor, K. C., Welten, K. C., Woodruff, T. E., Adolphi, F., Bisiaux, M., Brook, E. J., Buizert, C., Caffee, M. W., Dunbar, N. W., Edwards, R., Geng, L., Iverson, N., Koffman, B., et al. (2016). The WAIS Divide deep ice core WD2014 chronology - Part 2: Annual-layer counting (0-31 ka BP). *Climate of the Past*, *12*(3), 769–786. https://doi.org/10.5194/cp-12-769-2016

Spahni, R., Schwander, J., Fluckiger, J., Stauffer, B., Chappellaz, J., & Raynaud, D. (2003). The attenuation of fast atmospheric CH4 variations recorded in polar ice cores. *Geophysical Research Letters*, *30*(11), 1571. https://doi.org/10.1029/2003GL017093

Stauffer, B., & Tschumi, J. (2000). Reconstruction of past atmospheric CO2 concentrations by ice core analyses. In T. Hondoh (Ed.), *Physics of Ice Core Records* (pp. 217–241). Hokkaido University Press.

Stieglitz, J. L., Schmidt, M. W., & Curry, W. B. (2011). Evidence from the Florida Straits for Younger Dryas ocean circulation changes. *Paleoceanography*, *26*(PA1205), 1–11. https://doi.org/10.1029/2010PA002032

Chapter 3

Exposing Systematic Error in Mean Ocean Temperature Reconstructions

3.1. Introduction

Age uncertainties in paleoclimate records are one of the major impediments to understanding the mechanisms that drive past climate change (Govin et al., 2015; Rasmussen et al., 2014). This problem is especially acute for the comparison of ice core and sediment core records and obstructs our ability to determine the relative timing of ocean and atmospheric changes that would provide crucial insight into climate feedbacks. The recently developed noble gas mean ocean temperature (MOT) proxy (Headly & Severinghaus, 2007) represents a substantial advance on this front, because it provides information about total ocean heat content on the ice core time scale, with zero age uncertainty relative to greenhouse gas and other gas records from the same core.

Since the development of the proxy, the analytical precision of the inert gas measurements have markedly improved (Bereiter, Kawamura, et al., 2018). It is therefore prudent to revisit potential sources of systematic error in MOT reconstructions that were previously considered insignificant, as they may now exceed analytical uncertainty.

There are two general ways in which ice core inert gas ratios ($\delta Kr/N_2$, $\delta Xe/N_2$, and $\delta Xe/Kr$) and ocean heat content can become uncoupled, so that the inert gas ratios measured in ice cores do

not reflect mean ocean temperature and create systematic error. The first is through processes that decouple gas ratios in the well-mixed atmosphere from ocean heat content. Known cases of this potential source of systematic error in MOT include cooling under sea ice (Ritz et al., 2011), rapid cooling and sinking during deep water formation (Hamme & Severinghaus, 2007) and geothermal heating of ocean water at depth (Headly & Severinghaus, 2007). Several of these processes have been studied through modeling experiments (Ritz et al., 2011). If this type of MOT-inert gas decoupling occurred in the past, it would introduce systematic error to MOT results for all ice core records.

The second way to uncouple the ice core inert gases from MOT is through decoupling the inert gas content of glacial ice from that of the well-mixed atmosphere through fractionation of atmospheric gases during firnification or within the ice. The turbulent mixing of gases within the firn is significantly reduced compared to the free atmosphere (Schwander et al., 1988), allowing for diffusive fractionation processes such as gravitational (Craig et al., 1988), thermal (Severinghaus et al., 1998), and kinetic (Birner et al., 2018; Buizert & Severinghaus, 2016; Kawamura et al., 2013) fractionation to un-mix atmospheric gases before they are occluded in ice bubbles (Figure 1). This un-mixing influences all ice core records, making fractionation corrections necessary in order to derive MOT from the measured inert gas ratios. While all ice cores are subject to these sources of fractionation, variable site conditions make the extent of fractionation different for each site. If not appropriately accounted for, this second type of decoupling will result in error in MOT reconstructions that is potentially unique to each ice core. Because the atmosphere is well mixed on annual timescales, and a single ice core sample contains gases with a distribution of ages that spans much more than a year (Spahni et al., 2003), all ice core records should contain the same atmospheric inert gas history. It may therefore be possible to

identify this type of systematic error through the comparison of multiple ice core records over the same time interval.

Two recent MOT reconstructions replicated either part (Shackleton et al., 2019) or all (Baggenstos et al., 2019) of the pioneering WAIS Divide MOT record of the last deglaciation (Bereiter, Shackleton, et al., 2018) using ice cores from Taylor Glacier and EPICA Dome C (EDC) respectively. Both studies found inconsistencies with the WAIS Divide MOT results that could not be explained by analytical noise and must be related to inadequate corrections for fractionation processes that occurred either during firnification or within the ice. Because these studies covered intervals when atmospheric $\delta Kr/N_2$, $\delta Xe/N_2$, and $\delta Xe/Kr$ are unknown, it was not possible to definitively accept or reject any of the proposed MOT histories from the different ice core reconstructions.

To address this fractionation problem, here we measure $\delta Kr/N_2$, $\delta Xe/N_2$, and $\delta Xe/Kr$ in firn air and near-surface ice samples. Because these samples contain modern air, the measured $\delta Kr/N_2$, $\delta Xe/N_2$, and $\delta Xe/Kr$ in the firn air and surface ice samples are only influenced by fractionating processes within the firn or ice, rather than atmospheric changes in $\delta Kr/N_2$, $\delta Xe/N_2$, and $\delta Xe/Kr$ due to changes in MOT. We then correct the measured $\delta Kr/N_2$, $\delta Xe/N_2$, and $\delta Xe/Kr$ for fractionating processes to test our ability to reconstruct atmospheric $\delta Kr/N_2$, $\delta Xe/N_2$, and $\delta Xe/Kr$. If the samples are adequately corrected for fractionations, the corrected $\delta Kr/N_2$, $\delta Xe/N_2$, and $\delta Xe/Kr$ values should be zero (within analytical error), relative to the modern air standard they are measured against. By applying fractionation corrections to samples with *a priori* known atmospheric $\delta Kr/N_2$, $\delta Xe/N_2$, and $\delta Xe/Kr$, it may be possible to expose systematic errors in MOT reconstructions associated with fractionating processes within the firn/ice, identify their sources, quantify their magnitudes, and suggest methods to minimize their influence in future MOT studies.

3.2. Methods

3.2.1. Fractionation Corrections

The general approach to correct $\delta Kr/N_2$, $\delta Xe/N_2$, and $\delta Xe/Kr$ (referred to collectively as inert gas ratios for the remainder of this study) measured in ice for firn fractionations is through the use of isotope measurements of inert gases such as nitrogen, argon, and krypton to diagnose their source and extent. This strategy relies on the fact that these isotopes are essentially constant in the atmosphere on the timescales considered here, so the firn fractionations are the only processes that affect them. Often, additional information is used to estimate the sources of fractionation in MOT studies, such as a firn thermal model to correct for thermal fractionation (Baggenstos et al., 2019; Bereiter, Shackleton, et al., 2018). In this study we consider methods that exclusively use measured isotope data to correct the inert gas ratios for firn fractionations. Eight methods of fractionation corrections for MOT studies are considered, that can be divided into two correction types (Table 1).

The first correction type we consider is the process-based least-squares method, of which we consider four different methods (Baggenstos, 2015; Shackleton et al., 2019). This approach is described in detail in the Appendix of Chapter 4 of this thesis. In short, this method employs a linear system of isotope measurements to quantify the sources of each fractionation by solving for diffusive column height (gravitational fractionation), firn thermal gradient (thermal fractionation), and heavy isotope deficit (kinetic fractionation, Birner et al., 2018). These outputs are then used to quantify and correct for the influence of each fractionation on the inert gas ratios and reconstruct their atmospheric values. To distinguish between the inert gas ratios that are measured in firn/ice from corrected values that should reflect the atmospheric $\delta Kr/N_2$, $\delta Xe/N_2$, and $\delta Xe/Kr$, we refer

to the corrected inert gas ratios as the 'atmospheric proxies'. We emphasize that deviations of the atmospheric proxies from zero in this study do not reflect changes in MOT, but instead are due to error in the fractionation corrections of the inert gas ratios.

The second correction type we consider is the isotope-based approach, of which we consider four different methods (Table 1). Instead of quantifying the different sources of fractionation to correct the inert gas ratios, this method takes advantage of the fact that certain isotopes and inert gas ratios have similar mass-normalized sensitivities to fractionations. If the inert gas ratios were only influenced by gravitational fractionation, only one isotope measurement would be necessary to derive the atmospheric proxies, because gravitational fractionation is proportional to mass difference. However, if thermal or kinetic fractionation is also present, it is advantageous to correct each inert gas ratio with an isotope ratio that has a similar mass-normalized thermal and kinetic sensitivity. For instance, the $^{40}Ar/^{36}Ar$ thermal sensitivity happens to be similar to that of $^{84}Kr/^{28}N_2$ on a per-mass-unit-difference basis, as is exactly true for gravitational settling. Using the argon isotopes to correct $\delta Kr/N_2$ therefore reduces any error that may arise from inaccurate partitioning of the fractionation into gravitational and thermal components:

$$\delta' Kr/N_{2\,corr} = \delta' Kr/N_{2\,meas} - \frac{56}{4} \times \delta'^{40} Ar_{meas}$$

In this case (and also in the case of the process-based methods), we use δ' instead of the customary δ, where $\delta' = \ln(q)$ and $q = R_{sample}/R_{standard}$. Because the customary δ is the more common notation, we convert back to δ (reported in per mil) for our reported atmospheric proxies:

$$\delta = \left[e^{\delta'} - 1\right] \times 1000$$

We anticipate some error in the atmospheric proxies due analytical uncertainties in the measurement of the inert gas ratios and the isotopes used to correct them. We also expect there to be some correlation in the error between the atmospheric proxies for all methods, because any

analytical error in the isotopes used to correct the inert gas ratios will affect all three atmospheric proxies. To assess whether the error in the atmospheric proxies differs significantly more than what is expected due to analytical uncertainties, we run Monte Carlo simulation of each correction method with all analytical uncertainties to estimate the expected total analytical error for the atmospheric proxies. We may then compare the expected analytical errors to the atmospheric proxy results for firn air and surface ice samples to determine whether the results fall within the expected range of analytical uncertainty, or if there is additional systematic error in the atmospheric proxies for each of the correction methods (see Appendix).

3.2.2. Firn Air Samples

We consider the results of previously published firn air studies with measured inert gas ratios (Kawamura et al., 2013; Orsi, 2013; Severinghaus & Battle, 2006) from South Pole (SP01), Siple Dome (SDM), and Megadunes (MD), as well as new measurements from Summit (GISP2), NEEM, Dome Fuji (DF) and a resampling of South Pole (SP15). To assess the different methods of fractionation correction, we only consider firn air samples below 20 m depth to avoid the influence of seasonal temperature variations. In addition, we compare results within and outside of the lock-in zone, where horizontal layering largely inhibits vertical air motion. As certain processes, such as bubble-close off (Severinghaus & Battle, 2006) and dispersive mixing (Buizert & Severinghaus, 2016) are mostly restricted to the lock-in-zone, firn air samples within this depth interval may more closely represent the composition of gas that is occluded in air bubbles in glacial ice.

In our assessment of process-based correction methods, we only consider the sites that include nitrogen, argon, and krypton isotope measurements, because we do not want the presence/absence of a given predictor to influence the atmospheric proxy results. For Summit and

Megadunes, xenon isotopes were also measured, but not included in the analysis for this reason. To assess the expected analytical error, we estimate uncertainty from the pooled standard deviation of replicate measurements for each site. Specifics of the previously unpublished firn air campaigns are included in the Appendix.

3.2.3. Surface Ice Samples

In addition to firn air samples, we consider near-surface ice samples with ages within the last thousand years (Buizert et al., in prep). A total of 43 surface ice core samples were analyzed from eight ice core sites including South Pole (SP), WAIS Divide (WD), Siple Dome (SDM), Roosevelt Island (RICE), James Ross Island (JRI), Summit (GISP2) and two Law Dome sites (DE08 and DSSW20K). Of these 43 samples, three were rejected due to technical problems during sample extraction. All samples were measured using the same analytical method. This gives us more confidence that any differences in results between ice core sites are real and not due to laboratory offsets/artifacts.

An advantage of analyzing surface ice samples (compared to firn air) is that certain processes have the potential to influence gases in ice samples, yet these processes are not captured in the firn. One such process is the effect of 'artifactual' gas loss on the ice core samples (Bender et al., 1995; Ikeda-Fukazawa et al., 2005; Severinghaus et al., 2003). We define artifactual gas loss as any leakage of gas from an ice sample that does not occur naturally, but rather as the result of ice core drilling, handling, or storage. The inert gas ratios have exhibited alteration due to artifactual gas loss in clathrate ice with extreme gas loss from the deep Byrd core (Severinghaus, personal communication), from NEEM core clathrate ice that was allowed to warm to -5°C immediately after coring (Kawamura, personal communication), and within the bubble-clathrate transition zone (Bereiter, Kawamura, et al., 2018), but there has been no evidence of gas loss

influencing the inert gas ratios outside of these cases. However, evidence of argon isotope enrichment due to artifactual gas loss has been observed (Kobashi et al., 2008; Severinghaus et al., 2003), but not well understood. Artifactual enrichment of argon isotopes may introduce systematic error to the atmospheric proxies if they are used to make firn fractionation corrections.

Some of the surface ice samples considered in this study contain air that is several hundred years older than modern, and MOT has changed slightly over the last millennium. We therefore use model results of ocean temperature for the last two thousand years (Gebbie & Huybers, 2019) to account for any true change in the atmospheric proxies due to MOT change before evaluating the results for systematic error.

3.3. Results

3.3.1. Firn Air Assessment of Fractionation Corrections

As previously stated, we expect all atmospheric proxies to be zero (within analytical uncertainty) if there is no systematic error, because they contain modern air and are measured relative to a modern air standard. What we observe for the firn air samples is that all methods result in nonzero atmospheric proxy values, implying error in the atmospheric proxies that exceeds analytical error (Figure 3). We also find that the correlation in the biases between the atmospheric proxies exceeds what is expected from shared analytical error for all correction methods.

If our physical understanding of the processes that fractionate firn air is correct, we expect that the process-based gravitational-thermal-kinetic (PB-gtk) method will impart the least systematic error in the atmospheric proxies but will also result in the largest analytical error of any of the methods because we are using all three sets of isotope measurements (nitrogen, argon and krypton) to solve for the three sources of fractionation. While there is no apparent systematic error

in the corrected $\delta Kr/N_2$ from this method (0.0±0.3‰), a Student t-test of the corrected firn samples (n=81) shows significant negative bias in corrected $\delta Xe/N_2$ (-0.3±0.9‰, p=0.002) and $\delta Xe/Kr$ (-0.3±0.6‰, p<0.001). To place this in context, -0.3‰ corresponds to a MOT bias of -0.2°C for $\delta Xe/N_2$ and -0.3°C for $\delta Xe/Kr$.

If we assess the total error of the results by the root mean square deviation from zero, we find that the process-based gravitational-thermal (PB-gt) correction results in the least error in the atmospheric proxies. However, this method systematically introduces a negative bias for $\delta Kr/N_2$ (-0.1±0.2‰, p<0.001), $\delta Xe/N_2$ (-0.6±0.5‰, p<0.001) and $\delta Xe/Kr$ (-0.6±0.3‰, p<0.001). This systematically negative bias may be the result of not including a term for kinetic fractionation, which influences $\delta Xe/N_2$ and $\delta Xe/Kr$ more than $\delta Kr/N_2$ due to the lower diffusivity of xenon relative to krypton.

Considering results exclusively within the lock-in-zone, we find that the process-based gravitational-kinetic (PB-gk) correction method performs slightly better than the PB-gt correction, with results of +0.1±0.2‰, 0±0.7‰, and -0.1±0.5‰ for $\delta Kr/N_2$, $\delta Xe/N_2$, and $\delta Xe/Kr$ within the lock-in-zone respectively. Only the $\delta Kr/N_2$ lock-in-zone results show a statistically significant (p=0.003) bias for the PB-gk method. Because the firn air within the lock-in-zone is likely more representative of the air content occluded in glacial ice, based on these results we would posit that (besides gravitational fractionation) kinetic fractionation is the primary process that influences the inert gas ratios. However, as discussed in the following sections, the results are quite different for the surface ice samples.

3.3.2. Surface Ice Samples: Indication of Melt Layers

An initial examination of the results of the surface ice samples show that samples from JRI have significantly large and positive biases in the atmospheric proxies, regardless of correction

method (Figure 4). A two-sample Student t-test indicates that this site gives more positively biased results in the atmospheric proxies than the rest of the surface ice samples ($p<0.05$) for all correction methods and all atmospheric proxies. JRI is the warmest site considered in this study, and we suggest that the positive bias is the result of melt layers due to the warm surface temperatures at this site. Melt layers have been previously identified in ice cores from enriched $\delta Xe/Ar$ and $\delta Kr/Ar$ (Orsi et al., 2015). Because these are modern ice samples, we know that JRI results cannot be showing a true atmospheric signal. However, being able to identify melt in samples when MOT is unknown will be instrumental for future MOT studies.

Another key indication that the JRI samples are not showing a true atmospheric signal is the large scatter in these samples. Using an F-test to determine whether the JRI variance in atmospheric proxies is greater than the variance of the other sites, we find that for all correction methods except for PB-gtk, JRI had significantly ($p<0.05$) greater variance in the results for the atmospheric proxies than any of the other sites.

Orsi et al. (2015) showed that melt layers are not spatially uniform within ice cores. This is not a surprise, as we do not expect that melt events are uniformly distributed over time, or that their magnitudes are constant. We thus suggest that the high scatter in the atmospheric proxies are a good indicator of melt events and should be used as a basis for sample rejection in future MOT studies. Because the bias found for the JRI samples due to surface melt is quite different from what we expect from errors in firn fractionation corrections, we do not include the JRI site in our analysis for the remainder of this study.

3.3.3. Comparison of Firn Air and Surface Ice Results

Our assumption going into this study was that we should find similar results when comparing the correction methods applied to firn air and surface ice. While certain processes (such

as artifactual enrichment of argon isotopes due to gas loss) may influence the ice samples but not the firn, we expected the magnitude of these processes to be minimal, or only influence certain correction methods, but not others. To test this assumption, we ran a two-sample Student t-test comparing firn (n=81, no SP01 or SDM firn data) and ice (n=35, no JRI data) results for each of the 8 methods of correction and each of the three atmospheric proxies (24 tests). In all tests comparing corrected $\delta Xe/N_2$ and $\delta Xe/Kr$, we were able to reject the null hypothesis ($p<0.05$) that the firn and surface ice results were the same. For corrected $\delta Kr/N_2$ the null hypothesis could be rejected for 5 of the 8 cases. These results hold whether we compare the surface ice samples to all of the firn data, or firn air samples exclusively from the lock-in-zone (Figure 5).

One complication in comparing the firn and ice samples is that they come from different sites. To account for this, we also considered only the four locations where both firn and ice data are available, now including the data from Severinghaus & Battle (2006) only for the ISO-^{40}Ar and ISO-^{15}N correction methods and compare these subpopulations of the data using the two-sample Student t-test. These results are very similar to those that include all firn and ice sites. The only correction for which the null hypothesis could not be rejected was the ISO-^{40}Ar method. However, if we do not include the Severinghaus & Battle (2006) data, the results are virtually the same as those using the full populations of ice and firn, in or outside of the lock-in-zone.

This suggests that something is fundamentally different between the firn and ice samples. In the following sections, we discuss systematic error found in the ice samples, and the potential causes for the differences in the firn and ice data.

3.3.4. Surface Ice Systematic Error

Several patterns are apparent in the surface ice samples for all correction methods. The most notable is that the biases in corrected $\delta Xe/N_2$ and $\delta Kr/N_2$ are significantly and positively

correlated for all methods, beyond what may be explained by shared analytical error. In addition, the relative scaling of the biases in corrected $\delta Xe/N_2$ and $\delta Kr/N_2$ is similar to what we expect for changes in MOT (Figure 4). This is quite problematic for MOT reconstructions; previous studies have considered corrected $\delta Xe/N_2$ and $\delta Kr/N_2$ to be independent proxies for MOT, so their agreement provided confidence that a given MOT reconstruction was reliable. However, our results indicate that if systematic error is present, it will affect the resulting MOT derived from corrected $\delta Xe/N_2$ and $\delta Kr/N_2$ equally, so the agreement in these proxies cannot be used as a validation of the MOT results.

Another notable observation is that for most methods of corrections, there appears to be a systematic offset between sites, and the ordering (most positive to most negative) of this offset between sites does not change considerably between correction methods. In the case of most corrections (and excluding the JRI results), the surface ice samples from South Pole and Siple Dome tend to give the most positive atmospheric proxy results, and the Law Dome sites (DE08 and DSSW20K) give the most negative. This may indicate that there is a process that influences the inert gas ratios, but not the isotope ratios that are used to correct them.

3.3.5. Method for Minimization of Systematic Error

As in the case of the firn results, the PB-gt correction imparts the least error, as calculated by the smallest the root mean square deviation from zero. Considering all surface ice samples (excluding JRI, n=35), a Student t-test shows that there is no significant bias in the atmospheric proxies, and give average values of 0±0.2‰, 0.1±0.5‰, and 0.1±0.4‰ for corrected $\delta Kr/N_2$, $\delta Xe/N_2$, and $\delta Xe/Kr$ respectively. The spread in the data is slightly greater than what we predict for analytical noise. However, as mentioned in the previous section, random analytical error cannot

explain the significant correlation in the systematic bias we observe between the atmospheric proxies.

In addition to comparing the results of the four process-based and four isotope-based correction methods, we may also compare these results to an empirical correction. Because there is no atmospheric signal in the inert gas ratios measured in the firn and surface ice samples, they should only reflect the fractionation processes that decouple them from the atmosphere. We can thus invert the problem and test which linear combination of isotopes best represent the measured inert gas ratios. Comparing this empirical approach to the PB-gt correction, we find that the empirical method gives nearly identical results in systematic error as the PB-gt correction for all three atmospheric proxies and find that the systematic error observed between atmospheric proxies is still highly correlated, even if the empirical correction is calculated individually for each of the inert gas ratios. This supports the hypothesis that the systematic difference in atmospheric proxies is due to a process that influences the inert gas ratios, rather than the isotopes. Because the empirical correction uses no assumptions about the relationships between the isotopes and inert gas ratios, we use the results of this correction to consider possible explanations for the systematic error we observe in the ice samples.

3.4. Discussion: Causes of Systematic Error

3.4.1. Lab Artifacts

One potential explanation for the difference in results between the firn and ice is that they are the result of gas fractionation during processing within the lab or field. While much of the experimental method for firn air and ice core measurements are the same, the methods of gas extraction from the firn (Battle et al., 1996) and ice (Bereiter, Kawamura, et al., 2018) are quite

different. In the case of firn air, it is extracted in the field into glass or stainless-steel flasks that are later sampled in the lab for gas measurements.

In the case of ice samples, the gases are extracted from the ice in the lab, by melting the ice sample under vacuum in a >1 liter extraction vessel. After the sample is fully melted, it is stirred with a magnetic stir bar for an additional ~30 minutes to ensure a complete extraction. However, it may be possible that some of the gases are left behind, dissolved in the water from the melted ice. We tested this hypothesis by extracting an ice sample under the normal analytical procedure and then closing the evacuation off to sit overnight. Because the sample is left at vacuum, we expect that the majority of the remaining gases left in solution will enter the headspace.

The following day we extracted any remaining gases in the vessel. Before cryo-trapping the remaining gases, we opened the extraction vessel to the sample line to read the pressure, which increased to ~0.010 torr, indicating that there was still some gas left in the vessel, but only a miniscule fraction of what was collected from the initial extraction. In order to influence the results of the measured ice samples, the amount of gas left behind has to be large enough to influence the measurement, and it has to be fractionated relative to the gases that were collected during the ice extraction.

After the extraction, we froze a standard air sample on top of the collected gas and then followed the usual splitting and measurement protocol. This test was conducted twice, and in both cases, the measured standard plus residual gas samples were indistinguishable from the other standard air measurements. This suggests that even if there was any fractionation between the extracted ice sample and the gases remaining in solution, the extraction was close enough to 100% efficiency that the measurement was unaffected. It seems likely that the small amount of gas that

was present at the start of the extraction may have been degassed CO_2, which is known to remain partly in solution during our normal extractions due to its very high solubility. In summary, we can reject the hypothesis that incomplete sample degassing explains the observed systematic error.

An additional possibility is that there is co-trapping of gases along with water vapor in the water trap that is employed to remove water vapor before the air sample is collected in the sample tube (Headly & Severinghaus, 2007). As with the previous hypothesis, this would only influence the results if co-trapping fractionates the gases. Headly & Severinghaus (2007) tested if co-trapping influenced the MOT results in this pioneering study. While it was shown that a small fraction (~0.005%) of the gases in the ice sample were trapped in the water vapor trap, the remaining gases did not appear to be fractionated, so this had no influence on the results of the study. However, the analytical imprecision of the inert gas ratio measurements at this time was larger than the observed systematic difference between corrected firn air and surface ice samples found in this study. In addition, krypton isotope measurements were not made during this time, so we do not know whether they are fractionated by co-trapping.

While it is possible that differences between corrected firn air and surface ice results may be due to co-trapping of gases by water vapor in the water trap during ice sample extraction, this hypothesis cannot explain the systematic difference in results we find for surface ice samples from different sites and thus cannot explain all observed biases. Even so, we suggest that the test detailed in Headly & Severinghaus (2007) be redone to confirm that the observed difference in atmospheric proxy bias in the firn and ice is not the result of a lab artifact.

3.4.2. Gas Loss in Ice Samples

There are several additional sources of information that may provide clues about the observed systematic error in the surface ice atmospheric proxies. Considering our ‘best correction’

(PB-gt) we examine the solutions of the least-squares system for diffusive column height and firn thermal gradient to see if they are in line with our expectations based on site properties. We may also look at the isotope residuals in the least squares system to see if there are systematic offsets that may give insight into the sources of systematic error for the atmospheric proxies.

Comparing our results for diffusive column height to firn column height modelled from temperature and accumulation (Herron & Langway, 1980), the results are in line with expectations (Figure 6). Because the presence of a convective or lock-in zone will tend to reduce gravitational fractionation (Buizert et al., 2012), the diffusive column height that we solve for in our least squares system will tend to underestimate the total firn column height. As such, we may consider the modelled firn column height as an upper bound for the diffusive column height. The worst agreement between modelled and least squares firn height is found for the Law Dome DE08 site. This is understood to be the consequence of an exceptionally high accumulation rate that prevents the air from reaching gravitational equilibrium (Buizert & Severinghaus, 2016), so this disagreement is not unexpected.

The solutions for firn thermal gradients from the PB-gt correction are slightly more positive than expected at several sites including South Pole, where a negative (geothermal) temperature gradient has been directly measured (Price et al., 2002), but the PB-gt method indicates no gradient. One plausible explanation for this observation is seasonal thermal rectification (Severinghaus et al., 2001). If convection strength is constant over the year, the expression of the summer and winter seasonal temperature gradient in the gases within the firn will cancel, and show no thermal fractionation below the top 20 m. However, during the winter, enhanced convection may occur in the upper layers of the firn due to surface cracking from thermal contraction. With an enhanced convective zone in the winter months, gases in the upper firn are more turbulently

mixed, making the winter thermal signal in the gases less pronounced than the summer signal. This may result in a summertime, positive-biased thermal gradient in the measured gases that does not reflect the true thermal signal. Positive thermal gradients are also shown in the PB-gt outputs for the firn data, which lends support to this hypothesis. However, the firn air results could also be due to the recent Antarctic (Steig et al., 2009) and Greenland (Box et al., 2009) surface warming.

The mass-normalized isotope residuals for the PB-gt correction show a general trend that is consistent for all sites, with positive residuals in argon isotopes and negative residuals in nitrogen and krypton isotopes that are similar in magnitude (Figure 6). The positive residuals in argon isotopes may indicate that they are influenced by artifactual gas loss, which will enrich their values above the original gas composition of the ice (Severinghaus et al., 2003). This hypothesis is consistent with the observation that the ISO-^{40}Ar corrections lead to a negative atmospheric proxy bias for most sites/samples (Figure 4). However, this process would only influence results for the correction methods that include argon isotopes (Table 1), so cannot explain all of our observations.

Still, we can make several predictions to test whether the observed systematic error is, in part, caused by artifactual argon isotope enrichment due to gas loss. First, we predict that if argon isotopes measured in the ice samples are influenced by gas loss, including a gas loss correction should reduce the disagreement between the firn and surface ice results, because the firn results are not influenced by artifactual gas loss. Second, we expect that ice samples that have experienced more artifactual gas loss will tend to give more negative results for the atmospheric proxies than those that have experienced less.

In order to test these predictions, we must make a quantitative estimate of the magnitude of gas loss for each sample, and its influence on the argon isotopes. Of the measured gases in this study, gravitationally corrected $\delta O_2/N_2$, $\delta Ar/N_2$, and $\delta^{18}O\text{-}O_2$ have all demonstrated alteration due

to gas loss (Bender et al., 1995), which cause negative excursions in gravitationally corrected $\delta O_2/N_2$ and $\delta Ar/N_2$, and positive excursions in $\delta^{18}O\text{-}O_2$:

$$\delta O_2/N_{2gravcorr} = \delta O_2/N_{2\,meas} - 4 \times \delta^{15}N_{meas}$$

$$\delta Ar/N_{2gravcorr} = \delta Ar/N_{2\,meas} - 12 \times \delta^{15}N_{meas}$$

$$\delta^{18}O_{gravcorr} = \delta^{18}O_{meas} - 2 \times \delta^{15}N_{meas}$$

Changes in $\delta^{18}O\text{-}O_2$ on millennial timescales due to changes in $\delta^{18}O_{sw}$ and in the Dole Effect (Severinghaus et al., 2009) preclude its use in assessing gas loss in paleo-MOT studies. However, because these are modern ice samples, and $\delta^{18}O\text{-}O_2$ has not changed significantly in the past millennium, we may consider the $\delta^{18}O\text{-}O_2$ as a metric for gas loss.

One complication in using gravitationally corrected $\delta O_2/N_2$, $\delta Ar/N_2$, and $\delta^{18}O\text{-}O_2$ to quantify $\delta^{40}Ar$ (and $\delta^{38}Ar$) enrichment is the fact that these gases are influenced by both natural (i.e. bubble close off) and artifactual gas loss (Battle et al., 2011; Severinghaus & Battle, 2006), so their application in prescribing artifactual $\delta^{40}Ar$ enrichment is somewhat tenuous. To correct $\delta^{40}Ar$ and $\delta^{38}Ar$ for gas loss, we quantify the influence of gas loss on $\delta^{40}Ar$ detailed in Buizert et al (in prep), and assume that the gas loss fractionation of $\delta^{40}Ar$ is twice that of $\delta^{38}Ar$:

$$\Delta^{40}_{GL} = -\frac{\epsilon^{40}}{\left(\delta O_2/N_{2gravcorr} - \delta Ar/N_{2gravcorr}\right)}$$

$$\Delta^{38}_{GL} = -\frac{\epsilon^{40}/_2}{\left(\delta O_2/N_{2gravcorr} - \delta Ar/N_{2gravcorr}\right)}$$

Where Δ^{40}_{GL} and Δ^{38}_{GL} represent the fractionation of $\delta^{40}Ar$ and $\delta^{38}Ar$ due to gas loss respectively. We use the ϵ^{40} value from Buizert et al (in prep) of -0.008 to correct $\delta^{40}Ar$ and $\delta^{38}Ar$ and then apply these corrected argon isotope values to the firn fractionation corrections. We

compare the results in atmospheric proxies from the surface ice to the firn air samples using a two sample Student t-test, as we did in the previous section. For five of the six methods that use argon isotope data to correct the inert gas ratios, we find that the disagreement between firn and surface ice results increases when a gas loss correction is included. Testing a range of ϵ^{40} values does not considerably affect the results. This observation would suggest that artifactual enrichment of argon isotopes in surface ice samples cannot explain the difference between firn and surface ice systematic bias in atmospheric proxies.

Using $\delta O_2/N_2$, $\delta Ar/N_2$, and $\delta^{18}O\text{-}O_2$ as metrics for gas loss, we can test the second prediction, that surface ice samples that have experienced more gas loss will give more negative values for the MOT proxies (Figure 7). Interestingly, we find that there is a statistically significant negative correlation between the atmospheric proxies and $\delta O_2/N_2$ and $\delta Ar/N_2$. However, we expect the correlation between the systematic error in the atmospheric proxies and $\delta O_2/N_2$ (or $\delta Ar/N_2$) to be positive if it was a result of argon isotope enrichment due to gas loss because an enrichment of argon isotopes due to gas loss (which should cause negative excursions in $\delta O_2/N_2$ and $\delta Ar/N_2$) would result in an overestimation and overcorrection of the inert gas ratios for gravitational fractionation, and thus impart a negative bias on the atmospheric proxies.

This negative correlation is consistent to what is observed for the atmospheric proxies in clathrate ice samples when they have experienced extreme artifactual gas loss (e.g. -200‰ $\delta O_2/N_2$ in the deep Byrd core exposed to glycol and depressurization; Severinghaus, personal communication). The negative correlation has been hypothesized to be due to the fact that the clathrate dissociation pressures of Xe and Kr are much lower than that of N_2, so N_2 is preferentially lost from clathrates relative to Xe and Kr under these extreme conditions. Severinghaus & Battle, 2006 suggested that the inert gas ratios are not fractionated by natural gas loss due to bubble

closeoff, and fractionation due to artifactual gas loss, thus far, has only been observed in the inert gas ratios in clathrate ice. However, it is possible that the effect in bubbly ice is very small and has been unobserved up to this point. This hypothesis would also explain why a site-dependent bias can be seen for all correction methods and may explain the difference observed between the firn and surface ice samples.

We note that the hypothesis that the observed bias in the atmospheric proxies is due to artifactual gas loss relatively tenuous and the analysis of additional ice cores that have experienced significant gas loss may disprove its validity. In fact, if we include surface ice samples from the EDC MOT study (Baggenstos et al., 2019), we find that it does not follow the trend observed for the sites included in this study. Another caveat to this hypothesis is that we do not necessarily expect the scaling between the gas loss experienced by the inert gas ratios and gas loss predictors to be the same for differing mechanisms of gas loss (Bender et al., 1995; Kobashi et al., 2008). Future investigations into the different mechanisms of artifactual gas loss and its influence on $\delta^{40}Ar$ and the inert gas proxies may help determine whether gas loss contributes to systematic error in MOT reconstructions.

3.4.3. Mischaracterization of Kinetic Fractionation

Another piece of evidence that can be used to understand the difference between the firn air and surface ice results is the comparison of results of the individual correction methods. Some of the largest differences between the firn and surface ice results are observed for corrections that include a term for kinetic fractionation (PB-gk and PB-gtk). While these corrections performed best for the firn air samples in minimizing systematic error, in the case of surface ice, they introduced a positive systematic error in the atmospheric proxies for most sites. In fact, the PB-gtk

correction performed markedly worse than any of the other methods in its application to surface ice samples.

Modelling studies on kinetic fractionation in the firn and its influence on isotopes of inert gases (Birner et al., 2018; Buizert et al., in prep.; Buizert & Severinghaus, 2016; Kawamura et al., 2013) have found that while firn models are able to simulate the observed firn air difference between krypton and argon isotopes ($^{86}Kr_{exc}$), they underestimate the observed ice sample magnitude of $^{86}Kr_{exc}$.

This may provide some indication that the firn air samples are not representative of the gases occluded in the ice. Buizert & Severinghaus (2016) proposed a mechanism for kinetic fractionation through dispersion, where gases become unmixed by traversing different highly tortuous and disordered pathways in the firn. It is possible that the firn air collection method preferentially samples firn pathways with the lowest tortuosity and highest conductivity, where bulk flow is less restricted, and where we expect the least dispersive fractionation to occur. If this is the case, the larger magnitude of $^{86}Kr_{exc}$ observed in ice compared to firn may be due to a sampling bias during firn air collection. This may influence our current understanding of kinetic fractionation, and the effect of kinetic fractionation on the isotopes and inert gas ratios.

3.4.4. Adsorption

A final hypothesis that may explain the observed systematic error in the firn and surface ice atmospheric proxies is that certain gases may adsorb onto snow/firn surfaces. Because of their relatively high polarizability, Xe and Kr have the potential to adsorb onto snow/ice surfaces more strongly than N_2. To our knowledge, there have been no studies that have observed natural adsorption of Xe or Kr onto snow or ice. While Kr has been used to calculate the specific surface area of snow surfaces by adsorption experiments (Hachikubo et al., 2013), these experiments are

conducted at temperatures far below those experienced by polar regions, and at high Kr pressures. This induces multilayer adsorption, which is not likely to occur naturally for these atmospheric gases. However, studies on the influence of adsorption of CO_2 on ice surfaces have shown enrichment of CO_2 in the top ~10 m of firn due to adsorption, but that the recrystallization during firnification greatly reduces the surface area of the firn and thus the quantity of adsorbed gas is insignificant in the deepest layers of the firn, where bubble close off occurs (Stauffer & Tschumi, 2000).

If Xe and Kr are adsorbed onto snow/firn surfaces, we would expect adsorption to have a greater influence on colder sites. Because adsorption of gases is highly temperature dependent, colder sites would experience more adsorption of Xe and Kr than warmer ones. This would cause atmospheric proxies to be more positively biased at colder sites. This is broadly consistent with our observations of site dependent bias (Figure 8), except for Siple Dome.

In addition, adsorption may help to explain the difference between the atmospheric proxies in the firn air and surface ice. We expect that adsorbed Xe and Kr would not desorb during firn air collection, and thus the surface ice samples would have a more positive bias in the atmospheric proxies compared to the firn. This is generally consistent with the observed offsets between the firn and sample ice results (Figure 5).

Firn adsorption tests have been conducted to test its potential influence on $\delta^{15}N\text{-}N_2$ in ice (Grachev & Severinghaus, 2003). A similar test may help determine if adsorption introduces systematic error in MOT reconstructions.

3.5. Conclusions

We observe differences between firn air and surface ice samples in the systematic error of atmospheric proxies, suggesting that additional processes may influence ice samples that are

currently unaccounted-for in our fractionation corrections. The systematic error in surface ice samples is significantly correlated between atmospheric proxies, making it hard to distinguish from a true atmospheric signal. At this time, we do not have a decisive explanation for the observed systematic error in the surface ice samples but have suggested several tests that may help to prove or disprove some of the proposed hypotheses included in this chapter.

In order to minimize the influence of systematic error in future MOT studies, we make several recommendations. We find that the error in atmospheric proxies from the PB-gt correction only slightly exceeds that which is expected from analytical uncertainty (±0.4°C vs ±0.3°C) and therefore suggest that this correction is used for future MOT studies. However, this method appears to introduce site-dependent bias in the atmospheric proxies. For this reason, we suggest that surface ice samples should be analyzed for a given ice core in order to serve as a point of validation or calibration to minimize systematic error.

Appendex 3.A: Quantifying Analytical Error for MOT proxies

In order to compare the error observed in the results of the firn air and surface ice atmospheric proxies to what we may expect from analytical error, we create 'synthetic' isotope and inert gas ratio data, which is representative of the fractionation expected for a diffusive column height of 65m and no thermal or kinetic fractionation. We apply this condition (instead of zeros for all inputs) because we do not allow our least-squares gravitational fractionation term to be negative. We also tested synthetic data in which thermal and/or kinetic fractionation was also included, but this had no appreciable effect on the calculated analytical noise or the correlation between the error in atmospheric proxies. In order to estimate analytical error and the expected correlation between analytical error in the atmospheric proxies, we run Monte Carlo simulations

of the data that incorporate measurement uncertainties of the isotopes and inert gas ratios and assess each correction method. We can then compare the results of the corrected 'synthetic' data, representative of the expected analytical noise to the results of our corrected firn air and surface ice samples to determine if the observed error can be explained by analytical uncertainty alone, or if there is additional systematic error for the atmospheric proxies.

Appendex 3.B: Dome Fuji Firn Air Samples

Firn air samples from Dome Fuji were collected in 1998 and analyzed in 2009 at SIO by Kenji Kawamura. Samples were collected in metal flasks at ~10 bar. The observed offset in the surface air flask from the modern air standard may have been the result of (1) fractionation during firn air sampling due to a leak around the pump head during or a strong pressure gradient around the firn air inlet (2) leak through the 4H valves in the sample flasks during storage, or (3) fractionation during subsampling of aliquots for other measurements (greenhouse gases and their isotopes) before analysis of inert gases (Kawamura, personal communication). This fractionation appears to be present for all sample flasks.

Appendex 3.C: NEEM Firn Air Samples

Firn air samples from the NEEM ice core site were collected in 2008 and analyzed in 2009 at SIO by Kenji Kawamura. Firn air samples were collected in 2.5-liter glass flasks at ~1 bar. Samples showed no indication of fractionation during firn air sampling.

Appendex 3.D: GISP2 Firn Air Samples

Firn air samples from Summit (the GISP2 coring site) were collected in 2013 and analyzed in 2016 at SIO. Firn air samples were collected in 35 liter metal flasks at ~2 bar and analyzed according to the method of Kawamura et al, (2013).

Appendex 3.E: SP15 Firn Air Samples

Firn air samples from South Pole were collected in 2015 and analyzed in 2017 at SIO. Firn air samples were collected in 2.5-liter glass flasks at ~1 bar. Firn air sampling was terminated at ~94 m depth because of complications in the field, so no samples in the lock-in-zone were collected.

Acknowledgements

Chapter 3 contains unpublished material with the following co-authors: Christo Buizert, Kenji Kawamura, Daniel Baggenstos, and Jeffrey Severinghaus. I was the primary investigator and author of this work.

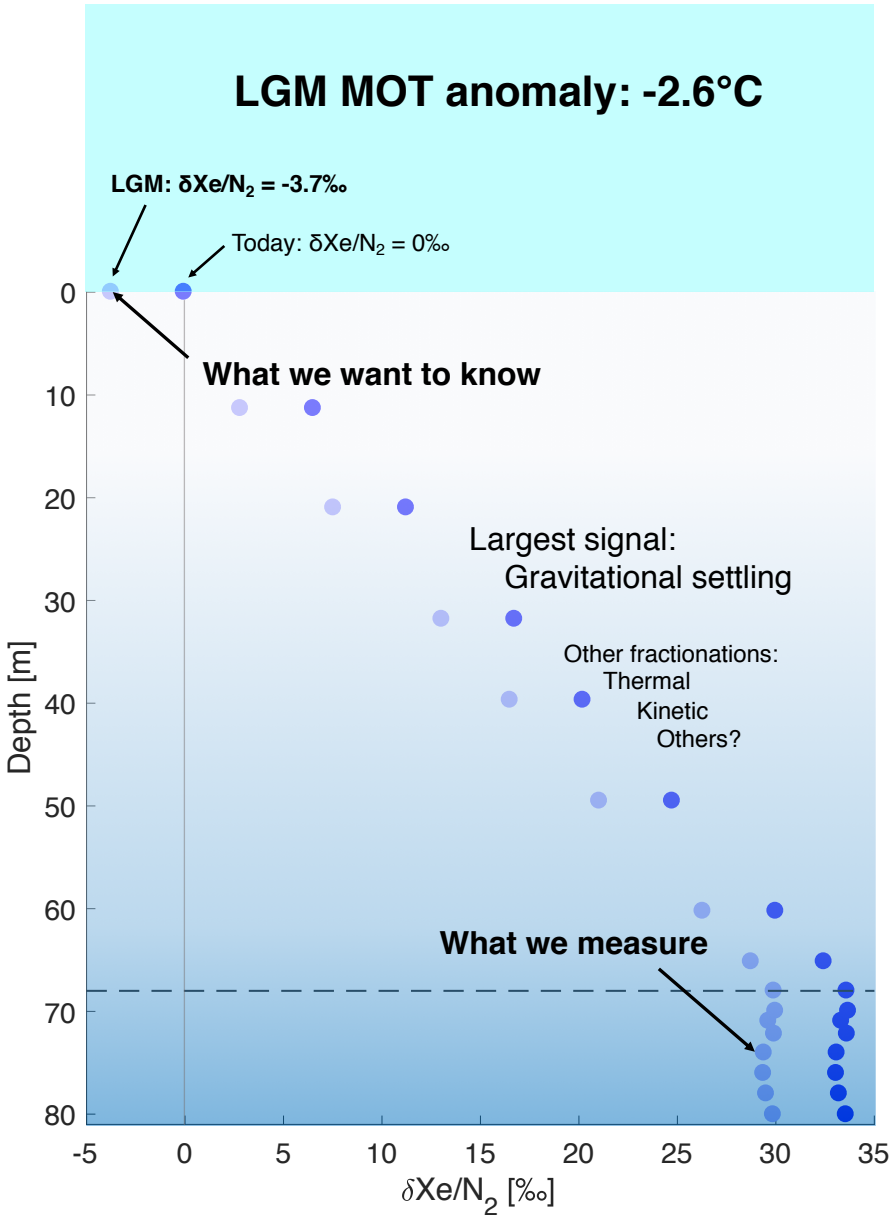

Figure 3.1: Schematic comparison of LGM MOT signal to firn air fractionations. Dark blue circles show modern measured $\delta Xe/N_2$ in firn air from Summit, Greenland. Lighter blue circles show what the $\delta Xe/N_2$ signal would look like if MOT was 2.6°C colder than today (as in the LGM), with the same firn fractionations. Dashed horizontal line indicates the close off depth, where gravitational settling ceases. The observed firn fractionations at Summit (mostly gravitational) are about an order of magnitude larger than the total atmospheric change in $\delta Xe/N_2$ due to MOT change from the LGM to present.

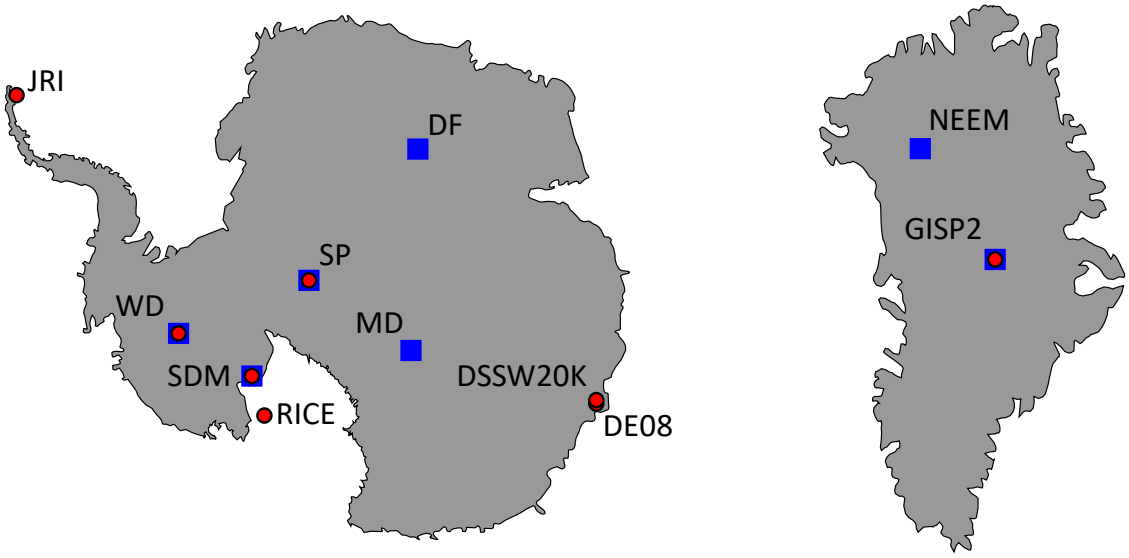

Figure 3.2: Locations of firn and near-surface ice samples analyzed in this study. Blue squares indicate the location of firn air samples, red circles indicate the location of surface ice samples.

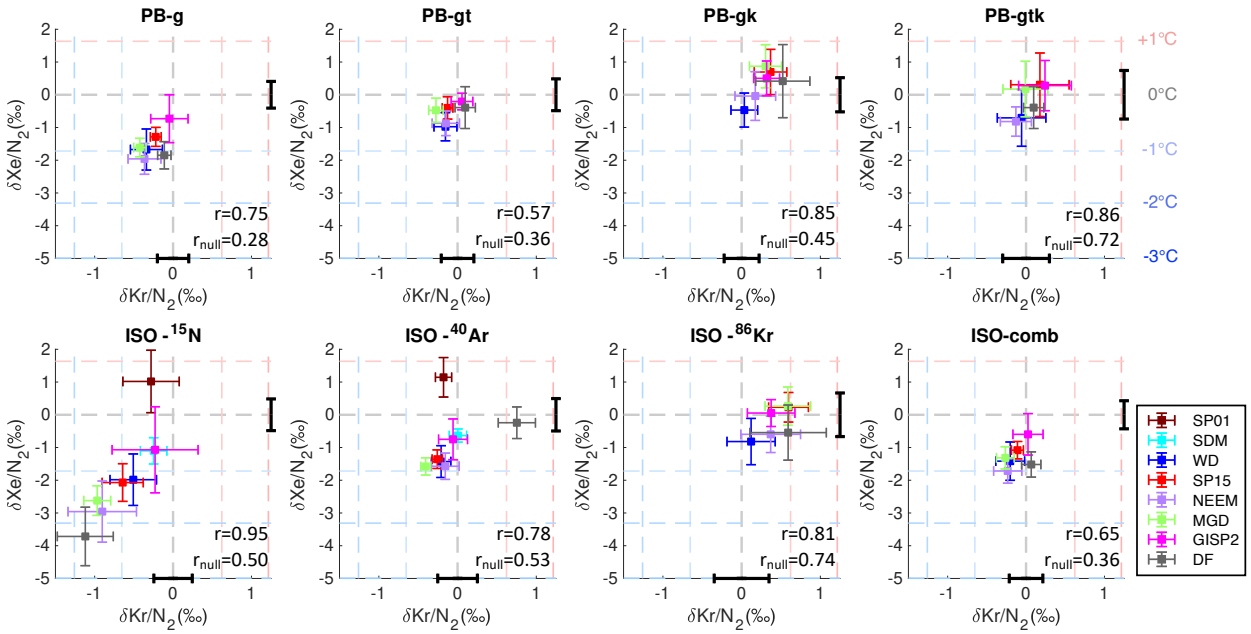

Figure 3.3: Apparent error in corrected $\delta Xe/N_2$ and $\delta Kr/N_2$ of firn air for the various correction methods. Points show site mean and error bars show spread (1σ) in the results for all the samples at a given site. Black error bars show the expected analytical uncertainty in $\delta Xe/N_2$ and $\delta Kr/N_2$ for each correction method. Grid lines are spaced by 1°C MOT bias, where the grey lines show no bias, the red show a positive bias, and the blue lines show a negative bias. Pearson correlation coefficients are shown for $\delta Xe/N_2$ and $\delta Kr/N_2$ for all samples (not site averages) and compared to the correlation coefficient (r_{null}) expected due to analytical noise for each correction method. Note that the results for firn air measurements from (Severinghaus & Battle, 2006) are not included in calculating the correlations, and only shown for the isotope ^{40}Ar and ^{15}N corrections.

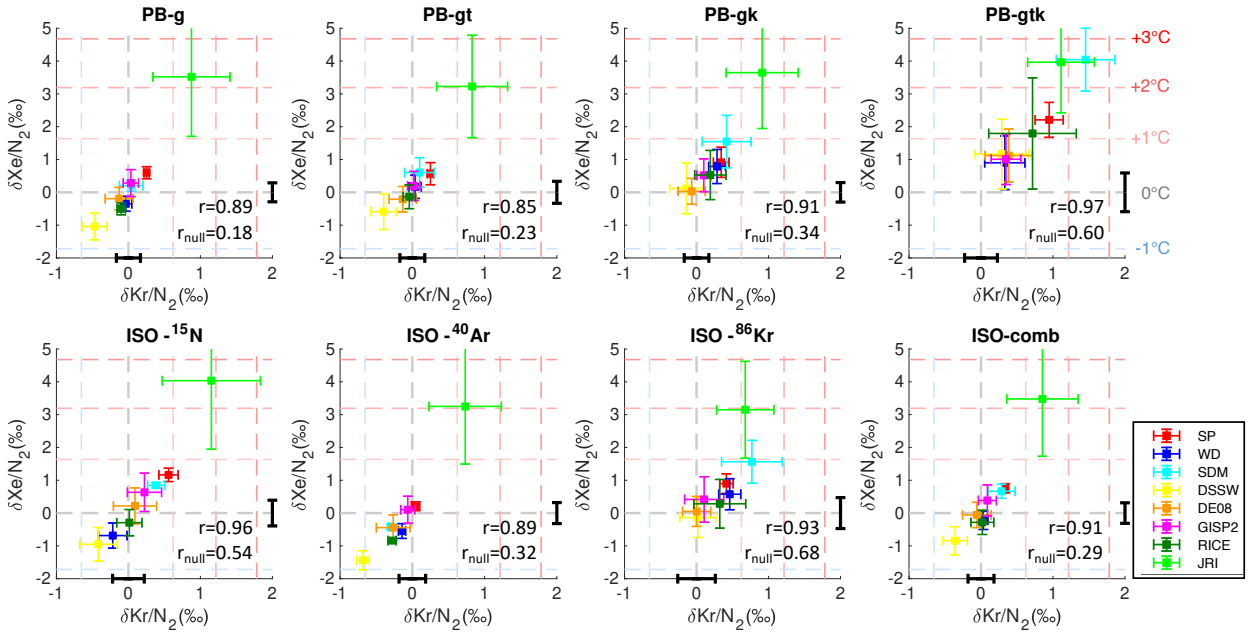

Figure 3.4: Apparent error in corrected $\delta Xe/N_2$ and $\delta Kr/N_2$ of surface ice for the various correction methods. Points show site mean and error bars show spread (1σ) in the samples for each site. Black error bars show the expected analytical uncertainty in $\delta Xe/N_2$ and $\delta Kr/N_2$ for each correction method. Grid lines are spaced by 1°C MOT bias, where the grey lines show no bias, the red show a positive bias, and the blue lines show a negative bias. Pearson correlation coefficients are shown for $\delta Xe/N_2$ and $\delta Kr/N_2$ for all samples (not site averages) and compared to the correlation coefficient (r_{null}) expected due to analytical noise for each correction method. The JRI site was not included in calculating the correlation coefficients because it is influenced by surface melt.

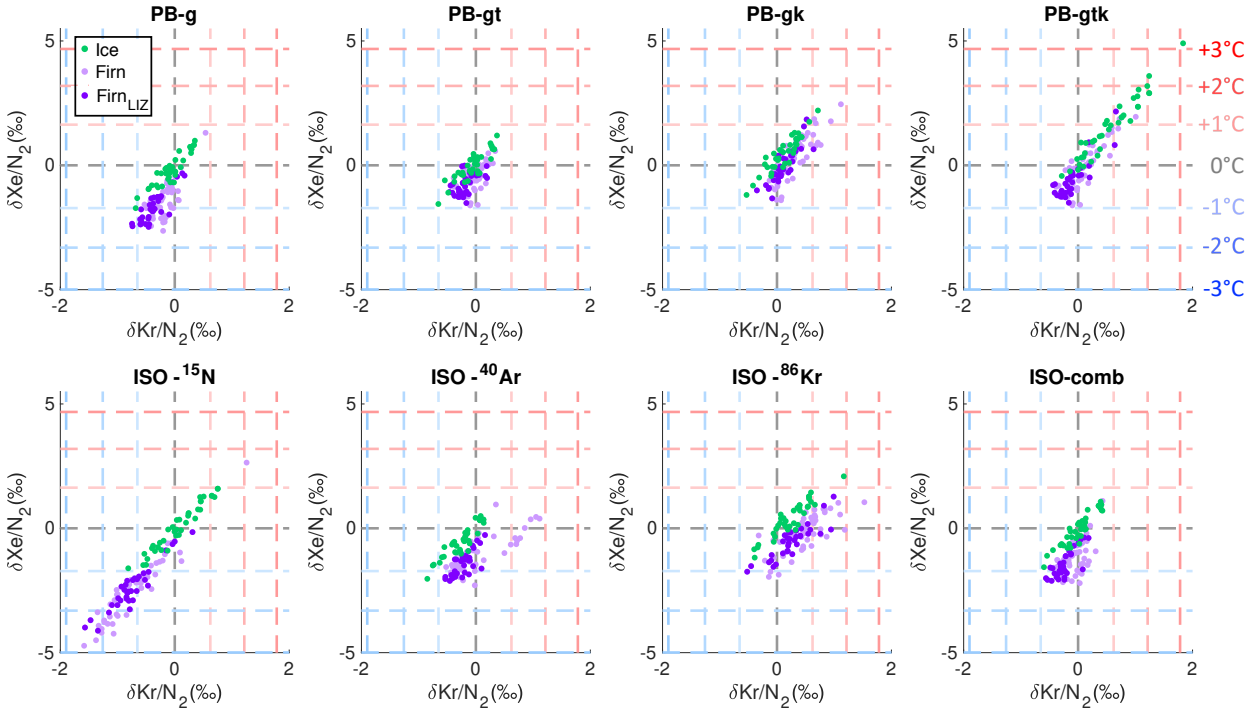

Figure 3.5: Comparison of error for firn versus surface ice samples (excluding firn air samples from Severinghaus & Battle, 2006 and surface ice samples from JRI). Green points show surface ice samples, dark purple points show firn air samples within the lock in zone, and light purple points show firn air samples above the lock in zone (but below 20m). Grid lines are spaced by 1°C bias, where the grey lines show no bias, the red show a positive MOT bias, and the blue lines show a negative MOT bias.

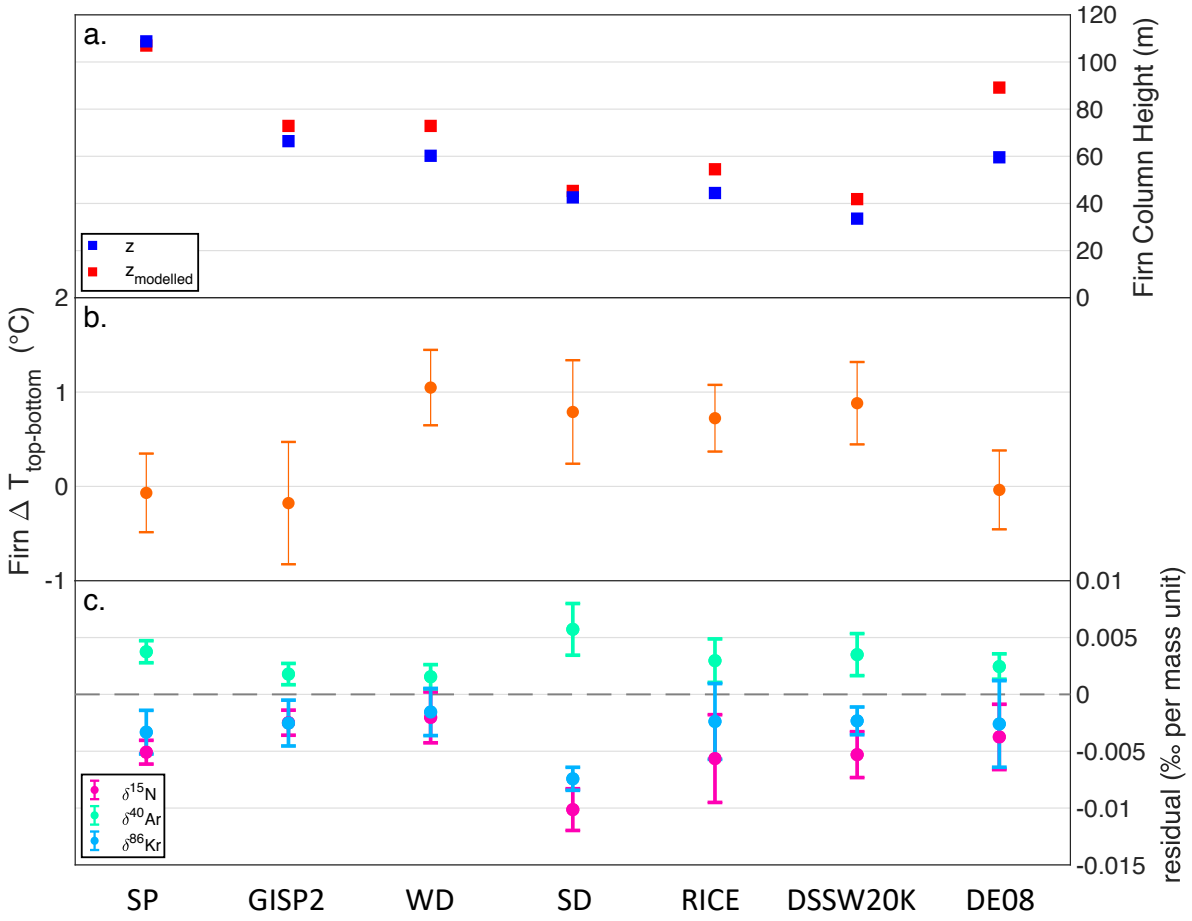

Figure 3.6: Output from the PB-gt method at each surface ice site. a) Average diffusive column height solution for each site (blue) compared to the modelled firn column height (red). b) Solution for firn thermal gradient (top-bottom) for each site. c) Isotope residuals for the least squares correction method. Error bars in b) and c) show the 1σ spread in solutions for samples at each site.

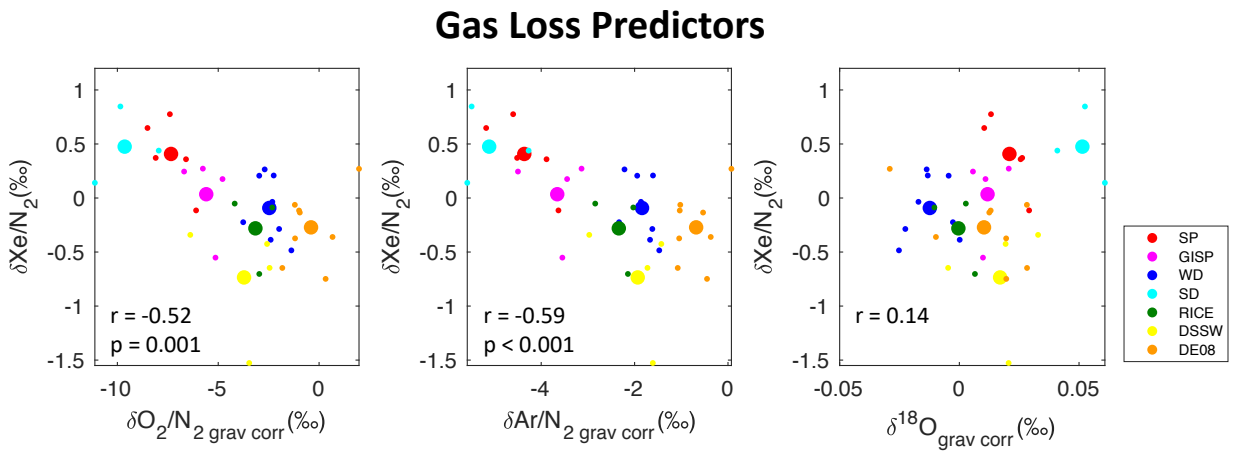

Figure 3.7: Predictors of gas loss versus empirically corrected δXeN_2. Large points show the mean value for each site, and smaller points indicate individual sample measurements. Pearson correlation coefficients and p-values are shown for individual samples (not site means).

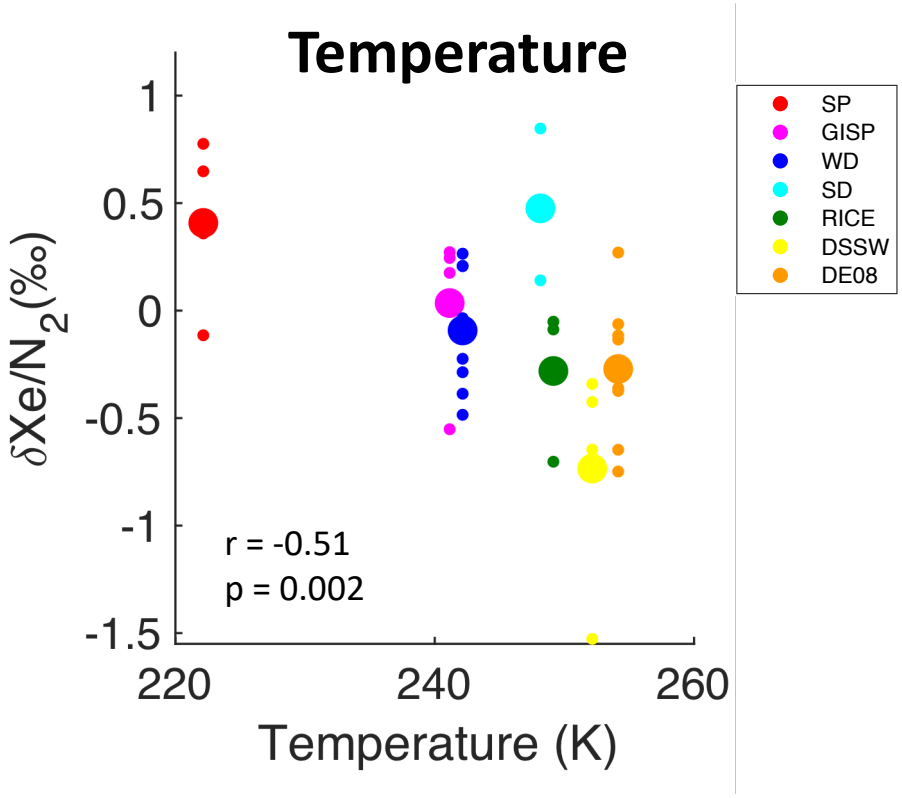

Figure 3.8: Temperature versus empirically corrected δXeN_2. Large points show the mean value for each site, and smaller points indicate individual sample measurements. Pearson correlation coefficient and p-value shown for individual samples (not site means).

Table 3.1: Methods of fractionation corrections considered in this study. Checkmarks indicate the types of fractionations included in each correction method, and the isotopes included for each method to correct the inert gas ratios. The ISO-comb correction takes the average of the three mass-normalized isotope ratios indicated by checkmarks.

Methods of Fractionation Corrections

METHOD	**FRACTIONATION**			**ISOTOPES**					
	Gravitational	Thermal	Kinetic	$\delta^{15}N$	$\delta^{40}Ar$	$\delta^{38}Ar$	$\delta^{86}Kr$	$\delta^{83}Kr$	$\delta^{84}Kr$
Process based									
PB-g	✓			✓	✓	✓	✓	✓	✓
PB-gt	✓	✓		✓	✓	✓	✓	✓	✓
PB-gk	✓		✓	✓	✓	✓	✓	✓	✓
PB-gtk	✓	✓	✓	✓	✓	✓	✓	✓	✓
Isotope based									
ISO-^{15}N				✓					
ISO-^{40}Ar					✓				
ISO-^{86}Kr							✓		
ISO-comb				✓	✓		✓		

Table 3.2: Firn air samples included in this study with site temperatures and accumulation rates. Column four indicates the number of firn air samples collected below 20 meters depth (including within the lock in zone). Column five indicates the number of samples within the lock in zone.

Firn Air Samples

Site	T (°C)	A (m ice yr^{-1})	N>20m	N_{LIZ}	Source
SDM [1]	-25	0.13	5	5	Severinghaus & Battle, 2006
SP01 [1, 2]	-51	0.08	19	8	Severinghaus & Battle, 2006
WD	-30	0.22	19	9	Orsi, 2013
MD	-49	0	13	5	Kawamura et al., 2013
GISP2	-31	0.23	14	8	This study
SP15 [2]	-51	0.08	6	0	This study
NEEM	-29	0.22	18	11	This study
DF [3]	-57	0.03	11	0	This study

[1] Sites not included in assessment of fractionation corrections that include krypton isotopes

[2] Samples from South Pole collected in 2001 (SP01) and 2015 (SP15)

[3] Surface air flask showed evidence of fractionation during collection that may have influenced all samples, see appendix

Table 3.3: Surface ice samples included in this study with site temperatures and accumulation rates. All data are from Buizert et al., (in prep).

Surface Ice Samples

Site	T (°C)	A (m ice yr^{-1})	N
SP	-51	0.08	5
GISP2	-31	0.23	4
WD	-32	0.22	8 [1]
SDM	-25	0.13	3 [1]
RICE	-23	0.24	3 [1]
DSSW20K	-21	0.16	4
DE08	-19	1.2	8
JRI	-14	0.68	5

[1] Does not include sample that was lost or rejected due to technical problems

References

Baggenstos, D. (2015). *Taylor Glacier as an archive of ancient ice for large-volume samples: Chronology, gases, dust, and climate*. University of California, San Diego.

Baggenstos, D., Häberli, M., Schmitt, J., Shackleton, S. A., Birner, B., Severinghaus, J. P., Kellerhals, T., & Fischer, H. (2019). The Earth's radiative imbalance from the Last Glacial Maximum to the present. *Proceedings of the National Academy of Sciences*, *116*(30), 14881–14886. https://doi.org/10.1073/pnas.1905447116

Battle, Mark O, Bender, M. L., Sowers, T., Tans, P., Butler, J. H., Elkins, J. W., Ellis, J. T., Conway, T., Zhang, N., Lang, P., & Clarke, A. D. (1996). Atmospheric gas concentrations over the past century measured in air from firn at the South Pole. *Nature*, *383*. https://doi.org/https://doi.org/10.1038/383231a0

Battle, M O, Severinghaus, J. P., Sofen, E. D., Plotkin, D., Orsi, A. J., Aydin, M., Montzka, S. A., & Sowers, T. (2011). Controls on the movement and composition of firn air at the West Antarctic Ice Sheet Divide. *Atmospheric Chemistry and Physics*, *11*, 11007–11021. https://doi.org/10.5194/acp-11-11007-2011

Bender, M. L., Sowers, T., & Lipenkov, V. (1995). On the concentrations of O2, N2, and Ar in trapped gases from ice cores. *Journal of Geophysical Research*, *100*, 18651–18660. https://doi.org/10.1029/94jd02212

Bereiter, B., Shackleton, S., Baggenstos, D., Kawamura, K., & Severinghaus, J. (2018). Mean global ocean temperatures during the last glacial transition. *Nature*, *553*(7686), 39–44. https://doi.org/10.1038/nature25152

Bereiter, B., Kawamura, K., & Severinghaus, J. P. (2018). New methods for measuring atmospheric heavy noble gas isotope and elemental ratios in ice core samples. *Rapid Communications in Mass Spectrometry*, *32*(10), 801–814. https://doi.org/10.1002/rcm.8099

Birner, B., Buizert, C., Wagner, T. J. W., & Severinghaus, J. P. (2018). The influence of layering and barometric pumping on firn air transport in a 2D model. *The Cryosphere*, *12*, 2021–2037. https://doi.org//10.5194/tc-12-2021-2018

Box, J. E., Yang, L., Bromwich, D. H., & Bai, L.-S. (2009). Greenland Ice Sheet Surface Air Temperature Variability : 1840 – 2007 *. *American Meteorological Society*, *22*, 4029–4049. https://doi.org/10.1175/2009JCLI2816.1

Buizert, C., & Severinghaus, J. P. (2016). Dispersion in deep polar firn driven by synoptic-scale surface pressure variability. *The Cryosphere*, *10*, 2099–2111. https://doi.org/10.5194/tc-10-2099-2016

Buizert, C., Shackleton, S., Severinghaus, J. P., Bereiter, B., Roberts, W. H. G., Kawamura, K.,

Baggenstos, D., Orsi, A. J., Oyabu, I., Birner, B., Brook, E. J., Etheridge, D. M., Bertler, N., Pyne, R. L., Mulvaney, R., & Mosley-Thompson, E. (n.d.). The new Kr-86 excess ice core proxy for synoptic activity: West Antarctic storminess possibly linked to ITCZ movement through the last deglaciation. *Climate of the Past*.

Buizert, C., Martinerie, P., Petrenko, V. V, Severinghaus, J. P., Trudinger, C. M., Witrant, E., Rosen, J. L., Orsi, A. J., Rubino, M., Etheridge, D. M., Steele L P, Hogan, C., Laube, J. C., Sturges, W. T., Levchenko, V. A., Smith, A. M., Levin, I., Conway, T. J., Dlugokencky, E. J., et al. (2012). Gas transport in firn : multiple-tracer characterisation and model intercomparison for NEEM , Northern Greenland. *Atmospheric Chemistry and Physics*, *12*, 4259–4277. https://doi.org/10.5194/acp-12-4259-2012

Craig, H., Horibe, Y., & T., S. (1988). Gravitational Seperation of Gases and Isotopes in Polar Ice Caps. *Science*, *242*(4886), 1675–1678. https://doi.org/10.1126/science.242.4886.1675

Gebbie, G., & Huybers, P. (2019). The Little Ice Age and 20th-century deep Pacific cooling. *Science*, *363*(6422), 70–74. https://doi.org/10.1126/science.aar8413

Govin, A., Capron, E., Tzedakis, P. C., Verheyden, S., Ghaleb, B., Hillaire-marcel, C., St-onge, G., Stoner, J. S., Bassinot, F., Bazin, L., Blunier, T., Landais, A., Martrat, B., Masson-delmotte, V., Parrenin, F., & Seidenkrantz, M. (2015). Sequence of events from the onset to the demise of the Last Interglacial : Evaluating strengths and limitations of chronologies used in climatic archives. *Quaternary Science Reviews*, *129*, 1–36. https://doi.org/10.1016/j.quascirev.2015.09.018

Grachev, A., & Severinghaus, J. P. (2003). Laboratory determination of thermal diffusion constants for 29N2/28N2 in air at temperatures from -60 to 0° C for reconstruction of magnitudes of abrupt climate changes using the ice core fossil – air paleothermometer. *Geochimica et Cosmochimica Acta*, *67*(3), 345–360. https://doi.org/10.1016/S0016-7037(02)01115-8

Hachikubo, A., Yamaguchi, S., Arakawa, H., Tanikawa, T., Hori, M., Sugiura, K., Niwano, M., Kuchiki, K., & Aoki, T. (2013). Investigation of adsorbent for a measurement of snow specific surface area by the gas adsorption method. In *International Snow Science Workshop* (pp. 73–77). Grenoble.

Hamme, R. C., & Severinghaus, J. P. (2007). Trace gas disequilibria during deep-water formation. *Deep Sea Research*, *54*, 939–950. https://doi.org/10.1016/j.dsr.2007.03.008

Headly, M. A., & Severinghaus, J. P. (2007). A method to measure Kr/N2 ratios in air bubbles trapped in ice cores and its application in reconstructing past mean ocean temperature. *Journal of Geophysical Research*, *112*(19), 1–12. https://doi.org/10.1029/2006JD008317

Herron, M. M., & Langway, C. C. (1980). Firn densification: an empirical model. *Journal of Glaciology*, *25*(93). https://doi.org/https://doi.org/10.3189/S0022143000015239

Ikeda-Fukazawa, T., Fukumizu, K., Kawamura, K., Aoki, S., Nakazawa, T., & Hondoh, T. (2005).

Effects of molecular diffusion on trapped gas composition in polar ice cores. *Earth and Planetary Science Letters*, *229*, 183–192. https://doi.org/10.1016/j.epsl.2004.11.011

Kawamura, K., Severinghaus, J. P., Albert, M. R., Courville, Z. R., Fahnestock, M. A., Scambos, T., Shields, E., & Shuman, C. A. (2013). Kinetic fractionation of gases by deep air convection in polar firn. *Atmospheric Chemistry and Physics*, *13*, 1–14. https://doi.org/10.5194/acp-13-1-2013

Kobashi, T., Severinghaus, J. P., & Kawamura, K. (2008). Argon and nitrogen isotopes of trapped air in the GISP2 ice core during the Holocene epoch (0 – 11 , 500 B . P .): Methodology and implications for gas loss processes. *Geochimica et Cosmochimica Acta*, *72*, 4675–4686. https://doi.org/10.1016/j.gca.2008.07.006

Orsi, A. J. (2013). *Temperature reconstruction at the West Antarctic Ice Sheet Divide, for the last millenium, from the combination of borehole temperature and inter gas isotope measurements*. University of California San Diego.

Orsi, A. J., Kawamura, K., Fegyveresi, J. M., Headly, M. A., Alley, R. B., & Severinghaus, J. P. (2015). Differentiating bubble-free layers from Melt layers in ice cores using noble gases. *Journal of Glaciology*, *61*(227), 585–594. https://doi.org/10.3189/2015JoG14J237

Price, P. B., Nagornov, O. V, Bay, R., Chirkin, D., He, Y., Miocinovic, P., Richards, A., Woschnagg, K., Koci, B., & Zagorodnov, V. (2002). Temperature profile for glacial ice at the South Pole : Implications for life in a nearby subglacial lake. *Proceedings of the National Academy of Sciences*, *99*(12), 7844–7847. https://doi.org/https://doi.org/10.1073/pnas.082238999

Rasmussen, S. O., Bigler, M., Blockley, S. P., Blunier, T., Buchardt, S. L., Clausen, H. B., Cvijanovic, I., Dahl-jensen, D., Johnsen, S. J., Fischer, H., Gkinis, V., Guillevic, M., Hoek, W. Z., Lowe, J. J., Pedro, J. B., Popp, T., Seierstad, I. K., Peder, J., Svensson, A. M., et al. (2014). A stratigraphic framework for abrupt climatic changes during the Last Glacial period based on three synchronized Greenland ice-core records : refining and extending the INTIMATE event stratigraphy. *Quaternary Science Reviews*, *106*, 14–28. https://doi.org/10.1016/j.quascirev.2014.09.007

Ritz, S. P., Stocker, T. F., & Severinghaus, J. P. (2011). Noble gases as proxies of mean ocean temperature : sensitivity studies using a climate model of reduced complexity. *Quaternary Science Reviews*, *30*(25–26), 3728–3741. https://doi.org/10.1016/j.quascirev.2011.09.021

Schwander, J., Stauffer, B., & Sigg, A. (1988). Air mixing in firn and the age of the air at pore close-off. *Annals of Glaciology*, *10*, 141–145. https://doi.org/10.1017/S0260305500004328

Severinghaus, J. P., & Battle, M. O. (2006). Fractionation of gases in polar ice during bubble close-off: New constraints from firn air Ne, Kr and Xe observations. *Earth and Planetary Science Letters*, *244*(1–2), 474–500. https://doi.org/10.1016/j.epsl.2006.01.032

Severinghaus, J. P., Sowers, T., Brook, E. J., Alley, R. B., & Bender, M. L. (1998). Timing of abrupt climate change at the end of the younger dryas interval from thermally fractionated gases in polar ice. *Nature*, *391*(6663), 141–146. https://doi.org/10.1038/34346

Severinghaus, J. P., Grachev, A., & Battle, M. (2001). Thermal fractionation of air in polar firn by seasonal temperature gradients. *Geochemistry, Geophysics, Geosystems*, *2*(7). https://doi.org/10.1029/2000GC000146

Severinghaus, J. P., Grachev, A., Luz, B., & Caillon, N. (2003). A method for precise measurement of argon 40/36 and krypton/argon ratios in trapped air in polar ice with applications to past firn thickness and abrupt climate change in Greenland and at Siple Dome , Antarctica. *Geochimica et Cosmochimica Acta*, *67*(3), 325–343. https://doi.org/https://doi.org/10.1016/S0016-7037(02)00965-1

Severinghaus, J. P., Severinghaus, J. P., Beaudette, R., & Headly, M. A. (2009). Oxygen-18 of O2 Records the Impact of Abrupt Climate Change on the Terrestrial Biosphere. *Science*, 1431–1434. https://doi.org/10.1126/science.1169473

Shackleton, S., Bereiter, B., Baggenstos, D., Bauska, T. K., Brook, E. J., Marcott, S. A., & Severinghaus, J. P. (2019). Is the noble gas-based rate of ocean warming during the Younger Dryas overestimated? *Geophysical Research Letters*. https://doi.org/doi: 10.1029/2019GL082971

Spahni, R., Schwander, J., Fluckiger, J., Stauffer, B., Chappellaz, J., & Raynaud, D. (2003). The attenuation of fast atmospheric CH4 variations recorded in polar ice cores. *Geophysical Research Letters*, *30*(11), 1571. https://doi.org/10.1029/2003GL017093

Stauffer, B., & Tschumi, J. (2000). Reconstruction of past atmospheric CO2 concentrations by ice core analyses. In T. Hondoh (Ed.), *Physics of Ice Core Records* (pp. 217–241). Hokkaido University Press.

Steig, E. J., Schneider, D. P., Mann, M. E. E., & Comiso, J. C. (2009). Warming of the Antarctic ice-sheet surface since the 1957 International Geophysical Year. *Nature*, *457*, 459–463. https://doi.org/https://doi.org/10.1038/nature07669

Chapter 4

Last Interglacial Peak Mean Ocean Temperature Due to Ocean Circulation Change

Abstract

The Last Interglacial (129-116 ka) represents one of the warmest climate intervals of the last 800,000 years and most recent time sea level was meters higher than modern. However, the timing and amplitude of peak warmth varies between reconstructions, and the relative sources contributing to elevated sea level during the Last Interglacial remain uncertain. Here, we present the first mean ocean temperature record for this interval from noble gas measurements in ice cores and constrain the thermosteric component of sea level. Mean ocean temperature reaches its maximum value of 1.1±0.3°C warmer-than-modern at the end of the penultimate deglaciation at 129 ka, resulting in 0.7±0.3m higher-than-modern thermosteric sea level. However, this maximum in ocean heat content is short-lived; mean ocean temperature cools in the first several thousand years of the interglacial and achieves a stable, comparable-to-modern value by ~127 ka. Comparison to other proxy records suggests that the peak in mean ocean temperature is a transient feature of the Last Interglacial, related to the accumulation of heat in the ocean interior during the preceding period of reduced overturning circulation.

4.1. Introduction

With a heat capacity one thousand times larger than that of the atmosphere, the ocean plays an important role in regulating the rate and magnitude of global temperature change. Ocean heat uptake and warming contributes directly to increasing sea level through thermal expansion of seawater, and may play a role in future sea level rise through enhanced sub-shelf melting and subsequent mass loss from the Antarctic Ice Sheet (Paolo et al., 2015; Pritchard et al., 2012; Schoof, 2007). To understand the future role of ocean heat uptake, it is instructive to study ocean temperature change during past warm periods in Earth's history.

During the Last Interglacial (LIG, 129-116 ka) surface temperatures were somewhat warmer than today, however existing reconstructions differ substantially on the timing and magnitude of peak warmth. The global air surface temperature reconstruction by Snyder (2016) shows maximum 2°C warmer temperatures during the middle of the LIG including both ocean and land surfaces, while a sea surface temperature reconstruction by Hoffman et al. (2017) shows a maximum of only 0.5°C warmer-than-modern on a global scale that peaks during the earlier LIG, but up to 1°C warmer in the high latitudes. Climate model results show considerable warmth at the mid-LIG, especially in the high northern latitudes, but in line with the lack of global insolation forcing, little warming or even cooler temperatures on a global scale (Otto-Bliesner et al., 2013). At the same time, global sea level during the LIG was 6-9 m higher (Kopp et al., 2009). Differences in greenhouse gas and orbital forcing over the LIG relative to modern make the spatial and temporal patterns of temperature change during this period distinct from what might be expected from anthropogenic warming (Masson-Delmotte et al., 2010). As a result, the LIG is not an analogue for future warming but offers a unique opportunity to assess the validity of earth system

model predictions of sea level rise in response to warming, provided that reliable paleoclimate data exist for model validation (Fischer et al., 2018).

Sediment cores provide valuable records of changes in ocean conditions through the LIG (e.g. Capron et al., 2014; Deaney et al., 2017; Hoffman et al., 2017; Shakun et al., 2015) and are critical to understanding the spatiotemporal structure of temperature change across the ocean basins. However, because changes in local ocean temperature can also reflect changes in ocean circulation (Forget & Ferreira, 2019), deducing total ocean heat content from these records remains challenging.

The measurement of atmospheric noble gases trapped in glacial ice provides an alternative to reconstruct changes in mean ocean temperature (MOT) independently from marine records (Bereiter, Shackleton, et al., 2018; Headly & Severinghaus, 2007; Ritz et al., 2011). Changes in the relative atmospheric concentrations of krypton, xenon and nitrogen trace total ocean heat content because they are caused by temperature-driven changes in gas solubilities in ocean water. In this study, we report measurements of the ratios of Kr/N_2, Xe/N_2, and Xe/Kr in ice cores from the Taylor Glacier blue ice area and the EPICA Dome C (EDC) ice core that cover the LIG and penultimate glacial, Marine Isotope Stage 6 (MIS6, 180-135 ka). We assess the timing and magnitude of ocean temperature change during the LIG and quantify the thermosteric component of elevated sea level during this period.

4.2. Results

MOTs were derived from Kr/N_2, Xe/N_2, and Xe/Kr measurements in Taylor Glacier and EDC ice core samples (Figure 1). For both ice cores, MOT is calculated relative to early Holocene

(10 - 11 ka) MOT samples from each core due to the more robust results for relative (versus absolute) MOT (see methods/supplementary materials). MOT is then calculated relative to modern from the WAIS Divide (Bereiter, Shackleton, et al., 2018) and EDC (Baggenstos et al., 2019) Holocene to preindustrial MOT records and preindustrial to modern simulations of ocean heat content (Gebbie & Huybers, 2019). Based on Monte Carlo simulations that account for all known sources of uncertainty we constrain peak MOT to 1.1±0.3°C (1σ) warmer than modern at 128.9±0.7 ka on the AICC2012 age scale (Bazin et al., 2013). While the data for MIS6 and Termination II are relatively sparse, the period of maximum MOT is highly resolved. Because of this, and the robust age constraints from trace gas measurements for the Taylor Glacier record (see methods/supplementary materials), the timing of peak MOT is well constrained.

The record shows a 3.4±0.5°C MOT warming from MIS6 to the early LIG, compared to the 2.6±0.3°C change between the LGM and Holocene (Bereiter, Shackleton, et al., 2018). The larger magnitude in glacial-interglacial MOT change over Termination II compared to Termination I is consistent with previous reconstructions of deep ocean temperature change during these intervals from an average of low-resolution marine sediments (Shakun et al., 2015). Crucially, the methods used to date the ice cores are completely independent from the MOT record itself. We can thus compare our record to other proxies from this period without any implicit assumptions about (a)synchronicity of changes.

4.3. Discussion

4.3.1 Comparison to global surface temperature records

The MOT maximum we find in this study is larger in magnitude than the global sea surface temperature (SST) anomaly reported by Hoffman et al. (2017, Figure 2). Rather, the magnitude

of the peak extratropical SST anomaly agrees well with the peak MOT anomaly. While global SST reconstructions are good indicators of the 'skin temperature' and thus outgoing longwave radiation for much of the planet, MOT is closely related to the subsurface and total ocean heat content (Baggenstos et al., 2019). MOT represents volume-averaged ocean temperature, so changes in intermediate and deep ocean temperatures (as opposed to SST changes) play a dominant role in setting MOT. Much of the intermediate and deep ocean's temperature is set at high latitudes via meridional circulation, so the polar regions are likely crucial for the structure of MOT change, relative to that of global SST.

The MOT maximum occurs several thousand years earlier than the global SST maximum but is synchronous (within uncertainty) with peak Antarctic surface temperature (Bazin et al., 2013; Jouzel et al., 2007). This follows the pattern of MOT change recently observed during Termination I (Baggenstos et al., 2019; Bereiter, Shackleton, et al., 2018) in which MOT and high southern latitude surface temperatures appear intrinsically linked. We thus have strong evidence that MOT both outpaces and exceeds low latitude SST during the LIG, which strongly suggest polar amplification and intermediate/deep-water formation are key regulators of MOT.

4.3.2 Links of MOT and Ocean Circulation across Termination II and the LIG

Recent studies have investigated the role of the bipolar seesaw, the out-of-phase temperature variations between hemispheres, during glacial terminations (Barker et al., 2011; Cheng et al., 2009; Deaney et al., 2017; Marino et al., 2015). While several alternative hypotheses have been proposed (Dokken et al., 2014; Petersen et al., 2013), the leading hypothesis has long been that the bipolar seesaw is driven by mode changes of the Atlantic Meridional Overturning Circulation (AMOC, Broecker, 1998; Stocker and Johnsen, 2003). When AMOC is in a strong

mode, as today, there is northward heat transport at all latitudes in the Atlantic. When AMOC is weakened this heat transport is reduced, leading to a net accumulation of heat in the Southern Hemisphere.

Proxy records from the North Atlantic (Deaney et al., 2017), Chinese speleothems (Cheng et al., 2009), and Antarctic ice cores (Masson-Delmotte et al., 2010) suggest that the AMOC was significantly weakened during Heinrich Stadial 11 (HS11, ~135-129 ka), a cold period in the Northern Hemisphere that covers much of Termination II. At ~129 ka, these proxy records show a rapid recovery of AMOC and Asian monsoon strength, coinciding with the peak in Antarctic temperature and MOT in our reconstruction (Figure 3). The excellent agreement in the timing of peak MOT (128.9±0.7 ka) and the end of Heinrich Stadial 11 (HS11, 128.9±0.06 ka) dated from the Sanbao Cave records suggests an important connection between MOT and the bipolar seesaw.

Recent modeling studies have examined the impact of AMOC weakening on surface and subsurface ocean temperature change through freshwater hosing experiments (Galbraith et al., 2016; Pedro et al., 2018). In these simulations reduction in AMOC strength results in net SST cooling while heat accumulates in the ocean interior. The surface temperature anomaly has a globally asymmetric pattern with strong and rapid cooling in the North Atlantic concurrent with slow and steady warming of the Southern Hemisphere. The accumulated subsurface heat is released at the subsequent recovery of the AMOC, followed by an overall surface warming and MOT cooling.

This spatiotemporal pattern is consistent with the decoupling between SST and MOT we observe during HS11 and the LIG (Figure 2). During HS11, the AMOC was weakened, leading to an accumulation of heat in the ocean interior and Southern Hemisphere. Once the AMOC recovered at ~129 ka the net accumulation of subsurface heat was released, and MOT transitioned

from warming to cooling. This mechanism may also explain the offset in timing between MOT and SST maxima, as the release of heat from the ocean interior subsequently leads to a net surface warming, particularly in the Northern Hemisphere high latitudes.

These results raise the question of how much of the warmer-than-modern MOT in the early LIG was due to the weakened AMOC state, and how much can be attributed to the stable interglacial climate? In our record, MOT cooled and eventually stabilized by ~127 ka at a temperature that is comparable to modern MOT (+0.2±0.3°C relative to Holocene/modern). If we believe that the cooling was entirely caused by the release of stored heat after AMOC recovery, then we can attribute most of the MOT anomaly at the LIG onset to deglacial changes in ocean circulation.

While our record of Termination II lacks temporal resolution at the onset of warming, it is interesting to note MOT only increased during times when AMOC was in a weakened state, alluding to the importance of AMOC interruptions in driving the climate out of a stable glacial state (Baggenstos et al., 2019; Galbraith et al., 2016). The Northern Hemisphere insolation forcing during Termination II exceeded that of Termination I, which may in part explain the comparatively rapid disintegration of the Northern Hemisphere ice sheets during Termination II, and long duration of HS11 due to strong freshwater forcing of the North Atlantic (Marino et al., 2015).

In contrast, during Termination I the AMOC temporarily recovered mid-termination, possibly due to the weaker insolation and thus reduced freshwater forcing of the North Atlantic. During this time, both Antarctica and MOT cooled. The so-called 'Antarctic Cold Reversal', may in many ways be analogous to the MOT cooling we see at the end of Termination II, post AMOC recovery. While the MOT cooling over the Antarctic Cold Reversal (~0.5°C) was slightly smaller in magnitude than what we observe during the LIG onset, the net warming of Heinrich Stadial I

and the Younger Dryas of 3.4±0.4°C is remarkably similar to the net warming found for the MIS6-peak LIG MOT change of our record (3.4±0.5°C). In addition, the magnitude of glacial-interglacial change across Termination II once MOT has stabilized is 2.5±0.5°C, which is comparable to the magnitude of MOT change across Termination I (2.6±0.3°C). This suggests that the AMOC interruptions during the past two terminations transiently provided an additional ~1°C of MOT warming above the net glacial-interglacial MOT change. Several studies comparing Termination I and Termination II have posited that the larger magnitude of changes in Antarctic temperature (Masson-Delmotte et al., 2010) and CO_2 (Deaney et al., 2017) observed for Termination II are related to the delayed recovery of AMOC strength. Our record suggests the same is true for MOT change across Termination II.

4.3.3 Implications for West Antarctic Ice Sheet stability

The MOT changes across the LIG have direct and indirect implications for sea level. Pinning down the sources contributing to the LIG global mean sea level highstand is crucial to understanding the vulnerability of modern ice sheets to global warming. From CMIP5 estimates of the long term thermosteric sensitivity to heat uptake (Kuhlbrodt & Gregory, 2012), we find that the 1.1±0.3°C MOT anomaly during the early stages of the LIG contributed 0.7±0.3m to elevated sea level. By ~127 ka MOT had cooled to near-modern values, and no appreciable thermosteric contribution (relative to modern) is expected by this early stage in the interglacial. In fact, our record implies a trend of thermosteric sea level lowering in the first ~2000 years of the LIG. Coral reef records (Dutton et al., 2015) indicate that sea level was already 6±2 meters higher than modern at 129 ka, requiring a substantial ice sheet (in addition to the thermosteric) contribution early in the LIG to explain this magnitude of elevated sea level.

Early MOT warming may have played another, more indirect role in contributing to sea level rise during the LIG. In recent Antarctic Ice Sheet simulations of the LIG (Pollard & Deconto, 2016; Sutter et al., 2016), ocean warming played an important role in mass loss from the West Antarctic Ice Sheet. Pollard and Deconto (2016) found that if ocean warming occurred shortly after the glacial termination, the West Antarctic Ice Sheet was more prone to lose mass because of enhanced reverse-sloped beds at grounding lines. By invoking sub-shelf melting through Southern Ocean warming, Sutter et al. (2016) derive the highest sea level rise-rates during maximum Antarctic temperatures at the end of Termination II, thus, synchronous to our MOT maximum. The delay in AMOC recovery and resulting accumulation of heat in the ocean interior and Southern Hemisphere at the end of Termination II may therefore have played an important role in West Antarctic Ice Sheet mass loss and elevated sea level during the LIG.

An important caveat to consider for this hypothesis is that MOT is not a proxy for ocean temperatures directly under ice shelves, and warmer MOT does not necessarily imply that temperatures in vulnerable sub-ice shelf regions were enhanced. However, MOT and the temperature of circumpolar deep water are intrinsically linked, because circumpolar deep water is made up of a representative mixture of waters from all ocean basins (Elderfield et al., 2012) and is brought efficiently to the surface by isopycnal mixing in the Southern Ocean. If, as today, circumpolar deep water intruded onto the Antarctic continental shelf, its ice melting capacity would be enhanced during the early stages of the LIG.

4.4. Conclusions

The ocean heat anomaly provided from our MOT reconstruction is a simple, but important metric to evaluate in earth system models, making it useful for future simulations of the LIG. The record presented here shows MOT reached values of 1.1°C warmer-than-modern during the Last Interglacial. The timing of peak MOT coincides with that of Antarctic temperature and the abrupt recovery of AMOC at the end of Termination II. Enhanced MOT contributed directly to elevated thermosteric sea level during the early stages of the LIG and may have played an indirect role in contributing to the sea level highstand through ocean forcing of West Antarctic Ice Sheet mass loss. MOT decreased to near-modern values by ~127 ka, when peak SSTs were observed in the Northern Hemisphere. Comparison of our record with other paleo indicators and model results suggest peak MOT was related mainly to global ocean circulation changes that occurred over Termination II, rather than the LIG warmth itself; studying the LIG in the context of the deglaciation that precedes it provides a more complete view of the climate evolution that occurs over this interval.

Appendix 4.A: Taylor Glacier Sampling and Site Description

Taylor Glacier is an outlet glacier of the East Antarctic Ice Sheet with a >80 km long ablation zone exposing easily accessible old ice at the surface. Its accumulation zone is located on the northern flank of Taylor Dome and it terminates in Taylor Valley. Extensive work on mapping the stratigraphy of the glacier identified ice from the LIG located near the terminus of the glacier (Aarons et al., 2019; Baggenstos et al., 2017; Buizert et al., 2014).

For this study, a total of four large-diameter ice cores were collected during the 2014/15 and 2015/16 Antarctic field seasons (Figure S1 in supplement). Two cores spanning approximately 120 to 155 ka were collected approximately 4 km from the glacier terminus. Additionally, two cores were drilled along a previously-established across-flow transect (Baggenstos et al., 2017) from the early Holocene (10.6 ka) and Last Glacial Maximum (LGM, 19.9 ka) to serve as a comparison to LIG and MIS6 MOT samples. Cores were drilled with the Blue Ice Drill (Kuhl et al., 2014) and are approximately 24 cm in diameter. Cores were processed and subdivided in the field and analyzed for noble gases for MOT reconstruction as well as other atmospheric gases used to establish the time scale for the record.

Appendix 4.B: Taylor Glacier Core Chronology

A major challenge in sampling a blue ice area is establishing ages for the samples (Bintanja, 1999). Ice from Taylor Glacier has traveled tens of kilometers from its deposition site and has likely undergone non-uniform thinning and folding. While the dynamics of the glacier have been studied in detail (Aciego et al., 2007; Kavanaugh & Cuffey, 2009), not enough is known about the basal topography or subsurface ice flow to build a chronology for the glacier from a glaciological model.

We therefore use alternative methods to construct the chronology for our samples. Previous work in blue ice areas (Baggenstos et al., 2017; Bauska et al., 2016; Menking et al., 2018; Petrenko et al., 2006) has demonstrated success in establishing ice sample chronologies through value and/or inflection point matching with well-dated ice core records of globally well-mixed atmospheric gases (Blunier et al., 2007). For this study the chronology was constructed using a least-squares

fitting method with measurements of methane concentrations (CH_4), molecular oxygen isotopic composition ($\delta^{18}O_{atm}$), and carbon dioxide concentrations (CO_2), tied to EPICA Dome C (EDC) reference records (Landais et al., 2013; Loulergue et al., 2008; Schneider et al., 2013) on the Antarctic Ice Core Chronology (AICC2012) (Bazin et al., 2013; Veres et al., 2013). This method allows for a construction of an age probability distribution for each noble gas sample that can be used to assess sample age uncertainty (see supplement).

Appendix 4.B: Taylor Glacier Core Chronology

A major challenge in sampling a blue ice area is establishing ages for the samples (Bintanja, 1999). Ice from Taylor Glacier has traveled tens of kilometers from its deposition site and has likely undergone non-uniform thinning and folding. While the dynamics of the glacier have been studied in detail (Aciego et al., 2007; Kavanaugh & Cuffey, 2009), not enough is known about the basal topography or subsurface ice flow to build a chronology for the glacier from a glaciological model.

We therefore use alternative methods to construct the chronology for our samples. Previous work in blue ice areas (Baggenstos et al., 2017; Bauska et al., 2016; Menking et al., 2018; Petrenko et al., 2006) has demonstrated success in establishing ice sample chronologies through value and/or inflection point matching with well-dated ice core records of globally well-mixed atmospheric gases (Blunier et al., 2007). For this study the chronology was constructed using a least-squares fitting method with measurements of methane concentrations (CH_4), molecular oxygen isotopic composition ($\delta^{18}O_{atm}$), and carbon dioxide concentrations (CO_2), tied to EPICA Dome C (EDC) reference records (Landais et al., 2013; Loulergue et al., 2008; Schneider et al., 2013) on the Antarctic Ice Core Chronology (AICC2012) (Bazin et al., 2013; Veres et al., 2013). This method

allows for a construction of an age probability distribution for each noble gas sample that can be used to assess sample age uncertainty (see supplement).

Appendix 4.C: Taylor Glacier Noble Gas Measurements

Taylor Glacier measurements of noble gases for MOT reconstruction were made at Scripps Institution of Oceanography (SIO). A total of 45 ice samples from the 2014/15 and 2015/16 cores were analyzed, including eight replicate samples, giving 37 unique MOT samples. In addition, at SIO and Bern five samples from the Holocene (10.6 ka) and five from the LGM (19.9 ka) were measured (Figure 3) at each institution. The motivation for this analysis was to verify the quality of the noble gas records by comparison to published MOT records (Bereiter et al., 2018a), and to verify that any offsets in the EDC and Taylor Glacier MOT results were unrelated to lab offsets (see supplementary materials).

The analytical methods for noble gas measurements are described in detail by Bereiter et al. (2018b). In short, ~800 grams of ice were melted under vacuum and liberated gases (~80 ml STP) were cryogenically trapped in stainless steel dip tubes. After gas extraction, the samples were split into two aliquots. The larger (~78 ml STP) aliquot was exposed to a Zr/Al alloy at 900°C to remove all non-noble gases and measured on a Thermo-Finnigan MAT-253 isotope ratio mass spectrometer via dual inlet method for $^{40}Ar/^{38}Ar$ ($\delta^{40/38}Ar$), $^{40}Ar/^{36}Ar$ ($\delta^{40/36}Ar$), $^{86}Kr/^{84}Kr$ ($\delta^{86/84}Kr$), $^{86}Kr/^{83}Kr$ ($\delta^{86/83}Kr$), $^{86}Kr/^{82}Kr$ ($\delta^{86/82}Kr$), $^{84}Kr/^{40}Ar$ ($\delta Kr/Ar$), and $^{132}Xe/^{40}Ar$ ($\delta Xe/Ar$). The smaller aliquot (~2 ml STP) was passed through a cryotrap (-196°C) to remove CO_2 and measured on a Thermo-Finnigan MAT Delta V isotope ratio mass spectrometer via dual inlet method for $^{29}N_2/^{28}N_2$ ($\delta^{15}N$), $^{34}O_2/^{32}O_2$ ($\delta^{18}O$), $^{32}O_2/^{28}N_2$ ($\delta O_2/N_2$), and $^{40}Ar/^{28}N_2$ ($\delta Ar/N_2$).

Measurements were corrected for pressure imbalance and chemical slope according to established procedure (Severinghaus et al., 2003).

All data are reported in delta notation, relative to a modern atmosphere standard. Because argon is preferentially lost relative to xenon and krypton during ice bubble formation (Severinghaus & Battle, 2006), we mathematically combine δXe/Ar, δKr/Ar, and δAr/N_2 to obtain δKr/N_2, δXe/N_2, and δXe/Kr.

Appendix 4.D: Taylor Glacier Fractionation Corrections

To reconstruct ocean temperature from δKr/N_2, δXe/N_2 and δXe/Kr, it is necessary to correct for fractionation during firnification, the process by which fresh snow compacts, transitioning to denser firn and eventually to glacial ice containing air trapped in bubbles. While the free troposphere is well mixed through convective processes, the low permeability of the firn restricts bulk flow; gases within the firn column are transported primarily via molecular diffusion (Schwander et al., 1988). This allows for gravitational settling and thermal diffusion to alter firn air from its atmospheric composition before it is occluded in glacial ice (Craig et al., 1988; Severinghaus et al., 1998). As such, δKr/N_2, δXe/N_2 and δXe/Kr must be corrected for fractionating processes to derive the paleoatmospheric composition for inferring MOT.

As suggested by Bereiter et al., (2018a), under/over-correction of fractionation may lead to systematic offsets in MOT, but the effect primarily impacts the absolute MOT anomaly (relative to modern) and has little impact on relative MOT change within a record. We investigate the influence of the choice in methods of fractionation correction on the MOT record and find that different methods shift the absolute MOT record up or down but have little effect on relative MOT change in the record for Taylor Glacier (see supplement). We thus compute the MOT anomalies

relative to the Taylor Glacier Holocene (10.6 ka) samples and then estimate the Holocene – modern MOT difference (and uncertainties) from the WAIS Divide MOT record and model simulations of ocean heat content over the last 2000 years (Gebbie & Huybers, 2019). A detailed description and assessment of the fractionation corrections is included in the supplementary materials.

Appendix 4.E: EDC Ice Core Noble Gas Analysis

Four EDC ice core samples from the LIG and four from MIS6 were analyzed at the University of Bern and included in this study. Measurement and data processing for these samples are similar to the analysis of Taylor Glacier samples with a few important distinctions (Baggenstos et al., 2019 and supplementary materials). Chronology uncertainties are not considered in this analysis, because the Taylor Glacier chronology is tied to that of EDC through ice core synchronization and contribute minimally to the total uncertainty for these samples. In addition, the approach to firn fractionation corrections differs slightly between Taylor Glacier and EDC (see section SI5 in the supplement).

Appendix 4.F: Derivation of MOT from Noble Gas Data

To reconstruct MOT values from fractionation-corrected $\delta Kr/N_2$, $\delta Xe/N_2$ and $\delta Xe/Kr$, we use the ocean-atmosphere box model of Bereiter et al. (2018a) with several modifications; we make no assumptions about the glacial-interglacial change in the ocean saturation state and use current estimates of krypton and xenon undersaturation (Hamme & Severinghaus, 2007) in the box model for the entirety of the record. We also do not invoke the glacial-interglacial changes in the relative water mass distributions that were applied in the Bereiter et al. (2018) study and use the

modern distributions of Antarctic Bottom Water and North Atlantic Deep Water to derive MOT over the full record.

We account for the effects of changes in ocean salinity, volume, and atmospheric pressure on the oceanic inventories of krypton, xenon and nitrogen using the sea level record of Grant et al. (2014) corrected for isostatic effects (Grant et al. 2014 and supplement). We also include the influence of the large ice shelf over the Arctic during MIS6, which holds the equivalent of 15 meters of sea level, influencing ocean salinity and volume, but not sea level (Nilsson et al., 2017).

To assess uncertainty in our MOT record we run 10,000 Monte Carlo simulations of our reconstruction with all known analytical and dating uncertainties in the MOT and sea level records, as well as the uncertainty in the Holocene-to-modern MOT change. We include uncertainties in measured Kr/N_2, Xe/N_2 and Xe/Kr and the isotope data used to correct for firn processes in our simulations, as well as the method used for fractionation corrections (see supplementary section SI3). To account for age uncertainties in the MOT record, we use an inverse transform method to randomly sample from our age probability distribution to include in our Monte Carlo simulations (Kolmogorov, 1950 and supplementary section SI1). For our final uncertainty estimate, we use the average of the three MOT records (and the Monte Carlo simulations) from Kr/N_2, Xe/N_2 and Xe/Kr to minimize the influence of analytical noise from any single measurement.

4.S1. Core Chronology

For the Blue Ice Drill (BID) core collected in the 2014/15 season, discrete CH_4 measurements were made at Oregon State University following the method described in Mitchell et al. (2011). For the 2015/16 core, continuous-flow methane measurements were made at Desert

Research Institute following Rhodes et al. (2013). Due to complications during the continuous flow melting process, the 2015/2016 core is missing 1.66 meters of CH_4 measurements (Figure S2), resulting in 4 MOT samples without age constraints from CH_4 information. For additional chronological constraints 10 of the 45 MOT samples were measured at OSU for CO_2 following methods described in Ahn, Brook, & Howell (2009). These samples include the four depth intervals that are missing CH_4 data, as well as six additional samples from adjacent depths.

The measurements required for the molecular oxygen isotopic composition ($\delta^{18}O_{atm}$) are included in the noble gas measurement method described in the methods section of the main text. $\delta^{18}O$ of O_2 measured in glacial ice is affected by gravitational fractionation and gas loss; in order to derive $\delta^{18}O_{atm}$ it is necessary to correct for both of these processes (Severinghaus et al., 2009). Gravitational fractionation corrections are made with $\delta^{15}N$:

$$\delta^{18}O_{gravcorr} = \delta^{18}O_{measured} - 2 \times \delta^{15}N_{measured}$$

There are several approaches to the gas loss correction. A Taylor Glacier specific gas loss correction (Baggenstos et al., 2017) uses measured $\delta O_2/N_2$ and $\delta Ar/N_2$:

$$\delta^{18}O_{atm} = \delta^{18}O_{gravcorr} + 0.0119 \times \delta O_2/N_{2,gravcorr} - 0.0115 \times \delta\, Ar/N_{2,gravcorr}$$

The correction used for the EDC reference record (Extier et al., 2018) uses only $\delta O_2/N_2$:

$$\delta^{18}O_{atm} = \delta^{18}O_{gravcorr} + 0.01 \times \left(\delta O_2/N_{2,gravcorr} + 10\right)$$

Applying the Taylor Glacier specific correction to the data minimizes the difference in $\delta^{18}O_{atm}$ between duplicate samples. However, compared to the EDC reference record, TG-corrected $\delta^{18}O_{atm}$ are slightly negative by ~0.05‰. If we apply the correction from Extier et al., (2018) to the TG data there is worse agreement between duplicate samples, but no apparent offset

between the EDC and TG records. For consistency, and to avoid potential bias due to offsets between the two records, we chose to apply the Extier et al., (2018) correction for this study.

By comparing the gas records on their depth scale to well-dated ice core records, we find evidence for folding and non-uniform thinning in both cores (Figure S2). For this reason, we chose to construct an age probability distribution for each individual sample rather than tie point selection and linear interpolation. This approach does not impose a monotonically changing age scale with depth. Instead, each MOT sample age is determined individually to allow for the possibility of thinning and folding.

In order to construct an age probability distribution, we first created a linearly interpolated reference record of CH_4 (Loulergue et al., 2008), $\delta^{18}O_{atm}$ (Extier et al., 2018) and CO_2 (Schneider et al., 2013) at 10 year resolution on the AICC2012 timescale (Bazin et al., 2013).

We then assessed the fit (F) for each sample in our record to each point in the interpolated reference curve assuming a Gaussian distribution:

$$F_{18Oatm}(t) = \frac{1}{\sqrt{2\pi\sigma^2_{\delta 18Oatm}}} e^{\frac{-\left(\delta^{18}O_{atm\,meas} - \delta^{18}O_{atm\,ref}(t)\right)^2}{2\sigma^2_{\delta 18Oatm}}}$$

$$F_{CH4}(t) = \frac{1}{\sqrt{2\pi\sigma^2_{CH4}}} e^{\frac{-\left(CH_{4\,meas} - CH_{4\,ref}(t)\right)^2}{2\sigma^2_{CH4}}}$$

$$F_{CO2}(t) = \frac{1}{\sqrt{2\pi\sigma^2_{CO2}}} e^{\frac{-\left(CO_{2\,meas} - CO_{2\,ref}(t)\right)^2}{2\sigma^2_{CO2}}}$$

Where σ is the combined 1-sigma error reported for the reference records and the pooled standard deviation of gas measurements made for this study (Table S2). Recent studies have

suggested the potential for slight offsets to exist in CO_2 content between individual ice cores (Ahn et al., 2012; Bereiter et al., 2012; Eggleston et al., 2016; Marcott et al., 2014). In addition to analytical uncertainties, we include a 5-ppm uncertainty in σ_{CO2} to account for a potential offset between the TG and EDC CO_2:

$$\sigma_{CO2} = \sqrt{\sigma_{TG}^2 + \sigma_{EDC}^2 + \sigma_{offset}^2}$$

We then combine the probability distribution functions for the measured gases:

$$F(t) = F_{\delta 18Oatm}(t) \cdot F_{CH4}(t) \cdot F_{CO2}(t)$$

The probability of the sample being a particular age P(t) is then defined as:

$$P(t) = \frac{F(t)}{\sum F(t)}$$

The depth versus age curves produced from this method also suggest the presence of folds. In addition to identifying the most probable age, the motivation for creating an age probability distribution for each sample was for its application to Monte Carlo simulations to assess MOT uncertainty. Age uncertainty directly impacts MOT uncertainty, because it translates into uncertainty in sea level, which is a required input in the ocean-atmosphere box model to derive MOT. A sea level record is necessary to account for the effect of changes in salinity, ocean volume, and sea level pressure on the ocean inventories of krypton, xenon, and nitrogen.

We sampled from our age probability distribution using the inverse transform method (Kolmogorov, 1950) to allow for Monte Carlo simulations with non-normal age probability distributions. While this method allows for objective quantification of age uncertainty, we made three assumptions about the absolute age and structure of the probability distribution to refine the age models.

Our first assumption was that the age of our samples lies within a restricted range. Based on radiometric and stratigraphic dating of this region of Taylor Glacier (Baggenstos, 2015; Buizert et al., 2014), we limited the probability distribution range for the record to the LIG and the penultimate glacial period, between 120 and 155 ka. Without bounds, small spurious peaks in the probability distribution during intervals with similar atmospheric compositions (i.e. other glacial and interglacial intervals) skewed the results of our Monte Carlo simulations.

We applied a second assumption in sampling from the age probability distributions. Because our probability distributions were constructed from least squares fitting to reference records, there are small (but non-zero) probabilities for each sample to be any age within the distribution. This can result in probability distributions with long tails that skew the age distribution. To prevent these tails from biasing the results of the Monte Carlo simulations we defined a minimum probability threshold before sampling from each distribution. For each sample we restricted the sampling distribution to only ages with probabilities (P(t)) that were at least 5% of the maximum age probability or greater (Figure S3). This allows the distributions to be wide and non-normal but prevents long tails from skewing the results of the simulations.

The third assumption in our age model was related to the structure of the probability distribution. To assess the 'goodness of fit' for each distribution, we examined the difference between the most probable age and the median age for each sample (Figure S3). The most probable age occurs at the time in the reference record with the best least squares fit between the measured gases and the reference gases i.e. when P(t) is maximized. The median age describes the 50^{th} percentile in the distribution, i.e. the point at which where there is an equal probability of the age lying on either side of the distribution. If the absolute difference between the 'peak age' and 'optimal age' was greater than 1000 years, we rejected this sample (total rejected samples = 4).

We believe that the age uncertainties of these samples added substantial uncertainty to the whole record and thus did not include them for the remainder of the analysis.

There are some limitations in this approach. For one, we assumed that the reference record is sampled at an adequately high resolution. If the resolution is too coarse, a feature in the atmospheric record may not be included (e.g. a methane spike associated with a millennial scale oscillation). It is also possible that a single outlier (such as the methane spike at 134 ka) in the reference record is due to an analytical error and does not reflect the true atmospheric history. For more context, we compared the EDC gas records to those of Vostok (Bazin et al., 2013). We have no reason to believe that these problems exist for our reference records, but they should be kept in mind.

Another limitation of this method arises when there are only small variations in the gas records over time. During glacial terminations, there are large changes in atmospheric methane, $\delta^{18}O_{atm}$, and CO_2, making the method robust. However, during periods of stable climate, gas isotopes and concentrations change very little with time, making it difficult to pinpoint an age. This is why samples from the penultimate glacial have much larger age uncertainties than those covering Termination II and the early Last Interglacial.

It is also important to emphasize that this method inherently assigns age and age uncertainties *relative* to the reference chronology. There are absolute age uncertainties in the AICC2012 chronology that are not incorporated into this study.

4.S2. Converting Red Sea Level to Eustatic Sea Level for Box Model

As with all relative sea level records, the Red Sea Level (RSL) record is influenced by isostatic effects, which decouple RSL from eustatic sea level, the input that is required for the box model in order to calculate MOT. In the case of RSL, the largest offset from eustatic sea level occurs during glacial maxima (Grant et al., 2014). From ice sheet simulations, Grant et al, (2014) finds a relationship between RSL and ESL, which is dependent on whether the Northern Hemisphere ice sheets are glaciating or deglaciating (Figure S5). However, the deglaciating correction appears to overestimate the LIG sea level highstand (Kopp et al., 2009), while the uncorrected RSL curve appears to better capture its magnitude. We thus choose to interpolate between the glaciating and uncorrected RSL curves over the deglaciation (140-129 ka) and use the glaciating RSL curve during MIS6 and uncorrected RSL curve over the LIG. We note that the difference in resulting MOT from any of the three RSL scenarios (uncorrected, glaciating, and deglaciating) are within our reported error, so the choice in sea level curve does not influence the findings of our study. However, given the data constraints on the sea level highstand and the modeling results for the isostatic influence on RSL, we believe this choice in sea level curve is the best representation to apply in our box model to calculate MOT.

4.S3. Lab Intercomparison Study

The Taylor Glacier and EDC measurements were made at different labs using slightly different analytical methods, so we must consider the possibility that differences between ice core MOT results may be the consequence of lab offsets. We thus conducted an intercomparison study in which the SIO and Bern labs measured isotope and elemental ratios required for MOT

reconstruction on one ice core from the Holocene (10.6 ka) and one from the LGM (19.9 ka) and compared the results. The cores were collected from a previously established well-dated transect of Taylor Glacier (Figure S1, Baggenstos et al., 2017) where the ice layer dip is vertical, so each core contains ice of the same age. Five samples were analyzed for each Holocene and LGM core at each institution for a total of 20 sample measurements. The results show excellent agreement between the labs for both the Holocene and LGM samples (Table S1), which gives us confidence that there is no lab offset, and any differences between the EDC and Taylor Glacier MOT results are in the ice. Possible differences in MOT results between cores may be attributed to systematic error in firn fractionation corrections.

4.S4. Fractionation Corrections

4.S4.1 Reconstructions of atmospheric $\delta Kr/N_2$, $\delta Xe/N_2$ and $\delta Xe/Kr$

In order to reconstruct atmospheric noble gas content for MOT, we assume that the isotope and elemental ratios we measure in ice represent the atmospheric composition, plus some combination of gravitational, thermal, and kinetic fractionations:

$$\delta'_{meas} = \delta'_{atm} + \delta'_{grav} + \delta'_{therm} + \delta'_{kin} + \left(\delta'_{degas}\right)$$

Where $\delta' = \ln(q)$ and $q = R_{sample}/R_{standard}$ (Markle, 2017). It is convenient to use δ' here instead of the nearly equivalent standard delta, because fractionations in terms of δ' are truly linear, and an exact form of gravitational fractionation (the largest source of fractionation in our system) can be expressed in terms of δ'.

Isotope ratios of nitrogen, argon (corrected for geological ^{40}Ar degassing, or δ'_{degas}, see SI4.5), and krypton have not changed in the atmosphere over time interval covered in this study, making the measured values a sum of all fractionations in the firn. In order to remove the effect of

these fractionations on our MOT proxies, we set up a linear least-squares system of all available isotope data to quantify each fractionation (as in Shackleton et al., 2019 and Baggenstos, 2015). Because the precision of these isotope measurements varies substantially (Table S2) we also use a weighting factor of $1/\sigma^2$ where σ is the 1σ uncertainty for of a given isotope measurement in our linear least squares system.

4.S4.2 Gravitational fractionation

The largest source of fractionation for isotopes and $\delta Kr/N_2$, $\delta Xe/N_2$ and δXe/Kr (hereafter referred to as MOT proxies) is gravitational settling in firn (Schwander, 1989; Craig et al., 1988). Through the entire diffusive zone of the firn column, settling is mass-dependent:

$$\delta'_{grav} = \frac{\Delta m_{x-y} g z}{RT}$$

where Δm is the mass difference of the gas pair (x-y, in kg/mol), g is the gravitational constant, z is depth in the diffusive column, R is the gas constant, and T is average firn temperature in Kelvin, which was calculated with the Taylor Dome water isotope record (Steig et al., 1998) as in (Steig et al., 2000).

4.S4.3 Thermal Fractionation

If a thermal gradient exists in the firn, thermal diffusion will also affect the isotopes and MOT proxies:

$$\delta'_{therm} = \Omega_{x-y} \Delta T$$

Where Ω is the laboratory-determined thermal diffusion sensitivity (Grachev & Severinghaus, 2003) for a specific gas pair (x-y) and ΔT is the temperature difference (top minus bottom) across the firn column.

4.S4.4 Kinetic fractionation/Heavy isotope deficit

Recent studies have explored the effect of kinetic fractionation or heavy isotope deficit (HID) in the firn and its influence on MOT proxies (Birner et al., 2018; Kawamura et al., 2013). Kinetic fractionation arises from the competing processes of molecular diffusion and the macroscopic advection of air. Sources of kinetic fractionation in the firn include convective zones (Kawamura et al., 2013; Severinghaus et al., 2010), barometric pumping (Buizert & Severinghaus, 2016), and the downward advection of gases during densification (Birner et al., 2018). While mechanisms for kinetic fractionation may vary, its influence on isotope ratios and MOT proxies is primarily dependent on the relative magnitudes of advection and molecular diffusion. Birner et al., (2017) found that while the absolute magnitude of HID may vary substantially between ice core sites, the relative scaling between isotopes and MOT proxies remains stable. This allows us to use a scaling factor, ϵ', to solve for the extent of kinetic fractionation:

$$\delta'_{kin} = \Delta m_{x-y}\ \epsilon'_{x-y}$$

Note that ϵ' is quantified relative to $^{29}N_2$ and $^{28}N_2$, which is the fastest diffusing measured gas pair in our system. Scaling factors for the isotopes and elemental ratios can be found in Birner et al., (2017).

4.S4.5 Changes in atmospheric ^{40}Ar due to geological degassing

While isotopes of nitrogen and krypton have not changed, the atmospheric concentration of ^{40}Ar has steadily increased over time due to the radioactive decay of ^{40}K in the crust and mantle (Bender et al., 2008). The effect on $\delta^{40/36}$Ar and $\delta^{40/38}$Ar can be corrected if the age of the sample is known:

$$\delta^{40/36}Ar_{degas} = 6.6 \times 10^{-5} \times gas\ age$$

$$\delta^{40/38}Ar_{degas} = 6.6 \times 10^{-5} \times gas\ age$$

Where gas age is in ka. Because the ice samples for this study are relatively young (~120-160 ka) the effect is nearly within the analytical uncertainty of the argon isotope measurements. Still, the effect is considered and corrections to $\delta^{40/36}$Ar and $\delta^{40/38}$Ar for degassing are made before these isotope pairs are input into the least squares systems used to correct the MOT proxies.

4.S4.6 EDC Fractionation Corrections

For EDC samples, we apply a similar method of quantifying firn air fractionations and correcting the MOT proxies to derive the past atmospheric composition. However, instead of a strictly least squares approach, we incorporate information beyond the available isotope measurements to quantify each source of fractionation, following the method described in Baggenstos et al, (2019). Because more is known about the accumulation and temperature history of the EDC ice core (relative to Taylor Glacier), a firn model was employed to determine the firn thermal gradient and to correct the isotope and elemental ratios for thermal fractionation. The extent of kinetic fractionation, or HID, was then quantified from the difference between thermally (and ^{40}Ar degassing) corrected and mass normalized argon, krypton and xenon isotopes, as described in the supplementary information of Baggenstos et al, (2019). Solutions for HID are quite noisy, due to the relatively lower analytical precisions of the krypton and xenon isotope ratios (Table S3), so it is advantageous to smooth the HID record to reduce the influence of this noise on the final MOT solution. Because the EDC LIG and MIS6 data are not evenly spaced, a boxcar filter of the HID (as applied in Baggenstos et al., 2019) is inappropriate. We separate the data into three <5 kyr segments and use the average HID difference to estimate kinetic fractionation for each interval. The MOT proxies are then corrected for kinetic fractionation using an empirical scaling factor, as described in SI3.4 (Birner et al., 2018). Finally, the MOT proxies were corrected

for gravitational fractionation from thermally and kinetically (and ^{40}Ar degassing) corrected $\delta^{40/36}Ar$. To explore the effect of choice in fractionation corrections on EDC MOT results, we compare MOT results with and without the HID correction.

4.S4.7 Taylor Glacier Results

As previously stated, gravitational settling is the largest source of fractionation for the isotopes and MOT proxies. Based on our knowledge of the Taylor Glacier accumulation region we expect kinetic and thermal fractionations to be minimal and the MOT proxies may not need to be corrected for their relative effects. Still, we consider the effect of including these fractionations in our linear least squares systems by comparing MOT results when we include terms for 1) gravitational fractionation only, 2) gravitational and thermal fractionations, 3) gravitational and kinetic fractionations, and 4) gravitational, thermal, and kinetic fractionations. To assess the validity of each method we applied these corrections to Taylor Glacier samples from the LGM and the Holocene and compared them to the WAIS Divide record. We also include the resulting MOT for the MOT LIG peak interval (129±0.8 ka) and MIS6 (136-160 ka).

An important result of comparing these methods is that while we don't expect the thermal and kinetic signals to be large, corrections including one or both of these fractionations yields quite different results in MOT than the corrections including gravitational settling alone (Table S4a). This suggests that these methods may be overestimating the degrees of thermal and kinetic fractionation, or that we may be missing or mischaracterizing a source of fractionation in the system. However, if we compare MOT for the LIG, LGM and MIS6 relative to the early Holocene all methods agree quite well (Table S4b), and the LGM – Holocene difference agrees with the WAIS Divide MOT record (2.6°C). This implies that while the methods may not be accurately characterizing and correcting for thermal and kinetic fractionation, the effect is relatively constant

over time. The different corrections shift the MOT record up and down in terms of absolute magnitude, but relative MOT change is insensitive to the choice of fractionation correction. This was also the case when these correction methods were applied to the WAIS Divide MOT record.

For this reason, we choose to compute the MOT anomaly relative to the Holocene (10.6 ka), and then use additional records to estimate the Holocene-present MOT difference. We posit that this is the most objective method to report MOT, since the results are insensitive to the method of fractionation correction. The final reported Taylor Glacier MOT data are a combination of the four described firn correction scenarios. Because some methods of corrections yield greater error for replicate samples, we combine scenarios weighted by the inverse of the square error (see Table S4a). In our Monte Carlo simulations, we combine the four correction scenarios, with the number of simulations proportional to their inverse square error. The total reported error is the combined error from these simulations and the estimated error for the Early Holocene – present MOT difference (see Table S4b).

We use the WAIS Divide (Bereiter et al., 2018) and EDC (Baggenstos et al., 2019) Holocene record to estimate the MOT difference between the Early Holocene and the preindustrial. The records show stable MOT over the entirety of the Holocene ($1\sigma = 0.1$°C for EDC, 0.2°C for WAIS Divide). We thus predict no MOT change between these two intervals, but we estimate the error in this calculation as the standard deviation of the WAIS Divide Holocene measurements. To estimate the preindustrial-to-modern MOT change, we refer to model simulations of ocean heat content over the last 2000 years (Gebbie & Huybers, 2019), which overlap with MOT data from WAIS Divide and EDC. Simulations suggest that MOT during the medieval warm period slightly exceeded modern MOT, because the deep ocean had more time to adjust to surface warming. The WAIS Divide and EDC data covering the medieval warm period indicate that the Early Holocene

MOT was comparable or very slightly warmer than the medieval warm period. We thus suggest that the Early Holocene MOT was comparable to modern MOT and make no adjustments to MOT to compare the LIG and MIS6 data to the present.

4.S4.8 EDC Results

In contrast to the Taylor Glacier results, the choice in method of fractionation corrections does affect the relative MOT change found for the EDC data. This is consistent with the findings of Baggenstos et al. (2019) comparing WAIS Divide and EDC MOT records over the last deglaciation. As shown by Baggenstos et al. (2019), the glacial-interglacial MOT change found for Termination I from the EDC record was 1°C greater than that found for WAIS Divide when the EDC record is corrected for gravitational and thermal, but not kinetic fractionation. However, the glacial-interglacial MOT change found for EDC agreed well with that of WAIS Divide when the EDC record was also corrected for kinetic fractionation.

We find analogous results when comparing the EDC record to that of Taylor Glacier for Termination II. If the MOT proxies are only corrected for gravitational and thermal fractionation, the EDC record shows a greater glacial-interglacial MOT difference compared to Taylor Glacier (Figure S6). However, we find quite good agreement in glacial-interglacial MOT difference between the two records if gravitational, thermal, and HID corrections are applied to the EDC data. We note that the Taylor Glacier and EDC records show slightly different results for MIS6 MOT, with the EDC data showing colder MOT than Taylor Glacier. This result is proxy-dependent: we see excellent agreement between records in MOT from $\delta Kr/N_2$, and relatively poor agreement from $\delta Xe/Kr$ (Figure S7). This difference between proxies merits further investigation but does not influence the main results of the study.

Consistent with the results of Baggenstos et al. (2019), inclusion of the HID correction makes MOT values unrealistically warm. As such, we take the same approach as described for the Taylor Glacier data and compute the EDC MOT anomaly relative to the early Holocene and then to the present. For consistency, we compare the EDC data for the LIG and MIS6 to EDC MOT from 10.0ka and 11.0ka (Baggenstos et al., 2019). MOT is quite stable over the Holocene, so the choice of reference Holocene MOT data for EDC has a negligible influence on the results but is made for consistency with the period used for reference for the Taylor Glacier record (10.6 ka). As with the Taylor Glacier MOT record, we include the error in estimating the Early Holocene – present MOT change in our total error estimate.

Acknowledgements

Chapter 4, in full, is the reproduction of a manuscript that is currently in review at *Nature Geoscience*: Shackleton, S., Baggenstos, D., Menking, J. A., Dyonisius, M. N., Bereiter, B., Bauska, T. K., Rhodes, R. H., Brook, E. J., Petrenko, V. V., McConnell, J. R., Kellerhals, T., Häberli, M., Schmitt, J., Fischer, H., Severinghaus, J. P. Last Interglacial Peak Mean Ocean Temperature Due to Ocean Circulation Change. In Review at *Nature Geoscience*. I was the primary investigator and author of this work.

This research was supported by NSF grants 1246148 (SIO), 1245821 (OSU) and 1245659 (UR). We thank Kathy Schroeder, Mike Jayred, Peter Sperlich, Isaac Vimont, Jacob Ward, Heidi Roop, Peter Neff, and Andrew Smith for their invaluable field support for this project. Ice Drilling Design and Operations (IDDO) provided drilling support, and the US Antarctic Program provided logistical support for this project. Thanks to Ross Beaudette for lab support at SIO, to Michael Kalk for CO_2 measurements at OSU, and to Monica Arienzo and Nathan Chellman for their heroic operation of the continuous melting system at DRI. The research at University of Bern leading to

these results has received funding from the European Research Council (ERC) under the European Union's Seventh Framework Programme FP7/2007-2013 ERC Grant 226172 (ERC Advanced Grant Modern Approaches to Temperature Reconstructions in polar Ice Cores (MATRICs)) and the Swiss national Science Foundation (200020_172506 (iCEP), 200021_155906 (NOTICE)). The EDC samples were obtained under the framework of EPICA, a joint European Science Foundation/European Commission scientific program funded by the European Union and national contributions from Belgium, Denmark, France, Germany, Italy, the Netherlands, Norway, Sweden, Switzerland, and the United Kingdom. The main logistic support was provided by IPEV and PNRA at Dome C.

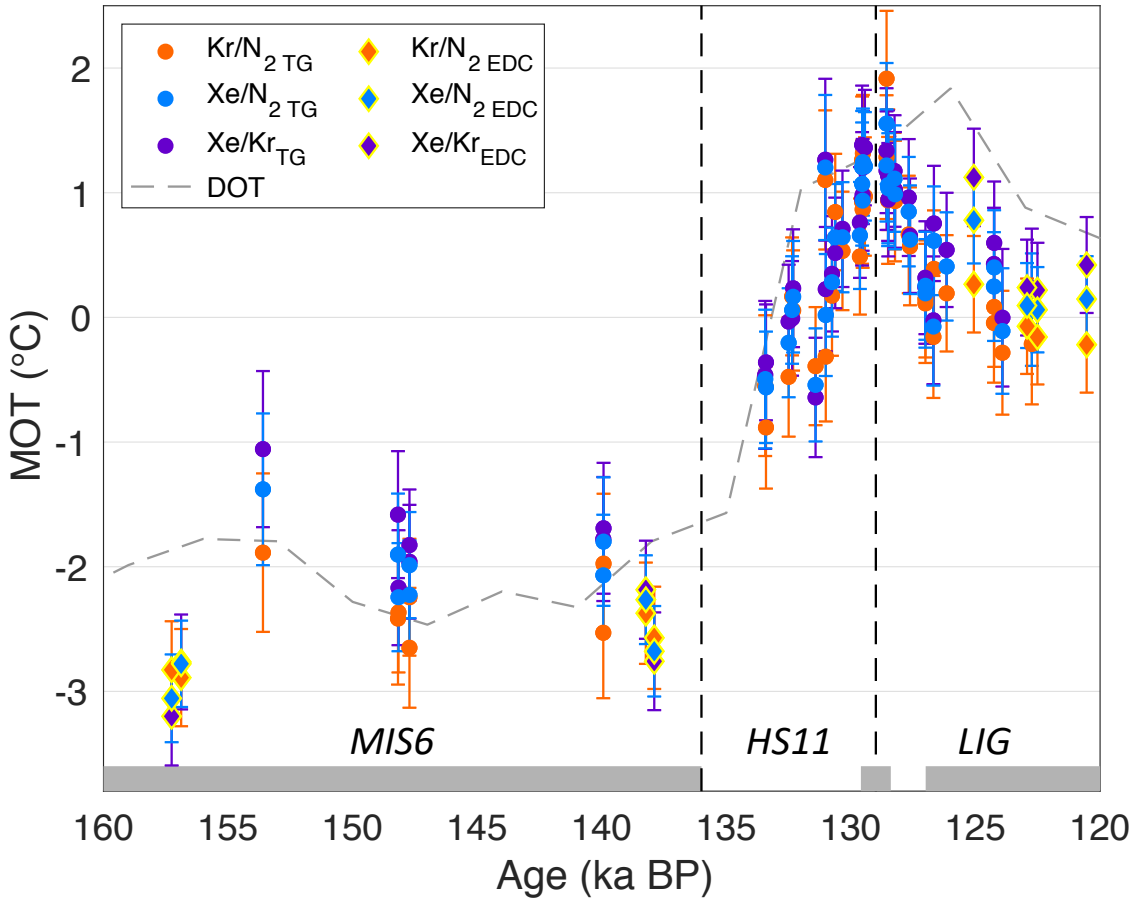

Figure 4.1. Mean ocean temperature (MOT) anomaly from Holocene/modern derived from Kr/N_2, Xe/N_2, and Xe/Kr with 1σ error on the AICC2012 age scale. Vertical dashed lines mark the Marine Isotope Stage 6 (MIS6), Heinrich Stadial 11 (HS11) and Last Interglacial (LIG) intervals. Gray bars indicate the time intervals for which MIS6 MOT (>136 ka), peak MOT (128.9±0.7 ka), and stable LIG MOT (<127 ka) are calculated. Deep ocean temperature from stacked marine sediment records (Shakun et al., 2015) on LR04 (Lisiecki & Raymo, 2005) is shown for reference.

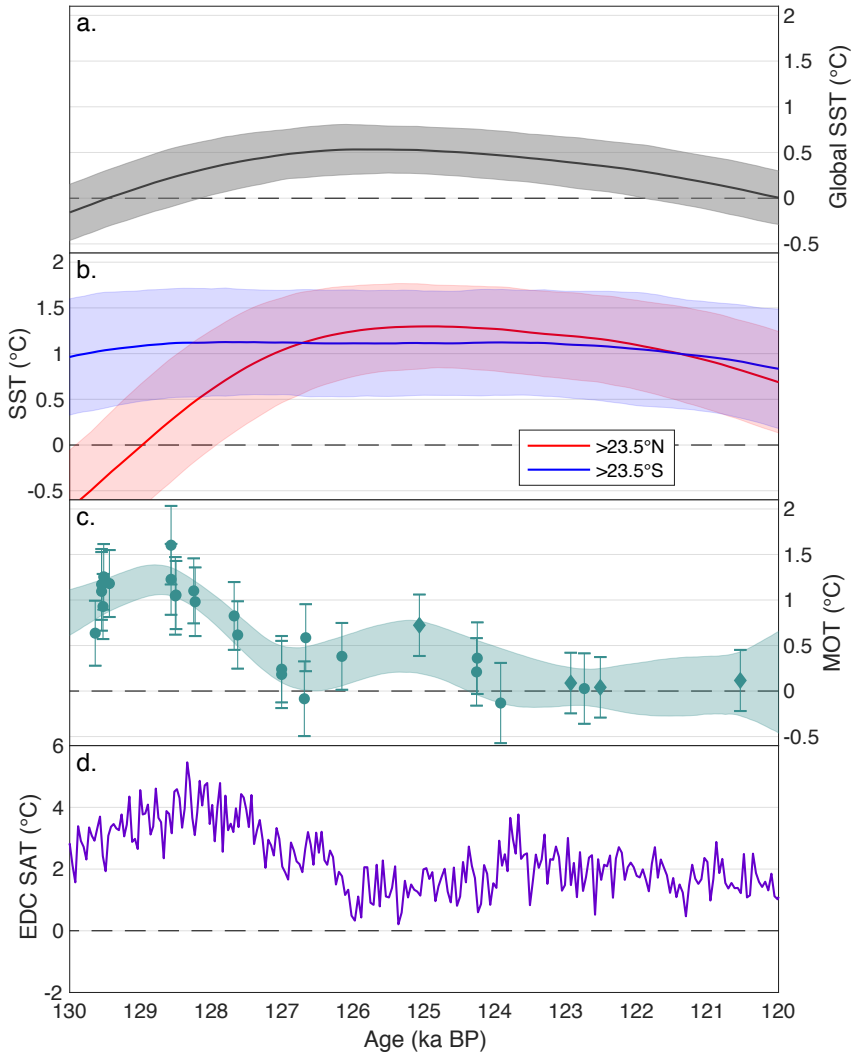

Figure 4.2. Comparison of surface temperature and MOT anomalies during the LIG. a) global and b) extratropical sea surface temperature (SST) anomalies (relative to preindustrial) from the Northern Hemisphere (red) and Southern Hemisphere (blue) from stacked sediment records (Hoffman et al., 2017). Shading shows 2σ confidence interval. c) MOT anomaly on AICC2012 with 1σ error bars (points) and 1σ confidence envelope (shading), based on Monte Carlo splines with a 2500-year cutoff period and bootstrapping. d) EDC surface air temperature anomaly (SAT, Jouzel et al., 2007) on AICC2012. Note that all temperature anomalies (except for EDC SAT) are plotted at the same scale.

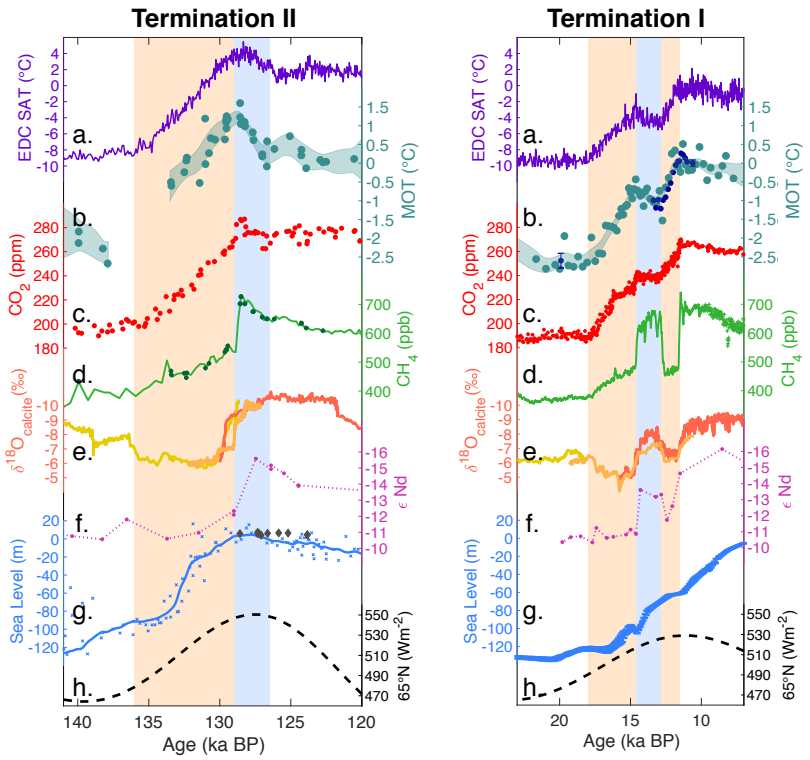

Figure 4.3. Climate records of Terminations I and II. Left panel: Climate records of Termination II. a) EDC surface air temperature (SAT) anomaly relative to modern (Jouzel et al., 2007) on AICC2012 (Bazin et al., 2013) b) MOT anomaly relative to Holocene/modern from this study on AICC2012. Shading indicates 1σ confidence envelope of splined data with a 2500 year cut-off period and bootstrapping c) CO_2 composite record (Bereiter et al., 2015) on AICC2012 d) EDC CH_4 record (Loulergue et al., 2008) on AICC2012. Points show Taylor Glacier CH_4 that coincide with MOT measurements. e) ^{230}Th dated $\delta^{18}O_{calcite}$ records from Sanbao cave (Cheng et al., 2009; Wang et al., 2008); individual Sanbao speleothems are shown with different colors. f) North Atlantic ϵNd (Deaney et al., 2017) on core-specific age scale. We note that the benthic $\delta^{18}O$ record presented by Deaney et al., (2017) suggests a much more abrupt shift in circulation than can be inferred from their ϵNd record. g) In light blue, Red Sea Level anomaly corrected for isostatic effects (Grant et al., 2014) on core-specific age scale. Crosses show individual points, line shows most probable sea level curve. Gray diamonds show isostatically corrected coral reef sea level records (Dutton et al., 2015) h) Summer solstice insolation at 65°N. Right panel: Climate records of Termination I with differences from left panel as follows: b) In turquoise, WAIS Divide MOT (Bereiter, Shackleton, et al., 2018) on WD2014 (Buizert, Cuffey, et al., 2015) relative to Holocene/modern and 1σ confidence envelope of splined data with a 2500 year cut-off period. In dark blue, Taylor Glacier MOT relative to Holocene/modern over the Younger Dryas (Shackleton et al., 2019), LGM, and Holocene on WD2014. Error bars show the spread (1σ) of the five replicate samples from the Holocene and LGM measured at SIO for this study (supplement) c) CO_2 composite record on WD2014 d) CH_4 record (Buizert, Adrian, et al., 2015) on WD2014 e) Dongge cave (Dykoski et al., 2005) (red) and Hulu cave (Wang et al., 2001) (orange and yellow) ^{230}Th dated $\delta^{18}O_{calcite}$ records. f) North Atlantic ϵNd (Roberts et al., 2010) on core-specific age scale g) eustatic sea level with 1σ error (Lambeck et al., 2014) from radiocarbon or uranium-series dated coral and sediment records. Orange panels indicate times when AMOC was in a weakened mode and blue panels show periods of strong AMOC and MOT/Antarctic cooling.

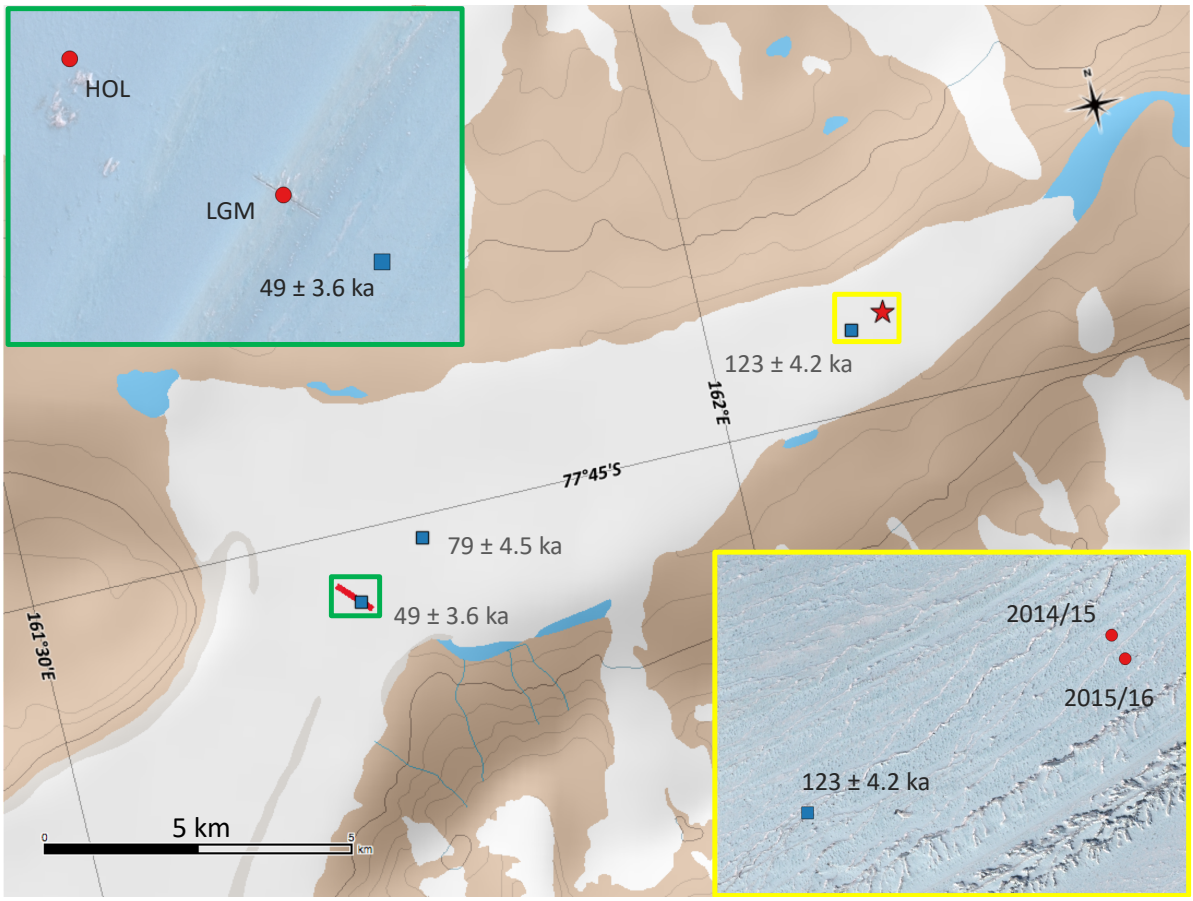

Figure 4.S1. Map of the Taylor Glacier blue ice area. The red star shows the sampling location for the Last Interglacial (LIG) cores, and the red line indicates the location of the across-flow transect (Baggenstos et al., 2017), where Blue Ice Drill (BID) samples from the Holocene (HOL) and Last Glacial Maximum (LGM) were drilled (Baggenstos et al., 2017). Blue squares mark locations of krypton-81 dated ice samples along with their stratigraphic ages and uncertainties (Buizert et al., 2014). Top left inset shows a close-up satellite image of the Main Transect and BID locations of the HOL and LGM cores (red dots) measured in this study. Bottom right inset shows a close-up of the sampling sites for the two LIG BID cores analyzed in this study. Base maps were compiled by the Norwegian Polar Institute, distributed in the Quantarctica package, and provided by the SCAR Antarctic Digital Database. Satellite imagery provided by the Polar Geospatial Center.

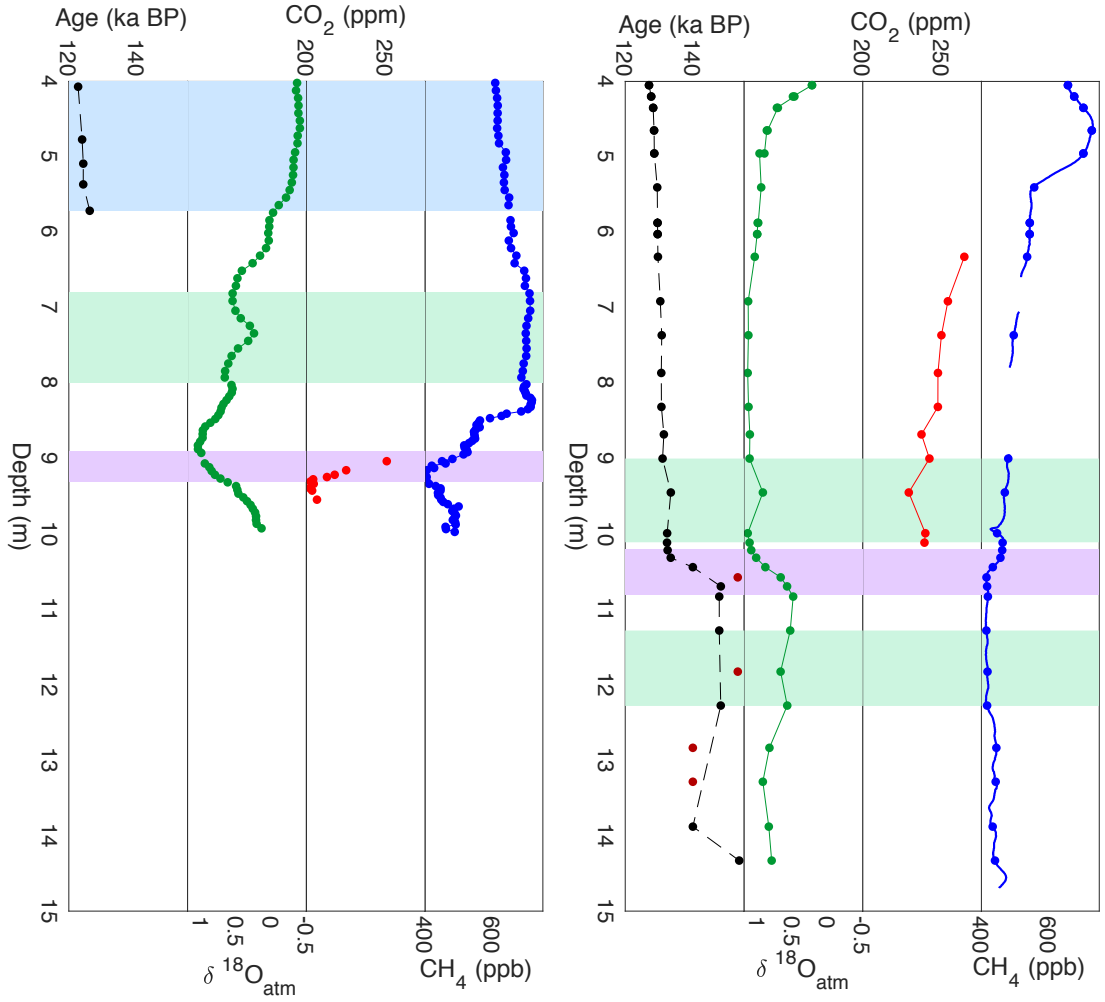

Figure 4.S2. Depth versus age (black), $\delta^{18}O_{atm}$ (green), CO_2 (red), and CH_4 (blue) for the 2014/2015 (left panels) and 2015/2016 (right panels) BID cores. Only ~1.75 meters (blue shading) of the 2014/2015 core was used for this MOT study. For the 2015/2016 core, the blue line shows the continuous CH_4 data and blue circles show depth intervals where MOT samples were taken. In the age panel, the red dots show samples that were rejected based on age constraint thresholds. In the regions highlighted with green, we observe likely artifacts in $\delta^{18}O_{atm}$ reversals and inflections that were not present in the reference record (Extier et al., 2018) suggesting folding. In the regions highlighted with purple we observe significant change in age within a very narrow depth range, suggesting non-uniform thinning.

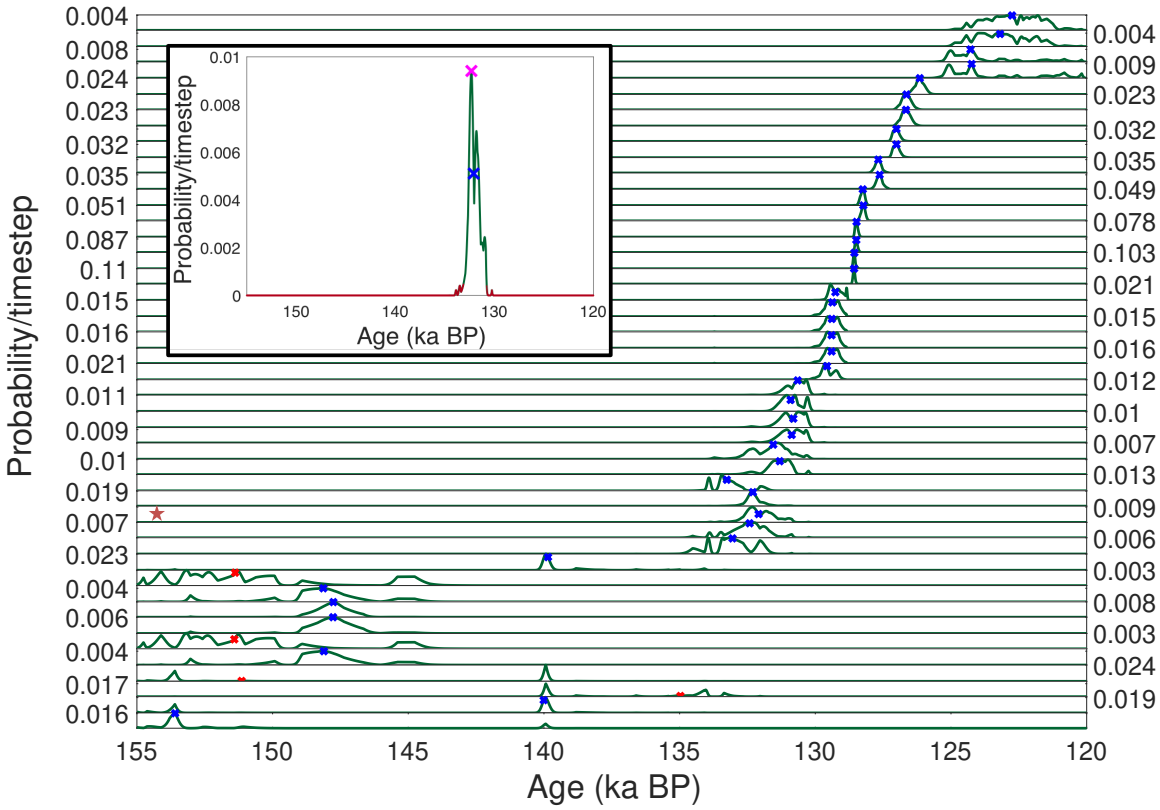

Figure 4.S3. Age probability distributions for the 45 MOT samples. Samples are shown in ascending order with respect to depth (i.e. the top row in the plot is closest to the glacier surface). The first five samples come from the 2014/2015 core, and the rest from the 2015/2016 core. Each probability distribution is normalized so that the area under the curve sums to 1. The green curve shows the probability that a sample is the age at each 10-year timestep between 120 and 155 ka BP. The y-axis tick-label indicates the maximum probability/timestep value for each distribution. The blue and red Xs show the median age of the sample. Samples that were included in the record have blue Xs while those that were rejected based on age uncertainty have Xs in red. The red star marks the 32nd MOT sample. Inset shows the probability distribution for the 32nd MOT sample highlighted as an example. Green shows the probability of the age at each 10-year timestep, and red shows the probability range that is not included in the Monte Carlo simulations. The blue X shows the median age of the distribution, while the magenta X shows the most probable age. The difference between the most probable age and the median age for this particular sample is 470 years. This sample is shown because it is one of the wider probability distributions.

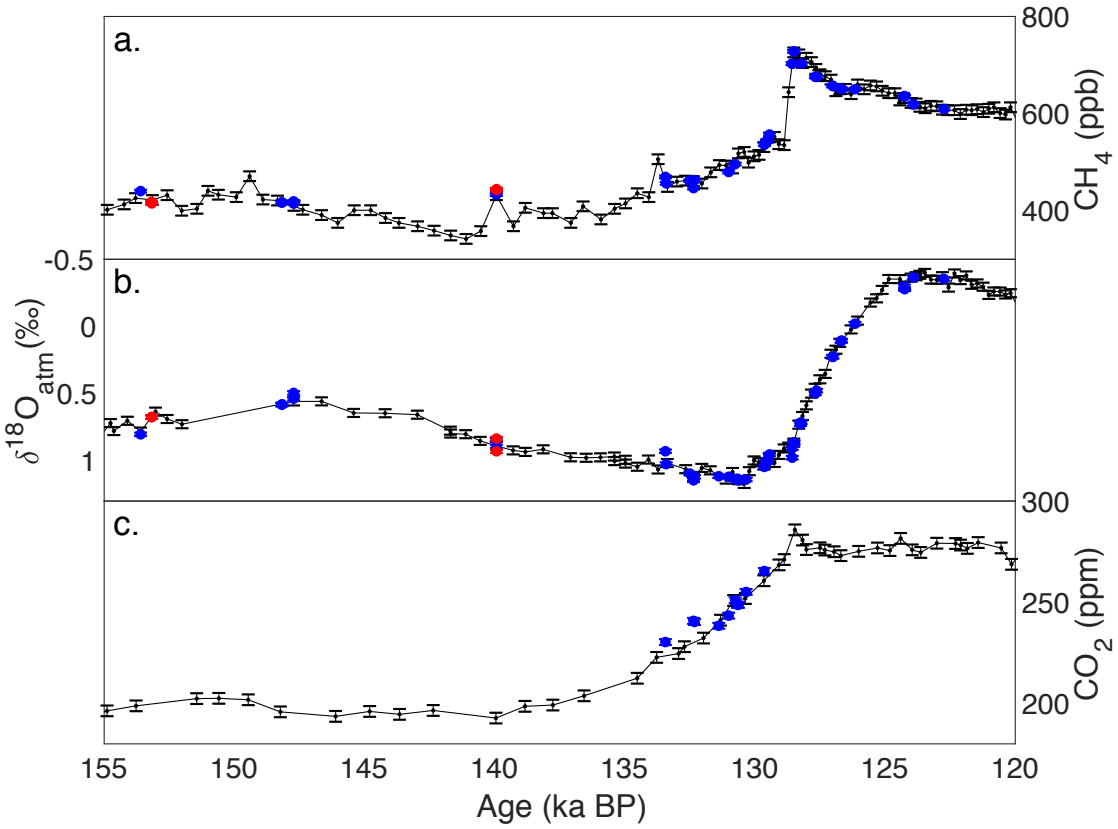

Figure 4.S4. In black, reference records of a) CH_4 (Loulergue et al., 2008), b) $\delta^{18}O_{atm}$ (Extier et al., 2018), and c) CO_2 (Schneider et al., 2013), along with Taylor Glacier measurements (blue and red) of these gases plotted at their most probable age. Samples in blue have acceptably small age uncertainties (41 samples), while those in red (4 samples) are rejected because of their large age uncertainties.

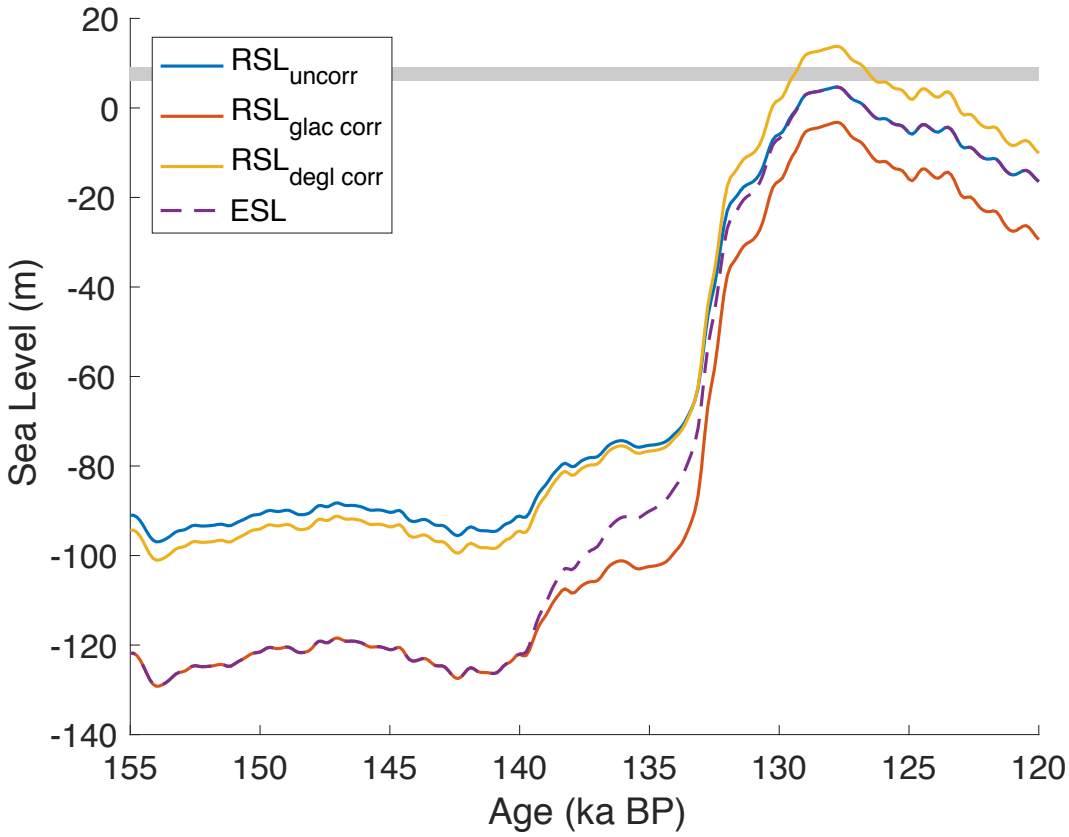

Figure 4.S5. Red Sea Level curves with and without isostatic corrections. Purple dashed line shows the sea level curve used in the box model to calculate MOT for this study. Gray bar shows the possible range of the LIG sea level highstand (Kopp et al., 2009).

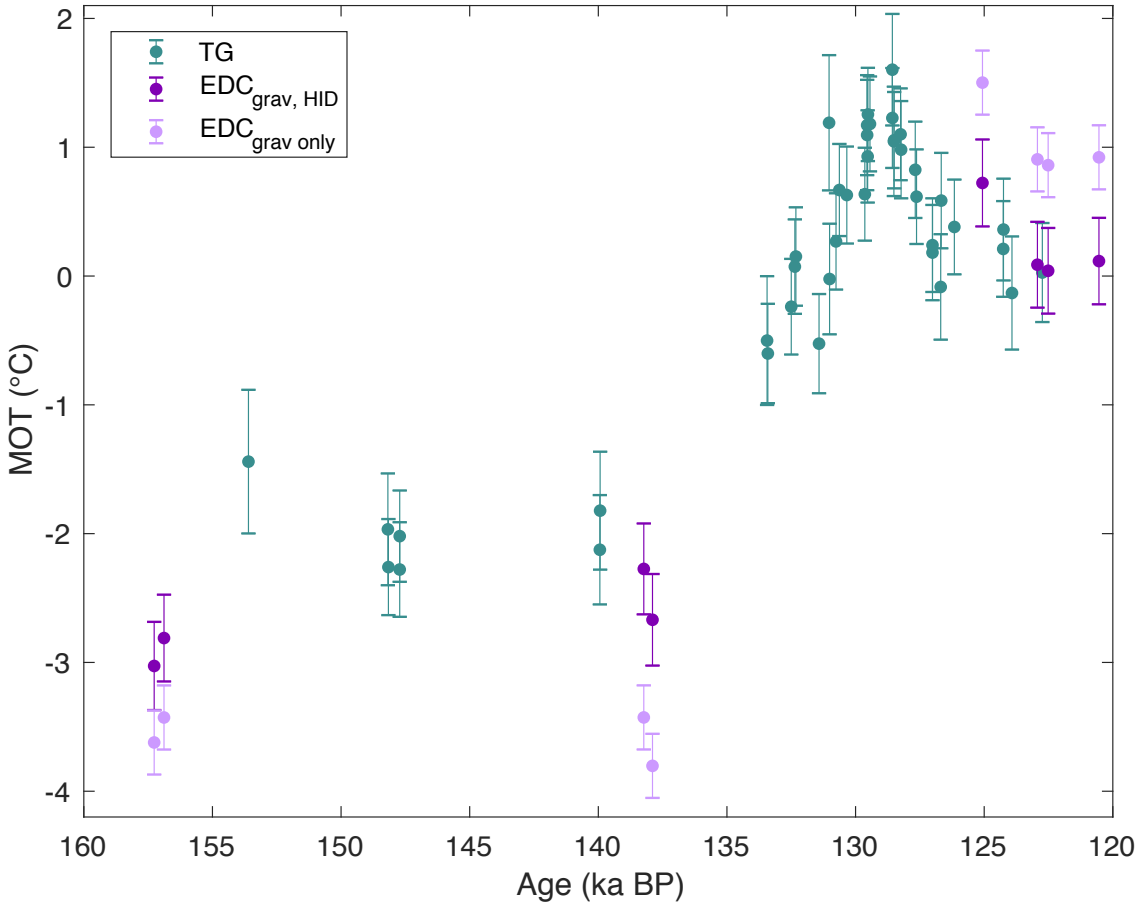

Figure 4.S6. Taylor Glacier and EDC MOT data. Green points indicate data from Taylor Glacier and purple points mark EDC data. Dark purple points show the EDC MOT solutions including the HID correction. Light purple points show the EDC MOT data without the HID correction. All data are reported relative to the Early Holocene.

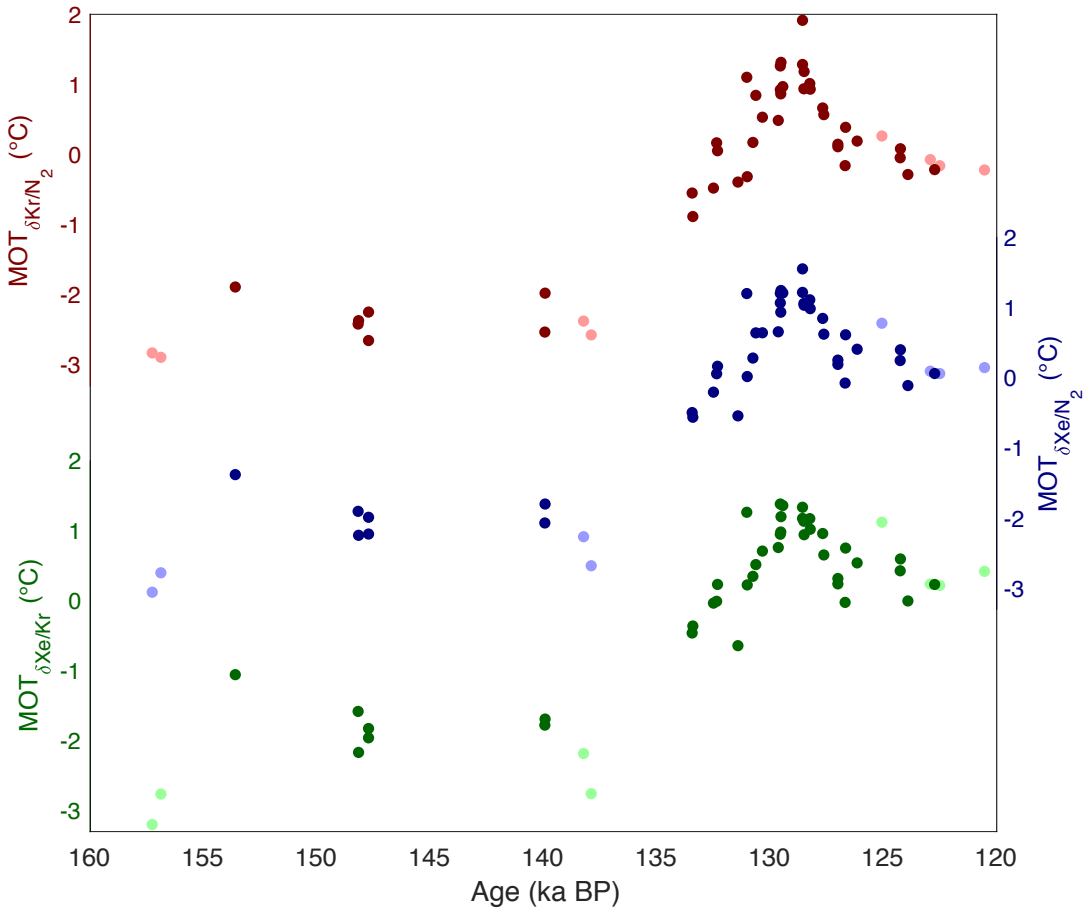

Figure 4.S7. Taylor Glacier and EDC MOT results from $\delta Kr/N_2$ (red), $\delta Xe/N_2$ (blue), and $\delta Xe/Kr$ (green). Taylor Glacier data is shown in darker colors and EDC (with HID correction) is shown in lighter colors. MOT is reported relative to Early Holocene results for the respective Taylor Glacier and EDC records.

Table 4.S1. Laboratory intercomparison results for the Holocene (HOL) and LGM samples made at SIO and Bern. Reported values are the mean and standard deviation of the 5 replicate samples of each core at each institution. Delta values are reported relative to a modern air standard. Reported isotope ratios are normalized per mass unit.

SIO and Bern Holocene and LGM intercomparison results

		$\delta Kr/N_2$	**$\delta Xe/N_2$**	**$\delta Xe/Kr$**	**$\delta^{40/36}Ar/4$**	**$\delta^{40/38}Ar/2$**	**$\delta^{86/82}Kr/4$**	**$\delta^{86/84}Kr/2$**	**$\delta^{15}N$**
HOL	mean	**13.35**	**24.37**	**10.88**	**0.241**	**0.238**	**0.221**	**0.226**	**0.240**
SIO	stdev	0.15	0.29	0.16	0.002	0.002	0.005	0.009	0.003
HOL	mean	**13.43**	**24.44**	**10.89**	**0.239**	**0.236**	**0.224**	**0.222**	**0.237**
Bern	stdev	0.05	0.12	0.09	0.001	0.003	0.003	0.004	0.007
LGM	mean	**2.31**	**3.07**	**0.76**	**0.069**	**0.066**	**0.051**	**0.052**	**0.065**
SIO	stdev	0.16	0.23	0.23	0.002	0.004	0.003	0.005	0.002
LGM	mean	**2.45**	**3.28**	**0.84**	**0.067**	**0.066**	**0.056**	**0.053**	**0.056**
Bern	stdev	0.06	0.15	0.11	0.001	0.002	0.002	0.006	0.008

Table 4.S2. List of relevant Taylor Glacier measurements for this study along with analytical uncertainties (1σ, pooled standard deviation), number of samples on which these measurements were made, and the application of these measurements in this study. The analytical uncertainties

Taylor Glacier Gas Measurements

Gas	1σ err	Unit	# Samples	Application
$\delta Kr/N_2$	0.153	per mil	45	MOT reconstruction
$\delta Xe/N_2$	0.259	per mil	45	MOT reconstruction
δXe/Kr	0.196	per mil	45	MOT reconstruction
$\delta^{40/36}Ar$	0.007	per mil	45	Fractionation corrections
$\delta^{40/38}Ar$	0.006	per mil	45	Fractionation corrections
$\delta^{86/84}Kr$	0.015	per mil	45	Fractionation corrections
$\delta^{86/83}Kr$	0.022	per mil	45	Fractionation corrections
$\delta^{86/82}Kr$	0.015	per mil	45	Fractionation corrections
$\delta^{15}N$	0.003	per mil	45	Fractionation corrections
$\delta^{18}O_{atm}$	0.013	per mil	45	Age model
CH_4 discrete	2.94	ppb	5	Age model
CH_4 continuous	2.80	ppb		Age model
CO_2	1.45	ppm	10	Age model

Table 4.S3. List of relevant EDC measurements for this study along with analytical uncertainties (1σ, pooled standard deviation), number of samples on which these measurements were made, and the application of these measurements in this study. The analytical uncertainties reported for the noble gas measurements are from the standard deviation of 'standard air' measurements made at the University of Bern.

EDC Gas Measurements

Gas	**1σ err**	**Unit**	**# Samples**	**Application**
$\delta Kr/N_2$	0.107	per mil	8	MOT reconstruction
$\delta Xe/N_2$	0.212	per mil	8	MOT reconstruction
δXe/Kr	0.135	per mil	8	MOT reconstruction
$\delta^{40/36}Ar$	0.010	per mil	8	Fractionation corrections
$\delta^{86/84}Kr$	0.012	per mil	8	Fractionation corrections
$\delta^{136/129}Xe$	0.036	per mil	8	Fractionation corrections
$\delta^{134/129}Xe$	0.052	per mil	8	Fractionation corrections
$\delta^{132/129}Xe$	0.017	per mil	8	Fractionation corrections

Table 4.S4. a.) Taylor Glacier MOT anomaly (°C) for each of the least-squares method of firn corrections. For each method, an X indicates if a source of fractionation is included in the least-squares system. Table shows the results for MOT within the peak interval (LIG, 128.9±0.7 ka) and coldest (MIS6, 136-160 ka) measurements in this reconstruction compared to those of the Holocene and LGM made at SIO for each least-squares method. Values shown are for the combined reconstructions of $\delta Kr/N_2$, $\delta Xe/N_2$ and $\delta Xe/Kr$. Error is estimated from the pooled standard deviation of the combined MOT reconstructions for the five Holocene and five LGM samples made at SIO. b.) MOT anomaly relative to Early Holocene MOT values. Bottom row shows the results for a combination of the four fractionation corrections. While the absolute MOT results differ significantly between methods of corrections, MOT results relative to the Holocene are in good agreement. The error is the combined error from the pooled standard deviation results and the uncertainty in the Holocene to present MOT difference.

a. Taylor Glacier absolute MOT (°C)

grav	therm	kin	HOL	LGM	LIG	MIS6	1σ err
X			-0.6	-3.1	0.4	-2.6	0.2
X	X		-0.1	-2.8	1.0	-2.2	0.1
X		X	0.6	-2.1	1.8	-1.2	0.3
X	X	X	1.0	-1.3	2.0	-0.6	0.4

b. Taylor Glacier MOT relative to Holocene/present (°C)

grav	therm	kin	HOL	LGM	LIG	MIS6	1σ err
X			-	-2.6	1.0	-2.0	0.3
X	X		-	-2.7	1.1	-2.0	0.3
X		X	-	-2.7	1.2	-1.8	0.4
X	X	X	-	-2.3	1.0	-1.2	0.5
combined scenario			-	-2.6	1.1	-2.0	0.3

References

Aarons, S. M., Aciego, S. M., Mcconnell, J. R., Delmonte, B., & Baccolo, G. (2019). Dust transport to the Taylor Glacier, Antarctica during the last interglacial. *Geophysical Research Letters*, *46*, 2261–2270. https://doi.org/10.1029/2018GL081887

Aciego, S. M., Cuffey, K. M., Kavanaugh, J. L., Morse, D. L., & Severinghaus, J. P. (2007). Pleistocene ice and paleo-strain rates at Taylor Glacier, Antarctica. *Quaternary Research*, *68*, 303–313. https://doi.org/10.1016/j.yqres.2007.07.013

Ahn, J., Brook, E. J., & Howell, K. (2009). A high-precision method for measurement of paleoatmospheric CO2 in small polar ice samples. *Journal of Glaciology*, *55*(191), 499–506. https://doi.org/https://doi.org/10.3189/002214309788816731

Ahn, J., Brook, E. J., Mitchell, L., Rosen, J., Mcconnell, J. R., Taylor, K., Etheridge, D., & Rubino, M. (2012). Atmospheric CO2 over the last 1000 years : A high-resolution record from the West Antarctic Ice Sheet (WAIS) Divide ice core. *Global Biogeochemical Cycles*, *26*(2). https://doi.org/10.1029/2011GB004247

Baggenstos, D. (2015). *Taylor Glacier as an archive of ancient ice for large-volume samples: Chronology, gases, dust, and climate*. University of California, San Diego.

Baggenstos, D., Bauska, T. K., Severinghaus, J. P., Lee, J. E., Schaefer, H., Buizert, C., Brook, E. J., Shackleton, S., & Petrenko, V. V. (2017). Atmospheric gas records from Taylor Glacier, Antarctica, reveal ancient ice with ages spanning the entire last glacial cycle. *Climate of the Past*, *13*(7), 943–958. https://doi.org/10.5194/cp-13-943-2017

Baggenstos, D., Häberli, M., Schmitt, J., Shackleton, S. A., Birner, B., Severinghaus, J. P., Kellerhals, T., & Fischer, H. (2019). The Earth's radiative imbalance from the Last Glacial Maximum to the present. *Proceedings of the National Academy of Sciences*, *116*(30), 14881–14886. https://doi.org/10.1073/pnas.1905447116

Barker, S., Knorr, G., Edwards, R. L., Parrenin, F., Putnam, A. E., Skinner, L. C., Wolff, E., & Ziegler, M. (2011). 800,000 Years of Abrupt Climate Variability. *Science*, *334*, 347–352. https://doi.org/10.1126/science.1203580

Bauska, T. K., Baggenstos, D., Brook, E. J., Mix, A. C., Marcott, S. A., Petrenko, V. V, Schaefer, H., Severinghaus, J. P., & Lee, J. E. (2016). Carbon isotopes characterize rapid changes in atmospheric carbon dioxide during the last deglaciation. *Proceedings of the National Academy of Sciences*, *113*(13), 3465–3470. https://doi.org/10.1073/pnas.1513868113

Bazin, L., Landais, A., Lemieux-Dudon, B., Toye Mahamadou, K. H., Veres, D., Parrenin, F., Martinerie, P., Ritz, C., Capron, E., Lipenkov, V. Y., Loutre, M.-F., Raynaud, D., Vinther, B. M., Svensson, A. M., Rasmussen, S. O., Severi, M., Blunier, T., Leuenberger, M., Fischer, H., et al. (2013). An optimized multi-proxy, multi-site Antarctic ice and gas orbital chronology (AICC2012): 120-800 ka. *Climate of the Past*, *9*, 1715–1731.

https://doi.org/10.5194/cp-9-1715-2013

Bender, M. L., Barnett, B., Dreyfus, G., Jouzel, J., & Porcelli, D. (2008). The contemporary degassing rate of 40Ar from the solid Earth. *Proceedings of the National Academy of Sciences*, *105*(24), 8232–8237. https://doi.org/https://doi.org/10.1073/pnas.0711679105

Bereiter, B., Lüthi, D., Siegrist, M., Schüpbach, S., & Stocker, T. F. (2012). Mode change of millennial CO2 variability during the last glacial cycle associated with a bipolar marine carbon seesaw. *Proceedings of the National Academy of Sciences*, *109*(25), 9755–9760. https://doi.org/10.1073/pnas.1204069109

Bereiter, B., Eggleston, S., Schmitt, J., Nehrbass-ahles, C., Stocker, T. F., Fischer, H., Kipfstuhl, S., & Chappellaz, J. (2015). Revision of the EPICA Dome C CO2 record from 800 to 600 kyr before present. *Geophysical Research Letters*, *47*, 542–549. https://doi.org/10.1002/2014GL061957

Bereiter, B., Shackleton, S., Baggenstos, D., Kawamura, K., & Severinghaus, J. (2018). Mean global ocean temperatures during the last glacial transition. *Nature*, *553*(7686), 39–44. https://doi.org/10.1038/nature25152

Bereiter, B., Kawamura, K., & Severinghaus, J. P. (2018). New methods for measuring atmospheric heavy noble gas isotope and elemental ratios in ice core samples. *Rapid Communications in Mass Spectrometry*, *32*(10), 801–814. https://doi.org/10.1002/rcm.8099

Bintanja, R. (1999). On the glaciological, meteorological, and climatological significance of Antarctic blue ice areas. *Reviews of Geophysics*, *37*(3), 337–359.

Birner, B., Buizert, C., Wagner, T. J. W., & Severinghaus, J. P. (2018). The influence of layering and barometric pumping on firn air transport in a 2D model. *The Cryosphere*, *12*, 2021–2037. https://doi.org//10.5194/tc-12-2021-2018

Blunier, T., Spahni, R., Barnola, J., Chappellaz, J., Loulergue, L., Schwander, J., & Cedex, H. (2007). Synchronization of ice core records via atmospheric gases. *Climate of the Past*, *3*, 325–330. https://doi.org/10.5194/cp-3-325-2007

Broecker, S. (1998). Paleocean circulation during the Last Deglaciation: A bipolar seesaw? *Paleoceanography*, *13*(2), 119–121. https://doi.org/10.1029/97PA03707

Buizert, C., & Severinghaus, J. P. (2016). Dispersion in deep polar firn driven by synoptic-scale surface pressure variability. *The Cryosphere*, *10*, 2099–2111. https://doi.org/10.5194/tc-10-2099-2016

Buizert, C., Baggenstos, D., Jiang, W., Purtschert, R., Petrenko, V. V, Lu, Z.-T., Muller, P., Kuhl, T., Lee, J., Severinghaus, J. P., & Brook, E. J. (2014). Radiometric 81Kr dating identifies 120,000-year-old ice at Taylor Glacier, Antarctica. *Proceedings of the National Academy*

of Sciences, *111*(19), 6876–6881. https://doi.org/10.1073/pnas.1320329111

Buizert, C., Adrian, B., Ahn, J., Albert, M., Alley, R. B., Baggenstos, D., Bauska, T. K., Bay, R. C., Bencivengo, B. B., Bentley, C. R., Brook, E. J., Chellman, N. J., Clow, G. D., Cole-Dai, J., Conway, H., Cravens, E., Cuffey, K. M., Dunbar, N. W., Edwards, J. S., et al. (2015). Precise interpolar phasing of abrupt climate change during the last ice age. *Nature*, *520*(7549), 661–665. https://doi.org/10.1038/nature14401

Buizert, C., Cuffey, K. M., Severinghaus, J. P., Baggenstos, D., Fudge, T. J., Steig, E. J., Markle, B. R., Winstrup, M., Rhodes, R. H., Brook, E. J., Sowers, T. A., Clow, G. D., Cheng, H., Edwards, R. L., Sigl, M., McConnell, J. R., & Taylor, K. C. (2015). The WAIS-Divide deep ice core WD2014 chronology – Part 1 : Methane synchronization (68 – 31 ka BP) and the gas age-ice age difference. *Climate of the Past*, *11*, 153. https://doi.org/10.5194/cp-11-153-2015

Capron, E., Govin, A., Stone, E. J., Mulitza, S., Otto-Bliesner, B., Rasmussen, T. L., Sime, L. C., Waelbroeck, C., & Wolff, E. W. (2014). Temporal and spatial structure of multi-millennial temperature changes at high latitudes during the Last Interglacial. *Quaternary Science Reviews*, *103*, 116–133. https://doi.org/10.1016/j.quascirev.2014.08.018

Cheng, H., Edwards, R. L., Broecker, W. S., Denton, G. H., Kong, X., Wang, Y., Zhang, R., & Wang, X. (2009). Ice Age Terminations. *Science*, *326*(5950), 248–252. https://doi.org/10.1126/science.1177840

Craig, H., Horibe, Y., & T., S. (1988). Gravitational Seperation of Gases and Isotopes in Polar Ice Caps. *Science*, *242*(4886), 1675–1678. https://doi.org/10.1126/science.242.4886.1675

Deaney, E. L., Barker, S., & Flierdt, T. Van De. (2017). Timing and nature of AMOC recovery across Termination 2 and magnitude of deglacial CO2 change. *Nature Communications*, *8*, 1–10. https://doi.org/10.1038/ncomms14595

Dokken, T. M., Nisancioglu, K. H., Li, C., Battisti, D. S., & Kissel, C. (2014). Dansgaard-Oeschger cycles: Interactions between ocean and sea ice intrinsic to the Nordic seas. *Paleoceanography*, *28*, 491–502. https://doi.org/10.1002/palo.20042

Dutton, A., Webster, J. M., Zwartz, D., & Lambeck, K. (2015). Tropical tales of polar ice: evidence of Last Interglacial polar ice sheet retreat recorded by fossil reefs of the granitic Seychelles islands. *Quaternary Science Reviews*, *107*, 182–196. https://doi.org/10.1016/j.quascirev.2014.10.025

Dykoski, C. A., Edwards, R. L., Cheng, H., Yuan, D., Cai, Y., Zhang, M., Lin, Y., Qing, J., An, Z., & Revenaugh, J. (2005). A high-resolution, absolute-dated Holocene and deglacial Asian monsoon record from Dongge Cave, China. *Earth and Planetary Science Letters*, *233*(1–2), 71–86. https://doi.org/10.1016/j.epsl.2005.01.036

Eggleston, S., Schmitt, J., Bereiter, B., Schneider, R., & Fischer, H. (2016). Evolution of the stable

carbon isotope composition of atmospheric CO2 over the last glacial cycle. *Paleoceanography*, *31*, 434–452. https://doi.org/10.1002/2015PA002874

Elderfield, H., Ferretti, P., Crowhurst, S., Mccave, I. N., Hodell, D., & Piotrowski, A. M. (2012). Evolution of Ocean Temperature and Ice Volume Through the Mid-Pleistocene Climate Transition. *Science*, *337*. https://doi.org/10.1126/science.1221294

Extier, T., Landais, A., Bréant, C., Prié, F., Bazin, L., Dreyfus, G., Roche, D. M., & Leuenberger, M. (2018). On the use of δ18Oatm for ice core dating. *Quaternary Science Reviews*, *185*, 244–257. https://doi.org/10.1016/j.quascirev.2018.02.008

Fischer, H., Meissner, K. J., Mix, A. C., Abram, N. J., Austermann, J., Brovkin, V., Capron, E., Colombaroli, D., Daniau, A., Dyez, K. A., Felis, T., Finkelstein, S. A., Jaccard, S. L., Mcclymont, E. L., Rovere, A., Sutter, J., Wolff, E. W., Affolter, S., Carlson, A. E., et al. (2018). Palaeoclimate constraints on the impact of 2°C anthropogenic warming and beyond. *Nature Geoscience*, *11*, 475–485. https://doi.org/10.1038/s41561-018-0146-0

Forget, G., & Ferreira, D. (2019). Global ocean heat transport dominated by heat export from the tropical Pacific. *Nature Geoscience*, *12*, 351–353. https://doi.org/10.1038/s41561-019-0333-7

Galbraith, E. D., Merlis, T. M., & Palter, J. B. (2016). Destabilization of glacial climate by the radiative impact of Atlantic Meridional Overturning Circulation disruptions. *Geophysical Research Letters*, *43*(15), 8214–8221. https://doi.org/10.1002/2016GL069846

Gebbie, G., & Huybers, P. (2019). The Little Ice Age and 20th-century deep Pacific cooling. *Science*, *363*(6422), 70–74. https://doi.org/10.1126/science.aar8413

Grachev, A., & Severinghaus, J. P. (2003). Laboratory determination of thermal diffusion constants for 29N2/28N2 in air at temperatures from -60 to 0° C for reconstruction of magnitudes of abrupt climate changes using the ice core fossil – air paleothermometer. *Geochimica et Cosmochimica Acta*, *67*(3), 345–360. https://doi.org/10.1016/S0016-7037(02)01115-8

Grant, K. M., Rohling, E. J., Ramsey, C. B., Cheng, H., Edwards, R. L., Florindo, F., Heslop, D., Marra, F., Roberts, A. P., Tamisiea, M. E., & Williams, F. (2014). Sea-level variability over five glacial cycles. *Nature Communications*, *5*(5076), 1–9. https://doi.org/10.1080/08989575.2017.1289316

Hamme, R. C., & Severinghaus, J. P. (2007). Trace gas disequilibria during deep-water formation. *Deep Sea Research*, *54*, 939–950. https://doi.org/10.1016/j.dsr.2007.03.008

Headly, M. A., & Severinghaus, J. P. (2007). A method to measure Kr/N2 ratios in air bubbles trapped in ice cores and its application in reconstructing past mean ocean temperature. *Journal of Geophysical Research*, *112*(19), 1–12. https://doi.org/10.1029/2006JD008317

Hoffman, J. S., Parnell, A. C., & He, F. (2017). Regional and global sea-surface temperatures during the last interglaciation. *Science*, *279*(6322), 276–279. https://doi.org/10.1126/science.aai8464

Jouzel, J., Masson-Delmotte, V., Cattani, O., Dreyfus, G., Falourd, S., Hoffmann, G., Minster, B., Nouet, J., Barnola, J. M., Chappellaz, J., Fischer, H., Gallet, J. C., Johnsen, S., Leuenberger, M., Loulergue, L., Luethi, D., Oerter, H., Parrenin, F., Raisbeck, G., et al. (2007). Orbital and Millennial Antarctic Climate Variability over the Past 800,000 years. *Science*, *317*(5839), 793–796. https://doi.org/10.1126/science.1141038

Kavanaugh, J. L., & Cuffey, K. M. (2009). Dynamics and mass balance of Taylor Glacier, Antarctica: 2. Force balance and longitudinal coupling. *Journal of Geophysical Research*, *114*. https://doi.org/10.1029/2009JF001329

Kawamura, K., Severinghaus, J. P., Albert, M. R., Courville, Z. R., Fahnestock, M. A., Scambos, T., Shields, E., & Shuman, C. A. (2013). Kinetic fractionation of gases by deep air convection in polar firn. *Atmospheric Chemistry and Physics*, *13*, 1–14. https://doi.org/10.5194/acp-13-1-2013

Kolmogorov, A. N. (1950). *Foundations of the Theory of Probability*. New York: Chelsea Publishing Company.

Kopp, R. E., Simons, F. J., Mitrovica, J. X., Maloof, A. C., & Oppenheimer, M. (2009). Probabilistic assessment of sea level during the last interglacial stage. *Nature*, *462*(7275), 863–867. https://doi.org/10.1038/nature08686

Kuhl, T. W., Johnson, J. A., Shturmakov, A. J., Goetz, J. J., Gibson, C. J., & Lebar, D. A. (2014). A new large-diameter ice-core drill: The Blue Ice Drill. *Annals of Glaciology*, *55*(68), 1–6. https://doi.org/10.3189/2014AoG68A009

Kuhlbrodt, T., & Gregory, J. M. (2012). Ocean heat uptake and its consequences for the magnitude of sea level rise and climate change. *Geophysical Research Letters*, *39*, 1–6. https://doi.org/10.1029/2012GL052952

Lambeck, K., Rouby, H., Purcell, A., Sun, Y., & Sambridge, M. (2014). Sea level and global ice volumes from the Last Glacial Maximum to the Holocene. *Proceedings of the National Academy of Sciences*, *111*(43), 15296–15303. https://doi.org/10.1073/pnas.1411762111

Landais, A., Dreyfus, G., Capron, E., Jouzel, J., Roche, D. M., & Prié, F. (2013). Two-phase change in CO2, Antarctic temperature and global climate during Termination II. *Nature Geoscience*, *6*, 1062–1065. https://doi.org/10.1038/ngeo1985

Lisiecki, L. E., & Raymo, M. E. (2005). A Pliocene-Pleistocene stack of 57 globally distributed benthic d18O records. *Paleoceanography*, *20*. https://doi.org/10.1029/2004PA001071

Loulergue, L., Schilt, A., Spahni, R., Masson-Delmotte, V., Blunier, T., Lemieux, B., Barnola, J.-

M., Raynaud, D., Stocker, T. F., & Chappellaz, J. (2008). Orbital and millennial-scale features of atmospheric CH4 over the past 800,000 years. *Nature*, *453*, 383–386. https://doi.org/10.1038/nature06950

Marcott, S. A., Bauska, T. K., Buizert, C., Steig, E. J., Rosen, J. L., Cuffey, K. M., Fudge, T. J., Severinghaus, J. P., Ahn, J., Kalk, M. L., McConnell, J. R., Sowers, T., Taylor, K. C., White, J. W. C., & Brook, E. J. (2014). Centennial-scale changes in the global carbon cycle during the last deglaciation. *Nature*, *514*(7524), 616–619. https://doi.org/10.1038/nature13799

Marino, G., Rohling, E. J., Grant, K. M., Heslop, D., Roberts, A. P., Stanford, J. D., & Yu, J. (2015). Bipolar seesaw control on last interglacial sea level. *Nature*, *522*, 197–201. https://doi.org/10.1038/nature14499

Markle, B. R. (2017). *Climate dynamics revealed in ice cores: advances in techniques, theory ,and interpretation*. University of Washington.

Masson-Delmotte, V., Stenni, B., Blunier, T., Cattani, O., Chappellaz, J., Cheng, H., Dreyfus, G., Edwards, R. L., Falourd, S., Govin, A., Kawamura, K., Johnsen, S. J., Jouzel, J., Landais, A., Lourantou, A., Marshall, G., Minster, B., Mudelsee, M., Pol, K., et al. (2010). Abrupt change of Antarctic moisture origin at the end of Termination II. *Proceedings of the National Academy of Sciences*, *107*(27), 10–13. https://doi.org/10.1073/pnas.0914536107

Menking, J. A., Brook, E. J., Shackleton, S. A., Severinghaus, J. P., Dyonisius, M., Petrenko, V., McConnell, J. R., Rhodes, R. H., Bauska, T. K., Baggenstos, D., Marcott, S., & Barker, S. (2018). Spatial pattern of accumulation at Taylor Dome during the last glacial inception: stratigraphic constraints from Taylor Glacier. *Climate of the Past Discussions*, 1–25. https://doi.org/10.5194/cp-2018-53

Mitchell, L. E., Brook, E. J., Sowers, T., Mcconnell, J. R., & Taylor, K. (2011). Multidecadal variability of atmospheric methane , 1000 – 1800 C . E . *Journal of Geophysical Research*, *116*, 1–16. https://doi.org/10.1029/2010JG001441

Nilsson, J., Jakobsson, M., Borstad, C., Kirchner, N., Björk, G., Pierrehumbert, R. T., & Stranne, C. (2017). Ice-shelf damming in the glacial Arctic Ocean : dynamical regimes of a basin-covering kilometre-thick ice shelf. *The Cryosphere*, *11*, 1745–1765. https://doi.org/https://doi.org/10.5194/tc-11-1745-2017

Otto-Bliesner, B. L., Rosenbloom, N., Stone, E. J., Mckay, N. P., Lunt, D. J., Brady, E. C., & Overpeck, J. T. (2013). How warm was the last interglacial? New model – data comparisons. *Philosophical Transactions of the Royal Society A*, *371*. https://doi.org/http://dx.doi.org/10.1098/rsta.2013.0097

Paolo, F. S., Fricker, H. A., & Padman, L. (2015). Volume loss from Antarctic ice shelves is accelerating. *Science*, *348*(6232), 327–331. https://doi.org/10.1126/science.aaa0940

Pedro, J. B., Jochum, M., Buizert, C., He, F., Barker, S., & Rasmussen, S. O. (2018). Beyond the bipolar seesaw: Toward a process understanding of interhemispheric coupling. *Quaternary Science Reviews*, *192*, 27–46. https://doi.org/10.1016/j.quascirev.2018.05.005

Petersen, S. V, Schrag, D. P., & Clark, P. U. (2013). A new mechanism for Dansgaard-Oeschger cycles. *Paleoceanography*, *28*, 24–30. https://doi.org/10.1029/2012PA002364

Petrenko, V. V, Severinghaus, J. P., Brook, E. J., Reeh, N., & Schaefer, H. (2006). Gas records from the West Greenland ice margin covering the Last Glacial Termination : a horizontal ice core. *Quaternary Science Reviews*, *25*, 865–875. https://doi.org/10.1016/j.quascirev.2005.09.005

Pollard, D., & Deconto, R. M. (2016). Contribution of Antarctica to past and future sea-level rise. *Nature*, *531*(7596), 591–597. https://doi.org/10.1038/nature17145

Pritchard, H. D., Ligtenberg, S. R. M., Fricker, H. A., Vaughan, D. G., Broeke, M. R. Van Den, & Padman, L. (2012). Antarctic ice-sheet loss driven by basal melting of ice shelves. *Nature*, *484*(7395), 502–505. https://doi.org/10.1038/nature10968

Rhodes, R. H., Faın, X., Stowasser, C., Blunier, T., Chappellaz, J., Mcconnell, J. R., Romanini, D., Mitchell, L. E., & Brook, E. J. (2013). Continuous methane measurements from a late Holocene Greenland ice core : Atmospheric and in-situ signals. *Earth and Planetary Science Letters*, *368*, 9–19. https://doi.org/10.1016/j.epsl.2013.02.034

Ritz, S. P., Stocker, T. F., & Severinghaus, J. P. (2011). Noble gases as proxies of mean ocean temperature : sensitivity studies using a climate model of reduced complexity. *Quaternary Science Reviews*, *30*(25–26), 3728–3741. https://doi.org/10.1016/j.quascirev.2011.09.021

Roberts, N. L., Piotrowski, A. M., McManus, J. F., & Keigwin, L. D. (2010). Synchronous Deglacial Overturning and Water Mass Source Changes. *Science*, *327*(5961), 75–78. https://doi.org/10.1126/science.1178068

Schneider, R., Schmitt, J., Köhler, P., Joos, F., & Fischer, H. (2013). A reconstruction of atmospheric carbon dioxide and its stable carbon isotopic composition from the penultimate glacial maximum to the last glacial inception. *Climate of the Past*, *9*(6), 2507–2523. https://doi.org/10.5194/cp-9-2507-2013

Schoof, C. (2007). Ice sheet grounding line dynamics: Steady states, stability, and hysteresis. *Journal of Geophysical Research*, *112*(2007), 1–19. https://doi.org/10.1029/2006JF000664

Schwander, J. (1989). The transformation of snow to ice and the occlusion of gases. In H. Oeschger & C. C. Langway (Eds.), *The Environmental Record in Glaciers and Ice Sheets* (pp. 53–67).

Schwander, J., Stauffer, B., & Sigg, A. (1988). Air mixing in firn and the age of the air at pore close-off. *Annals of Glaciology*, *10*, 141–145.

https://doi.org/10.1017/S0260305500004328

Severinghaus, J. P., & Battle, M. O. (2006). Fractionation of gases in polar ice during bubble close-off: New constraints from firn air Ne, Kr and Xe observations. *Earth and Planetary Science Letters*, *244*(1–2), 474–500. https://doi.org/10.1016/j.epsl.2006.01.032

Severinghaus, J. P., Sowers, T., Brook, E. J., Alley, R. B., & Bender, M. L. (1998). Timing of abrupt climate change at the end of the younger dryas interval from thermally fractionated gases in polar ice. *Nature*, *391*(6663), 141–146. https://doi.org/10.1038/34346

Severinghaus, J. P., Grachev, A., Luz, B., & Caillon, N. (2003). A method for precise measurement of argon 40/36 and krypton/argon ratios in trapped air in polar ice with applications to past firn thickness and abrupt climate change in Greenland and at Siple Dome , Antarctica. *Geochimica et Cosmochimica Acta*, *67*(3), 325–343. https://doi.org/https://doi.org/10.1016/S0016-7037(02)00965-1

Severinghaus, J. P., Severinghaus, J. P., Beaudette, R., & Headly, M. A. (2009). Oxygen-18 of O2 Records the Impact of Abrupt Climate Change on the Terrestrial Biosphere. *Science*, 1431–1434. https://doi.org/10.1126/science.1169473

Severinghaus, J. P., Albert, M. R., Courville, Z. R., Fahnestock, M. A., Kawamura, K., Montzka, S. A., Mühle, J., Scambos, T. A., Shields, E., Shuman, C. A., Suwa, M., Tans, P., & Weiss, R. F. (2010). Deep air convection in the firn at a zero-accumulation site, central Antarctica. *Earth and Planetary Science Letters*, *293*, 359–367. https://doi.org/10.1016/j.epsl.2010.03.003

Shackleton, S., Bereiter, B., Baggenstos, D., Bauska, T. K., Brook, E. J., Marcott, S. A., & Severinghaus, J. P. (2019). Is the noble gas-based rate of ocean warming during the Younger Dryas overestimated? *Geophysical Research Letters*. https://doi.org/doi: 10.1029/2019GL082971

Shakun, J. D., Lea, D. W., Lisiecki, L. E., & Raymo, M. E. (2015). An 800-kyr record of global surface ocean δ 18 O and implications for ice volume-temperature coupling. *Earth and Planetary Science Letters*, *426*, 58–68. https://doi.org/10.1016/j.epsl.2015.05.042

Snyder, C. W. (2016). Evolution of global temperature over the past two million years. *Nature*, *538*(7624), 226–228. https://doi.org/10.1038/nature19798

Steig, E. J., Brook, E. J., White, J. W. C., Sucher, C. M., Bender, M., Lehman, S. J., Morse, D. L., Waddington, E. D., & Clow, G. D. (1998). Synchronous climate changes in Antartica and the North Atlantic. *Science*, *282*(5386), 92–95. https://doi.org/10.1126/science.282.5386.92

Steig, E. J., Morse, D. L., Waddington, E. D., Stuiver, M., Grootes, P. M., Mayewski, P. A., Twickler, M. S., & Whitlow, S. I. (2000). Wisconsinan and Holocene Climate History from an Ice Core at Taylor Dome, Western Ross Embayment, Antarctica. *Geografiska Annaler,*

Series A: Physical Geography, *82*(2–3), 213–235. https://doi.org/10.1111/j.0435-3676.2000.00122.x

Stocker, T. F., & Johnsen, S. J. (2003). A minimum thermodynamic model for the bipolar seesaw. *Paleoceanography*, *18*(4), 1–9. https://doi.org/10.1029/2003PA000920

Sutter, J., Gierz, P., Grosfeld, K., Thoma, M., & Lohmann, G. (2016). Ocean temperature thresholds for Last Interglacial West Antarctic Ice Sheet collapse. *Geophysical Research Letters*, *43*, 2675–2682. https://doi.org/10.1002/2016GL067818.1.

Veres, D., Bazin, L., Landais, A., Toye Mahamadou, K. H., Lemieux-Dudon, B., Parrenin, F., Martinerie, P., Blayo, E., Blunier, T., Capron, E., Chappellaz, J., Rasmussen, S. O., Severi, M., Svensson, A., Vinther, B. M., & Wolff, E. W. (2013). The Antarctic ice core chronology (AICC2012): an optimized for the last 120 thousand years. *Climate of the Past*, *9*, 1733–1748. https://doi.org/10.5194/cp-9-1733-2013

Wang, Y., Cheng, H., Edwards, R. L., An, Z. S., Wu, J. Y., Shen, C. C., & Dorale, J. A. (2001). A high-resolution absolute-dated late pleistocene monsoon record from Hulu Cave, China. *Science*, *294*(5550), 2345–2348. https://doi.org/10.1126/science.1064618

Wang, Y., Cheng, H., Edwards, R. L., Kong, X., Shao, X., Chen, S., Wu, J., Jiang, X., Wang, X., & An, Z. (2008). Millennial- and orbital-scale changes in the East Asian monsoon over the past 224,000 years. *Nature*, *451*(7182), 1090–1093. https://doi.org/10.1038/nature06692

Chapter 5

Millennial-Scale Control of Mean Ocean Temperature During the Last Glacial Inception

5.1. Introduction

Glacial cycles of the late Quaternary are characterized by slow buildup of ice sheets followed by rapid disintegration (Cheng et al., 2016; Emiliani, 1955; Imbrie et al., 1993). Along with ice volume and global temperature changes, ocean circulation changes play an important role in setting glacial versus interglacial climate (Adkins, 2013; Curry & Oppo, 2005; Lynch-Stieglitz et al., 1999). The role of the physical and chemical state of the ocean in setting atmospheric CO_2 has been at the center of most of the proposed mechanisms to explain the ~90-ppm glacial-interglacial difference in atmospheric CO_2 (see Sigman et al., 2010 for review).

While glaciations develop gradually over tens of thousands of years, an abrupt transition occurred at the Marine Isotope Stage (MIS) 5-4 boundary at ~70 ka during the last glacial inception. During this period, roughly half of the interglacial-glacial drawdown of atmospheric CO_2 occurred in four thousand years. Along with atmospheric CO_2 change, the transition brought extensive global cooling, buildup of polar ice sheets, and changes in deep ocean circulation (Adkins, 2013; Bereiter et al., 2012; Cutler et al., 2003; Yu et al., 2016). The mechanisms behind this abrupt change are not fully understood.

Multiple lines of oceanographic evidence (Adkins, 2013; Thornalley et al., 2013; Yu et al., 2016) suggest that the MIS 5-4 transition marks the transition from interglacial to glacial ocean circulation. MIS 4 (like MIS 2) is characterized by very cold temperatures in Greenland and Antarctica and the absence of millennial scale variability. Porewater measurements indicate that the deep ocean was near-freezing during MIS 2 (Adkins et al., 2002), but this constraint is unavailable for MIS 4. While similarities exist between the MIS 4 and MIS 2 intervals, there are notable differences. Northern Hemisphere ice sheets did not extend as far as their limit during MIS 2 (Cutler et al., 2003), but MIS 4 conditions led to greater glacial extent in the Southern Hemisphere, in comparison to MIS 2 (Schaefer et al., 2015). While the transition out of MIS 2 led to full interglacial conditions, the same was not true for MIS 4.

Superposed on the orbitally-forced global cooling leading up to the MIS 5-4 transition are Dansgaard-Oeschger (DO) events 19 (72 ka) and 20 (76 ka), and the associated Antarctic Isotope Maxima (AIM). DO cycles are believed to be linked to changes in the strength of the Atlantic Meridional Overturning Circulation (AMOC) (Barker et al., 2011; Broecker, 1982; Buizert & Schmittner, 2015). The influence of AMOC changes on ocean heat content has been studied through mean ocean temperature (MOT) reconstructions over the last two terminations (Baggenstos et al., 2019; Bereiter, Shackleton, et al., 2018; Shackleton et al., 2019, and Chapter 4 of this thesis). However, the long-term changes in radiative forcing and internal feedbacks over terminations make it difficult to parse the different mechanisms controlling MOT during these intervals. In order to gain better insight into the influence of AMOC variations on MOT, it is necessary to study changes in AMOC and MOT outside of terminations (Baggenstos et al., 2019), and under various forcings (Pedro et al., 2018).

Here we reconstruct MOT from 74 to 59 ka, covering the MIS 5-4 transition, MIS 4, and part of the MIS 4-3 transition. With this record, we seek to answer the following questions:

1. How much of the CO_2 drawdown over the MIS 5-4 transition was due to ocean cooling and increased solubility?
2. How cold/stable were ocean temperatures during MIS 4 relative to MIS 2?
3. How does MOT respond to millennial-scale changes in AMOC?

5.2. Methods

5.2.1 Site Description and Ice Core Measurements

The ice core samples in this study are primarily from Taylor Glacier, Antarctica, a blue ice area located in the McMurdo Dry Valleys. The Taylor Glacier ice core site is located approximately 1 km down-glacier from a previously-established across-flow transect that contains ice from ~ 7 – 50 ka (Baggenstos et al., 2017). While the dip of the ice layers is nearly vertical for the across-flow transect, the layers are approximately horizontal at the location of the ice core used in this study; the core contains ice from ~58 ka near the surface to 74 ka at 20 meters depth (Menking et al., 2018). Ice samples were analyzed for noble gases below 4 m depth, to avoid alteration/contamination due to surface cracks (Baggenstos et al., 2017). A total of 56 samples from Taylor Glacier were measured, including 10 replicate samples for MOT reconstruction between 74 and 59 ka. In addition, four WAIS Divide samples from MIS 4 were measured as an independent check on the Taylor Glacier results. Ice core samples were analyzed for noble gases using the method of Bereiter, Kawamura, et al, (2018).

5.2.2. Taylor Glacier Age Model

We use the ice core age model of (Menking et al., 2018) for our MOT reconstruction. This age model was developed by matching measured variations in CH_4 and $\delta^{18}O_{atm}$ in the Taylor Glacier ice core to preexisting records on the AICC2012 timescale. Tie points were manually selected, and noble gas sample ages were determined from linear interpolation between tie points. Tie point uncertainties are reported relative to AICC2012, and do not include age uncertainty of the AICC2012 chronology itself.

5.2.3. Fractionation Corrections and Box Model Parameterizations

The noble gas ratios measured in ice cores must be corrected for fractionation that occurs within the firn, which alters the noble gas ratios from their atmospheric content (Headly & Severinghaus, 2007). For the Taylor Glacier data, we apply the correction approach of Shackleton et al. (2019), which uses a linear least-squares method to solve for gravitational (Craig et al., 1988) and thermal (Severinghaus et al., 1998) fractionation in the firn. To test the sensitivity of our results to the applied correction method we compare the results between several correction methods (see Appendix). For the WAIS Divide data, we use the correction method of (Bereiter, Shackleton, et al., 2018) to compare the results for the measurements within MIS 4 to the published WAIS Divide MIS 2 record. We employ the box model of (Bereiter, Shackleton, et al., 2018) with parameterizations detailed in Baggenstos et al, (2019), and the RSL record of Grant et al, (2014) to calculate MOT from the fractionation-corrected noble gas ratios.

5.2.4. Error Analysis

Error is assessed by propagating all known uncertainties via Monte Carlo simulations through the entire evaluation routine. This includes the analytical error for the noble gas ratios,

and the isotope ratios used for firn fractionation corrections. Additional uncertainties that we account for with this method include reported tie point uncertainties used in the age model development of the Taylor Glacier ice core (Menking et al., 2018), and temporal and analytical uncertainties in the sea level curve used in the box model. To produce a smoothed estimate of our MOT record (and its uncertainties) we create a splined record for each of the 10,000 Monte Carlo simulations with a 2500 year cut-off period, and data resampling via bootstrapping.

5.3. Results

5.3.1 MIS 5-4 MOT and CO_2

Considering the MOT record during the dramatic drawdown in atmospheric CO_2 (72 - 68 ka, Figure 1), we find that MOT cools in two distinct phases, for a net cooling of 1°C. In the first phase, MOT cools by 0.7±0.2°C over ~1500 years, coincident with Antarctic cooling and Greenland Interstadial 19. In the second phase, MOT stabilizes, then cools gradually by 0.3±0.2°C, reaching a minimum at ~68 ka. Because this ocean cooling coincides with a significant drop in sea level, the increased solubility due to ocean cooling is partially offset by an increase in ocean salinity. The net cooling of 1°C over the MIS 5-4 transition leads to a CO_2 drawdown of 8 ppm, which is a small fraction of the ~40 ppm drawdown that occurs over this interval.

A comparison of the Taylor Glacier records of MOT and CO_2 over the MIS 5-4 transition shows MOT and CO_2 both decrease at the onset of the transition, followed by a stabilization of MOT coincident with a brief (~500 year) stabilization CO_2 (Menking, 2019). Because the CO_2 and MOT records are from the same ice core, there is virtually no uncertainty in the relative timing of these records. After brief stabilization, CO_2 decreases by another ~20 ppm to reach its minimum

during MIS 4. During this time MOT change is minimal; while ocean cooling may explain some portion of the CO_2 drawdown in the early stage of the transition, the MOT and CO_2 trends clearly diverge about halfway through the transition.

5.3.2 MIS 4 versus MIS 2 MOT

We compare the Taylor Glacier MIS 4 (70-60 ka) MOT record to that of MIS 2 (at 19.9 ka) and find that MIS 4 was as cold as MIS 2 (-0.1±0.3°C relative to MIS 2). The WAIS Divide MOT data from MIS 2 and MIS 4 confirms the Taylor Glacier results (+0.2±0.3°C relative to MIS 2, Figure S1). If we use our Taylor Glacier MOT record to decompose the benthic stack (Lisiecki & Raymo, 2005) with the method of Cutler et al. (2003), we find an average MIS 4 sea level of -74 m relative to present from Taylor Glacier (-84 m from WAIS Divide MOT), which is in reasonable agreement with the MIS 4 coral sea level benchmark of -81m (Cutler et al., 2003), and slightly higher than the average MIS 4 sea level input we apply for our box model calculations of MOT (-88m, Grant et al., 2014). We note that applying an adjustment to the sea level record used in our box model to be consistent with the benthic decomposition has a negligible impact on MOT (less than 0.1°C change in calculated MOT). The comparable MIS 4 MOT, but ~60 m higher sea level compared to MIS 2 is consistent with previous findings that most of the interglacial to glacial ocean cooling occurs early in the glaciation, preceding significant ice sheet growth (Cutler et al., 2003; Shakun et al., 2015; Waelbroeck et al., 2002).

5.3.3 MIS 4-3 Transition

While our record does not capture the full transition into MIS 3, we find that there is substantial MOT warming out of MIS 4. By the end of our record at ~59.5 ka, MOT had reached levels comparable to peak MIS 5a MOT at ~72 ka. Because our record does not contain a clear leveling of MOT, it is uncertain if/by how much MIS 3 MOT exceeded levels found at the end

MIS 5a. While our MOT record suggests that MOT cooling observed at the MIS 5-4 transition was fully compensated by MOT warming at the MIS 4-3 transition, changes in some physical and chemical ocean properties, such as the shoaling of the North Atlantic Western Boundary Undercurrent (Thornalley et al., 2013) and the decrease in Southern Ocean and Atlantic $\delta^{13}C$ (Oliver et al., 2010) that occurred at the MIS 5-4 boundary were not fully reversed at the transition into MIS 3.

5.4. Discussion

A close correspondence between MOT, Antarctic temperature, and AMOC strength has been observed for the past two deglaciations but their link, until now, has not been tested outside of these unique intervals of global climate change. The covariation of MOT and Antarctic temperature in this record confirms that this phenomenon is not limited to deglaciations. Because the MIS 5-4 transition occurred during a time of substantial global cooling, the correspondence of Antarctic temperature and MOT is perhaps most striking at the onset of the record, as both increase through Greenland Stadial 20, reaching maxima at ~72 ka, coincident with the abrupt warming at the onset of Greenland Interstadial 19 (Figure 1). It is unclear if we capture the onset of MOT warming in our record, so the observed 0.3±0.2°C of warming should be considered a lower bound on the total warming associated with this interval.

At the onset of the MIS 4-3 transition/Heinrich Stadial 6 (~63-59 ka), we do not see as tight covariation between MOT and Antarctic temperature. Antarctica gradually warms in the final four thousand years of MIS 4, whereas the MOT warming at the end of MIS 4 in our record is more abrupt (Figure 1). As a possible basis for understanding the MIS 4-3 transition, we turn to MOT

records of Heinrich Stadial 1 from WAIS Divide (Bereiter, Shackleton, et al., 2018) and EDC (Baggenstos et al., 2019), which showed warming throughout this interval, concurrent with steady Antarctic warming. However, both records suggested that the rate of MOT warming was not constant and peaked later in the stadial at ~15.5 ka (Baggenstos et al., 2019), after the Heinrich event at 16.2 ka (Rhodes et al., 2015). The resulting changes in atmospheric (Rhodes et al., 2015; Severinghaus et al., 2009; Wang et al., 2001) and oceanic (Anderson et al., 2009) circulation in response to the Heinrich event may have enhanced the rate of MOT warming during Heinrich Stadial 1 (Baggenstos et al., 2019). A similar mechanism may also explain the more rapid MOT warming in the latter half of Heinrich Stadial 6.

However, there are multiple caveats to this hypothesis that must be considered. First, the timing of the Heinrich event within Heinrich Stadial 6 is not well known. While an abrupt increase in methane (with no corresponding Greenland warming) was used to identify the timing of the Heinrich event in Heinrich Stadials 1, 2, 4 and 5, none were found for Heinrich Stadials 3 or 6 (Rhodes et al., 2015). The methane spike is believed to be the result of enhanced rainfall over Southern Hemisphere land masses due to an extreme southward migration of the ITCZ forced by Northern Hemisphere cooling and sea ice formation in response to iceberg discharge (Rhodes et al., 2015). The lack of a methane signal during Heinrich Stadial 6 may suggest that an extreme southward migration of the ITCZ did not occur, perhaps due to the lesser impact of this Heinrich event. Additional support for the smaller imprint of this event comes from the less severe weakening of Asian monsoon intensity that occurred during Heinrich event 6, as compared to 1, 2, 4, and 5, which were all sourced from the Hudson Straight; Heinrich events 6 and 3 are of a different/mixed provenance (Hemming, 2004). These observations suggest that the global changes across Heinrich Stadial 6 were much more muted than Heinrich Stadial 1. We would therefore

predict that the MOT changes across Heinrich Stadial 6 would be less dramatic than Heinrich Stadial 1, which is not the case.

Another noteworthy caveat to this hypothesis comes from the MOT record itself. The MOT data is much lower resolution in late MIS 4, owing to the significant decrease in accumulation for the Taylor Glacier accumulation area during this time (Menking et al., 2018). In a lower resolution record, the potential of a single outlier to alter the overall interpretation of the record greatly increases. For instance, without the MOT data point at ~61 ka, the onset of warming appears to better coincide with Antarctic temperature.

We also note that uncertainties in the age scale of the Taylor Glacier record may contribute to uncertainties in the relative timing of MOT and Antarctic temperature change during the MIS 4-3 transition. There is slight disagreement in the overall trend in the Taylor Glacier CO_2 record compared to the composite CO_2 record on AICC2012 at the end of MIS 4 (Figure 1). In the Taylor Glacier record the rate of CO_2 increase is relatively slow at the onset of MIS 4-3 transition but substantially increases at ~61 ka, whereas other CO_2 records show a more constant CO_2 increase from ~64 ka through the end of MIS 4. This may be indicative of an issue with the synchronization of the Taylor Glacier age scale to AICC2012 for this section of the record. We therefore suggest that the asynchrony of Antarctic and MOT warming at the MIS 4-3 transition may not be robust, and requires a higher resolution record, with better age control to substantiate.

Our MOT record shows a largely symmetric pattern of warming and subsequent cooling during Greenland Stadial 20 and Interstadial 19, suggesting that the cooling during the MIS 5-4 transition was largely related to millennial scale changes in the AMOC, rather than a more permanent ocean cooling. However, MOT (and Antarctic temperature) do not begin warming entering Greenland Stadial 19. Theories about the lack of bipolar seesaw behavior during very cold

periods (such as MIS 4 and MIS 2) have invoked mechanisms related to ice volume extent (Mcmanus et al., 1999) and ocean temperature (Buizert & Schmittner, 2015). While the ice sheet extent during MIS 2 exceeds that of MIS 4, MOT during MIS 2 and MIS 4 show equally cold ocean conditions. This supports the idea that ocean temperature, rather than ice sheet extent, controls AMOC stability within a glacial. However, the transition out of MIS 2 (as opposed to MIS 4) resulted in a termination and a transition of ocean circulation from glacial to interglacial conditions. This suggests that maximum Northern Hemisphere ice sheet extent is required for terminations (Abe-ouchi et al., 2013; Schaefer et al., 2015) and the transition from glacial to interglacial ocean conditions.

5.5 Conclusions

Our record clearly demonstrates that ocean cooling during the MIS 5-4 transition can only explain a small fraction of the ~40 ppm drop in atmospheric CO_2, and that MOT cooling at the MIS 5-4 transition was fully reversed at the MIS 4-3 transition, suggesting no net change in the solubility pump from the end of MIS 5 to the onset of MIS 3. MOT reached full glacial conditions during MIS 4, whereas Northern Hemisphere ice sheets were markedly smaller during MIS 4 than MIS 2. While deep ocean warming and ice sheet disintegration occurred approximately in phase during the last deglaciation, deep ocean cooling outpaced ice sheet growth during the last glacial inception.

Our record provides the first piece of evidence that MOT responds to AMOC changes outside of deglaciations and reflects bipolar seesaw behavior during Greenland Stadial 20 and Interstadial 19. As during MIS 2, MOT was cold and stable during MIS 4; their similarity may suggest that stable glacial ocean conditions occur when the oceans cool below a certain threshold.

However, we cannot confidently claim that MIS 2 and MIS 4 were unique in their coldness until MOT records are available through the entirety of the last glacial.

5.6 Future Work

Invaluable insight into the controls on MOT may be gained from reconstructions of MOT during MIS 5 and MIS 3. The ocean had already cooled by more than 2°C between MIS 5e and the start of our MOT record. Determining when, within MIS 5, most of the interglacial-glacial ocean cooling occurred will provide important insight into the sequence of events that occur during the transition from interglacial into glacial conditions. While our record suggests that the coupling between MOT and AMOC is not limited to terminations, the role of Heinrich events and freshwater forcing on controlling the rate of MOT change could be further explored during Heinrich Stadial 2, 4, or 5, when the timing of the Heinrich event within the stadial is well known. A comparison of MOT over Heinrich Stadials 2, 4, and 5 may be particularly interesting, as the Heinrich events occur in the relatively late, middle, and early stages of these respective stadials. In addition, comparison of DO cycles within MIS 5 and MIS 3 may provide further insight into the mechanisms linking the AMOC, Antarctic temperature, and MOT.

Appendix 5. Influence of Firn Fractionation Correction on MOT Results

To consider the influence of the choice in firn fractionation corrections on MOT results, we compared MOT results for the least squares gravitational and thermal correction, to a

gravitational and kinetic correction, and a purely gravitational correction. We did not consider a least-squares correction for gravitational, thermal and kinetic fractionation because this method was shown to impart significant systematic error and amplify analytical noise (see Chapter 3 of this thesis).

As noted from previous Taylor Glacier reconstructions of MOT (see supporting information of Chapter 4 of this thesis), we find that the method of firn correction strongly influences the absolute MOT anomaly, but has less of an influence on relative MOT change (Figure S1). However, there are several subtle differences between the records that are worth noting, so as to highlight some uncertainties when considering the interpretation of the MOT record in the context of other paleoclimate evidence. While all three of the correction scenarios show MOT warming during Greenland Stadial 20, they vary slightly in the relative timing and magnitude of this MOT change. Another divergence between the corrected records is at ~70 ka. For all three correction scenarios, there is a clear cooling in MOT up to this point, however – the scenarios disagree as to whether there is a stabilization of MOT, or a slight warming, before all three scenarios show further cooling. The coldness of MOT during MIS 4 (compared to MIS 2) also varies slightly between corrections. While the correction scenarios are consistent in the overall MOT trends, it is worth cautioning the overinterpretation of the aforementioned features.

Acknowledgements

Chapter 5 contains unpublished material with the following co-authors: James Menking, Edward Brook, Vasilii Petrenko, Michael Dyonisius, Daniel Baggenstos, and Jeffrey Severinghaus. I was the primary investigator and author of this work.

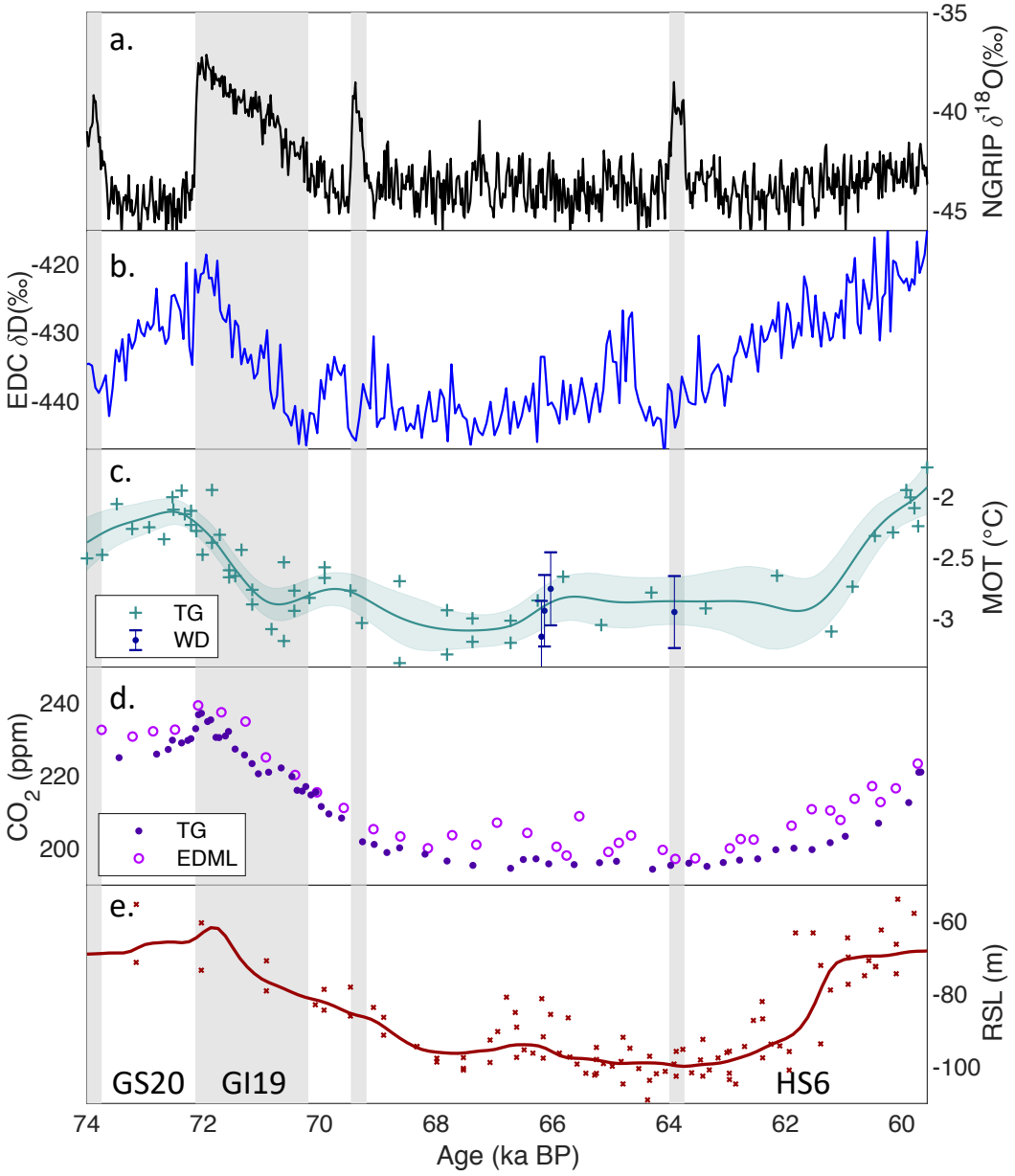

Figure 5.1. Mean ocean temperature (MOT) versus key climate variables. Panel (a) shows NGRIP $\delta^{18}O_{ice}$ (Andersen et al., 2004) on AICC2012 (Veres et al., 2013), (b) EDC δD (Jouzel et al., 2007) (c) MOT data from Taylor Glacier (crosses) on AICC2012 and WAIS Divide (points with 1σ error bars) on WD2014 (Buizert et al., 2015). The turquoise line shows the spline of the Taylor Glacier data with a 2500-year cutoff period and bootstrapping, and shading indicates the 1σ confidence envelope. Panel (d) shows EDML (Bereiter et al., 2015) and Taylor Glacier (Menking, 2019) CO_2 on AICC2012, (e) Red Sea Level record on core-specific age scale (Grant et al., 2014). Gray panels show warm Greenland intervals (interstadials) and white panels indicate cold Greenland intervals (stadials).

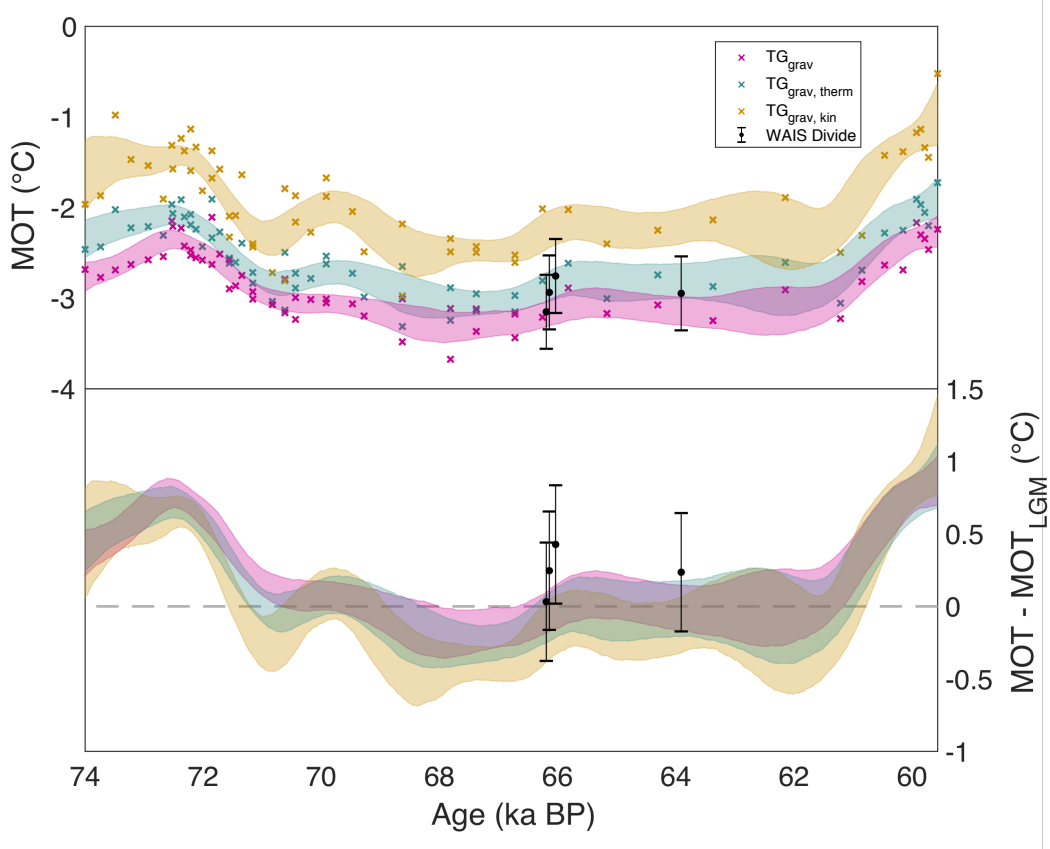

Figure 5.S1. Comparison of Taylor Glacier and WAIS Divide MOT reconstructions from different methods of firn fractionation corrections. Top panel shows the Taylor Glacier results of the absolute MOT anomaly (relative to present) using methods to correct for gravitational (pink), gravitational and thermal (turquoise), and gravitational and kinetic (yellow) fractionation. Shading indicates the 1σ confidence interval of the splined record for each correction method. WAIS Divide results using the fractionation corrections detailed in (Bereiter, Shackleton, et al., 2018) are shown as black points with 1σ error bars. Bottom panel shows the same as the top, but instead of absolute MOT, the results are shown relative to the MIS 2 data for each of the correction methods and each of the ice cores.

References

Abe-ouchi, A., Saito, F., Kawamura, K., Raymo, M. E., Okuno, J., Takahashi, K., & Blatter, H. (2013). Insolation-driven 100,000-year glacial cycles and hysteresis of ice-sheet volume. *Nature*, *500*(7461), 190–193. https://doi.org/10.1038/nature12374

Adkins, J. F. (2013). The role of deep ocean circulation in setting glacial climates. *Paleoceanography*, *28*, 1–23. https://doi.org/10.1002/palo.20046

Adkins, J. F., Mcintyre, K., & Schrag, D. P. (2002). The Salinity, Temperature, and d18O of the Glacial Deep Ocean. *Science*, *298*, 1769–1773. https://doi.org/10.1126/science.1076252

Andersen, K. K., Azuma, N., Barnola, J.-M., Bigler, M., Biscaye, P., Caillon, N., Chappellaz, J., Clausen, H. B., Dahl-Jensen, D., Fischer, H., Flückiger, J., Fritzsche, D., Fujii, Y., Goto-Azuma, K., Grønvold, K., Gundestrup, N. S., Hansson, M., Huber, C., Hvidberg, C. S., et al. (2004). High-resolution record of Northern Hemisphere climate extending into the last interglacial period. *Nature*, *431*(7005), 147–151. https://doi.org/10.1038/nature02805

Anderson, R. F., Ali, S., Bradtmiller, L. I., Nielsen, S. H. H., Fleisher, M. Q., Anderson, B. E., & Burckle, L. H. (2009). Wind-driven upwelling in the southern ocean and the deglacial rise in atmospheric CO2. *Science*, *323*(5920), 1443–1448. https://doi.org/10.1126/science.1167441

Baggenstos, D., Bauska, T. K., Severinghaus, J. P., Lee, J. E., Schaefer, H., Buizert, C., Brook, E. J., Shackleton, S., & Petrenko, V. V. (2017). Atmospheric gas records from Taylor Glacier, Antarctica, reveal ancient ice with ages spanning the entire last glacial cycle. *Climate of the Past*, *13*(7), 943–958. https://doi.org/10.5194/cp-13-943-2017

Baggenstos, D., Häberli, M., Schmitt, J., Shackleton, S. A., Birner, B., Severinghaus, J. P., Kellerhals, T., & Fischer, H. (2019). The Earth's radiative imbalance from the Last Glacial Maximum to the present. *Proceedings of the National Academy of Sciences*, *116*(30), 14881–14886. https://doi.org/10.1073/pnas.1905447116

Barker, S., Knorr, G., Edwards, R. L., Parrenin, F., Putnam, A. E., Skinner, L. C., Wolff, E., & Ziegler, M. (2011). 800,000 Years of Abrupt Climate Variability. *Science*, *334*, 347–352.

Bereiter, B., Lüthi, D., Siegrist, M., Schüpbach, S., & Stocker, T. F. (2012). Mode change of millennial CO2 variability during the last glacial cycle associated with a bipolar marine carbon seesaw. *Proceedings of the National Academy of Sciences*, *109*(25), 9755–9760. https://doi.org/10.1073/pnas.1204069109

Bereiter, B., Eggleston, S., Schmitt, J., Nehrbass-ahles, C., Stocker, T. F., Fischer, H., Kipfstuhl, S., & Chappellaz, J. (2015). Revision of the EPICA Dome C CO2 record from 800 to 600 kyr before present. *Geophysical Research Letters*, *47*, 542–549. https://doi.org/10.1002/2014GL061957

Bereiter, B., Shackleton, S., Baggenstos, D., Kawamura, K., & Severinghaus, J. (2018). Mean global ocean temperatures during the last glacial transition. *Nature*, *553*(7686), 39–44. https://doi.org/10.1038/nature25152

Bereiter, B., Kawamura, K., & Severinghaus, J. P. (2018). New methods for measuring atmospheric heavy noble gas isotope and elemental ratios in ice core samples. *Rapid Communications in Mass Spectrometry*, *32*(10), 801–814. https://doi.org/10.1002/rcm.8099

Broecker, W. S. (1982). Glacial to Interglacial Changes in Ocean Chemistry. *Progress in Oceanography*, *11*, 151–197. https://doi.org/https://doi.org/10.1016/0079-6611(82)90007-6

Buizert, C., & Schmittner, A. (2015). Southern Ocean control of glacial AMOC stability and Dansgaard-Oeschger interstadial duration. *Paleoceanography*, *30*, 1595–1612. https://doi.org/10.1002/2015PA002795

Buizert, C., Cuffey, K. M., Severinghaus, J. P., Baggenstos, D., Fudge, T. J., Steig, E. J., Markle, B. R., Winstrup, M., Rhodes, R. H., Brook, E. J., Sowers, T. A., Clow, G. D., Cheng, H., Edwards, R. L., Sigl, M., McConnell, J. R., & Taylor, K. C. (2015). The WAIS-Divide deep ice core WD2014 chronology – Part 1 : Methane synchronization (68 – 31 ka BP) and the gas age-ice age difference. *Climate of the Past*, *11*, 153. https://doi.org/10.5194/cp-11-153-2015

Cheng, H., Edwards, R. L., Sinha, A., Spötl, C., Yi, L., Chen, S., Kelly, M., Kathayat, G., Wang, X., Li, X., Kong, X., Wang, Y., Ning, Y., & Zhang, H. (2016). The Asian monsoon over the past 640,000 years and ice age terminations. *Nature*, *534*(7609), 640–646. https://doi.org/10.1038/nature18591

Craig, H., Horibe, Y., & T., S. (1988). Gravitational Seperation of Gases and Isotopes in Polar Ice Caps. *Science*, *242*(4886), 1675–1678. https://doi.org/10.1126/science.242.4886.1675

Curry, W. B., & Oppo, D. W. (2005). Glacial water mass geometry and the distribution of d13 C of CO2 in the western Atlantic Ocean. *Paleoceanography*, *20*, 1–13. https://doi.org/10.1029/2004PA001021

Cutler, K. B., Edwards, R. L., Taylor, F. W., Cheng, H., Adkins, J., Gallup, C. D., Cutler, P. M., Burr, G. S., & Bloom, A. L. (2003). Rapid sea-level fall and deep-ocean temperature change since the last interglacial period. *Earth and Planetary Science Letters*, *206*, 253–271. https://doi.org/10.1016/S0012-821X(02)01107-X

Emiliani, C. (1955). Pleistocene Temperatures. *The Journal of Geology*, *63*(6), 538–578. https://doi.org/https://doi.org/10.1086/626295

Grant, K. M., Rohling, E. J., Ramsey, C. B., Cheng, H., Edwards, R. L., Florindo, F., Heslop, D., Marra, F., Roberts, A. P., Tamisiea, M. E., & Williams, F. (2014). Sea-level variability

over five glacial cycles. *Nature Communications*, *5*(5076), 1–9. https://doi.org/10.1080/08989575.2017.1289316

Headly, M. A., & Severinghaus, J. P. (2007). A method to measure Kr/N2 ratios in air bubbles trapped in ice cores and its application in reconstructing past mean ocean temperature. *Journal of Geophysical Research*, *112*(19), 1–12. https://doi.org/10.1029/2006JD008317

Hemming, S. R. (2004). Heinrich Events: Massive Late Pleistocene Detritus Layers of the North Atlantic and their Global Climate Imprint. *Reviews of Geophysics*, *42*. https://doi.org/10.1029/2003RG000128

Imbrie, J., Berger, A., Boyle, E. A., Clemens, S. C., Duffy, A., Howard, W. R., Kukla, G., Kutzbach, J., Martinson, D. G., Mcintyre, A., Mix, A. C., Molfino, B., Morley, J. J., Peterson, L. C., Pisias, N. G., Prell, W. L., Raymo, M. E., Shackleton, N. J., & Toggweiler, J. R. (1992). On the structure and origin of major glaciation cycles 2: The 100,000-year cycle. *Paleoceanography*, *8*(6), 699–735. https://doi.org/https://doi.org/10.1029/92PA02253

Jouzel, J., Masson-Delmotte, V., Cattani, O., Dreyfus, G., Falourd, S., Hoffmann, G., Minster, B., Nouet, J., Barnola, J. M., Chappellaz, J., Fischer, H., Gallet, J. C., Johnsen, S., Leuenberger, M., Loulergue, L., Luethi, D., Oerter, H., Parrenin, F., Raisbeck, G., et al. (2007). Orbital and Millennial Antarctic Climate Variability over the Past 800,000 years. *Science*, *317*(5839), 793–796. https://doi.org/10.1126/science.1141038

Lisiecki, L. E., & Raymo, M. E. (2005). A Pliocene-Pleistocene stack of 57 globally distributed benthic d18O records. *Paleoceanography*, *20*. https://doi.org/10.1029/2004PA001071

Lynch-Stieglitz, J., Curry, W. B., & Slowey, N. (1999). Weaker Gulf Stream in the Florida Straits during the Last Glacial Maximum. *Nature*, *402*. https://doi.org/10.1038/45204

Mcmanus, J. F., Oppo, D. W., & Cullen, J. L. (1999). A 0.5-Million-Year Record of Millennial-Scale Climate Variability in the North Atlantic. *Science*, *283*(5404), 971–975. https://doi.org/10.1126/science.283.5404.971

Menking, J. A. (2019). *Stable Isotope Constraints on Carbon Dioxide and Nitrous Oxide Variations at the Onset of the Last Glacial Period: New Ice Core Records from Taylor Glacier, Antarctica*. Oregon State University.

Menking, J. A., Brook, E. J., Shackleton, S. A., Severinghaus, J. P., Dyonisius, M., Petrenko, V., McConnell, J. R., Rhodes, R. H., Bauska, T. K., Baggenstos, D., Marcott, S., & Barker, S. (2018). Spatial pattern of accumulation at Taylor Dome during the last glacial inception: stratigraphic constraints from Taylor Glacier. *Climate of the Past Discussions*, 1–25. https://doi.org/10.5194/cp-2018-53

Oliver, K. I. C., Hoogakker, B. A. A., Crowhurst, S., Henderson, G. M., Rickaby, R. E. M., Edwards, N. R., & Elderfield, H. (2010). A synthesis of marine sediment core δ13C data

over the last 150 000 years. *Climate of the Past*, *6*, 645–673. https://doi.org/10.5194/cp-6-645-2010

Pedro, J. B., Jochum, M., Buizert, C., He, F., Barker, S., & Rasmussen, S. O. (2018). Beyond the bipolar seesaw: Toward a process understanding of interhemispheric coupling. *Quaternary Science Reviews*, *192*, 27–46. https://doi.org/10.1016/j.quascirev.2018.05.005

Rhodes, R. H., Brook, E. J., Chiang, J. C. H., Blunier, T., Maselli, O. J., McConnell, J. R., Romanini, D., & Severinghaus, J. P. (2015). Enhanced tropical methane production in response to iceberg discharge in the North Atlantic. *Science*, *348*(6238), 1016–1019. https://doi.org/10.1126/science.1262005

Schaefer, J. M., Putnam, A. E., Denton, G. H., Kaplan, M. R., Birkel, S., Doughty, A. M., Kelley, S., Barrell, D. J. A., Finkel, R. C., Winckler, G., Anderson, R. F., Ninneman, U. S., Barker, S., Schwartz, R., Andersen, B. G., & Schluechter, C. (2015). The Southern Glacial Maximum 65,000 years ago and its Unfinished Termination. *Quaternary Science Reviews*, *114*, 52–60. https://doi.org/10.1016/j.quascirev.2015.02.009

Severinghaus, J. P., Sowers, T., Brook, E. J., Alley, R. B., & Bender, M. L. (1998). Timing of abrupt climate change at the end of the younger dryas interval from thermally fractionated gases in polar ice. *Nature*, *391*(6663), 141–146. https://doi.org/10.1038/34346

Severinghaus, J. P., Severinghaus, J. P., Beaudette, R., & Headly, M. A. (2009). Oxygen-18 of O2 Records the Impact of Abrupt Climate Change on the Terrestrial Biosphere. *Science*, 1431–1434. https://doi.org/10.1126/science.1169473

Shackleton, S., Bereiter, B., Baggenstos, D., Bauska, T. K., Brook, E. J., Marcott, S. A., & Severinghaus, J. P. (2019). Is the noble gas-based rate of ocean warming during the Younger Dryas overestimated? *Geophysical Research Letters*. https://doi.org/doi: 10.1029/2019GL082971

Shakun, J. D., Lea, D. W., Lisiecki, L. E., & Raymo, M. E. (2015). An 800-kyr record of global surface ocean δ 18 O and implications for ice volume-temperature coupling. *Earth and Planetary Science Letters*, *426*, 58–68. https://doi.org/10.1016/j.epsl.2015.05.042

Sigman, D. M., Hain, M. P., & Haug, G. H. (2010). The polar ocean and glacial cycles in atmospheric CO2 concentration. *Nature*, *466*, 47–55. https://doi.org/10.1038/nature09149

Thornalley, D. J. R., Barker, S., Becker, J., Hall, I. R., & Knorr, G. (2013). Abrupt changes in deep Atlantic circulation during the transition to full glacial conditions. *Paleoceanography*, *28*, 253–262. https://doi.org/10.1002/palo.20025

Veres, D., Bazin, L., Landais, A., Toye Mahamadou, K. H., Lemieux-Dudon, B., Parrenin, F., Martinerie, P., Blayo, E., Blunier, T., Capron, E., Chappellaz, J., Rasmussen, S. O., Severi, M., Svensson, A., Vinther, B. M., & Wolff, E. W. (2013). The Antarctic ice core chronology (AICC2012): an optimized for the last 120 thousand years. *Climate of the Past*,

9, 1733–1748. https://doi.org/10.5194/cp-9-1733-2013

Waelbroeck, C., Labeyrie, L., Michel, E., Duplessy, J. C., Mcmanus, J. F., Lambeck, K., Balbon, E., & Labracherie, M. (2002). Sea-level and deep water temperature changes derived from benthic foraminifera isotopic records. *Quaternary Science Reviews*, *21*, 295–305. https://doi.org/10.1016/S0277-3791(01)00101-9

Wang, Y., Cheng, H., Edwards, R. L., An, Z. S., Wu, J. Y., Shen, C. C., & Dorale, J. A. (2001). A high-resolution absolute-dated late pleistocene monsoon record from Hulu Cave, China. *Science*, *294*(5550), 2345–2348. https://doi.org/10.1126/science.1064618

Yu, J., Menviel, L., Jin, Z. D., Thornalley, D. J. R., Barker, S., Marino, G., Rohling, E. J., Cai, Y., Zhang, F., Wang, X., Dai, Y., Chen, P., & Broecker, W. S. (2016). Sequestration of carbon in the deep Atlantic Sequestration of carbon in the deep during the last glaciation Atlantic during the last glaciation. *Nature Geoscience*, *2657*. https://doi.org/10.1038/NGEO2657